

MOLECULAR SIMULATION OF NANOSCALE TRANSPORT PHENOMENA

Soumik Banerjee

Dissertation submitted to the Faculty of Virginia Polytechnic Institute and State
University in partial fulfillment of the requirements of the degree of

Doctor of Philosophy
in
Engineering Mechanics

Dr. Ishwar K. Puri, Chair

Dr. Romesh C. Batra

Dr. Muhammad Hajj

Dr. Michael W. Hyer

Dr. Kyungwha Park

June 16, 2008

Blacksburg, Virginia

Keywords: Nanotechnology, Molecular Dynamics, Carbon Nanotube

MOLECULAR SIMULATION OF NANOSCALE TRANSPORT PHENOMENA

Soumik Banerjee

ABSTRACT

Interest in nanoscale heat and mass transport has been augmented through current trends in nanotechnology research. The theme of this dissertation is to characterize electric charge, mass and thermal transport at the nanoscale using a fundamental molecular simulation method, namely molecular dynamics. This dissertation reports simulations of (1) ion intake by carbon nanotubes, (2) hydrogen storage in carbon nanotubes, (3) carbon nanotube growth and (4) nanoscale heat transfer. Ion transport is investigated in the context of desalination of a polar solution using charged carbon nanotubes. Simulations demonstrate that when either a spatially or temporally alternating charge distribution is applied, ion intake into the nanotubes is minimal. Thus, the charge distribution can either be maintained constant (for ion encapsulation) or varied (for water intake) in order to achieve different effects. Next, as an application of mass transport, the hydrogen storage characteristics of carbon nanotubes under modified conditions is reported. The findings presented in this dissertation suggest a significant increment in storage in the presence of alkali metals. The dependence of storage on the external thermodynamic conditions is analyzed and the optimal range of operating conditions is identified. Another application of mass transport is the growth mode of carbon nanostructures (viz. tip growth and base growth). A correct prediction of the dominant growth mode depends on the energy gain due to the addition of C-atoms from the carbon-metal catalyst solution to the graphene sheets forming the carbon nanostructures. This energy gain is evaluated through

molecular dynamics simulations. The results suggest tip growth for Ni and base growth for Fe catalysts. Finally, unsteady nanoscale thermal transport at solid-fluid interfaces is simulated using non-equilibrium molecular dynamics simulations. It is found that the simulated temperature evolution deviates from an analytical continuum solution due to the overall system heterogeneity. Temperature discontinuities are observed between the solid-like interfaces and their neighboring fluid molecules. With an increase in the temperature of the solid wall the interfacial thermal resistance decreases.

This thesis is dedicated to my fiancée Sudeshna without whose continuous support, encouragement and inspiration it would never have been accomplished.

ACKNOWLEDGEMENTS

I extend my gratitude and sincere thanks to my advisor Prof. Ishwar K. Puri for his constant help and guidance that contributed to the completion of this dissertation. Professor Puri not only inspired me through myriad interesting discussions and brainstorming sessions, but also made sure that I worked on a research topic that was both intellectually stimulating and useful to the scientific community. I would also like to thank my co-advisor Prof. Sohail Murad for his continuous guidance. Without his invaluable input this dissertation would not be completed. Gratitude is expressed to my dissertation committee – Professors Romesh C. Batra, Muhammad Hajj, Michael W. Hyer, and Kyungwha Park – for their unwavering support and encouragement.

I express my sincere thanks to my colleagues Sayangdev Naha and Ganesh Balasubramanian with whom I collaborated on various research projects. I would specially like to thank my colleagues Anindya De, Sayangdev Naha, and Ashok Sinha for their continuous support and for the numerous debates and discussions that I have had with them, both academic and non-academic. Without their presence the whole experience of working in the lab over the past four years would not be as much enjoyable and intellectually stimulating as it has been. I express sincere gratitude to Prof. Ranjan Ganguly for all the motivating discussions that I have had with him. Gratitude is expressed to Prof. Swarnendu Sen for his help and guidance in numerous aspects.

Finally, I thank my parents Mrs. Jolly Banerjee and Mr. Swapan Banerjee for their unwavering support. The confidence in my abilities and encouragement that they have continuously provided me with has led to the culmination of my PhD.

CONTENTS

Abstract.....	ii
Acknowledgements	v
Contents	vi
List of Figures.....	viii
List of Tables	xii
Chapter 1: Introduction.....	1
1.1. Motivation	1
1.2. Objective	4
1.3. Contributions.....	5
1.4. Outline of the dissertation	6
Chapter 2: Background.....	7
2.1. Carbon Nanostructures.....	7
2.2. Molecular Simulation Methods.....	9
2.2.1. Molecular Dynamics.....	11
2.3. Ion Adsorption in Carbon Nanotubes.....	13
2.4. Hydrogen Storage in Carbon Nanotubes.....	14
2.4.1. Storage Mechanism.....	14
2.4.2. Review of Previous Hydrogen Storage Investigations	16
2.4.3. Means of Enhanced Storage.....	22
2.5. Carbon Nanotube Growth Mode	27
2.6. Nanoscale Heat Transfer at Solid-Fluid Interfaces	28
Chapter 3: Ion Adsorption in Carbon Nanotubes	30

3.1. Introduction	30
3.2. Methodology	31
3.3. Results and Discussion.....	35
Chapter 4: Hydrogen Storage in Carbon Nanotubes.....	44
4.1. Introduction	44
4.2. Methodology	45
4.3. Results and Discussion.....	49
Chapter 5: Carbon Nanotube Growth Mode.....	60
5.1. Introduction	60
5.2. Methodology	62
5.3. Results and Discussion.....	65
Chapter 6: Nanoscale Heat Transfer at Solid-Fluid Interfaces	69
6.1. Introduction	69
6.2. Methodology	70
6.3. Results and Discussion.....	73
Chapter 7: Conclusions	81
7.1. Ion Adsorption in Carbon Nanotubes.....	81
7.2. Hydrogen Storage in Carbon Nanotubes.....	81
7.3. Carbon Nanotube Growth Mode	82
7.4. Nanoscale Heat Transfer at Solid-Fluid Interfaces	82
Bibliography	84
Appendix A.....	110

LIST OF FIGURES

<u>FIGURE</u>	<u>PAGE</u>
Figure 2.1: Various types of carbon nanotubes are characterized by their respective chiral angles.	8
Figure 3.1: Schematic diagrams of the simulated charge distributions. (The deeper shade corresponds to a negative charge on a carbon atom while the lighter shade is for a positive charge.).....	31
Figure 3.2: Schematic diagram of the simulated system.	33
Figure 3.3: Water molecule intake by the nanotubes for different charge distributions. Initially, a 13.96% sodium chloride solution surrounds the carbon nanotube and the system is at ambient temperature and pressure. The surface charge density in each case (except for the uncharged nanotube) is 0.825 C/m^2	36
Figure 3.4: Water molecule intake by carbon nanotubes used as conventional electrodes for different charge densities, also for a 13.96% initial sodium chloride solution. The surface charge densities on the electrodes are zero (uncharged nanotube), 0.825 C/m^2 , 1.65 C/m^2 and 3.3 C/m^2	38
Figure 3.5: (a) Sodium and (b) chloride ion intake by the nanotubes for different charge distributions and for conditions that are used to obtain the results in Fig. 3.3.	41
Figure 4.1: Comparison of result from Prof. Murad's Code with that of LAMMPS.....	45
Figure 4.2: Schematic diagram of the simulated system. Interconnects made of Li-, Pd- and Ti-ions, and C atoms (purple) are used to join adjacent carbon nanotubes (green), surrounded by hydrogen molecules (blue).....	48

Figure 4.3: Variation of hydrogen storage with pressure at 273 K for various interconnect materials joining the carbon nanotubes..... 50

Figure 4.4: (a) Variation of hydrogen storage with pressure at 273 K in the presence of Li ion interconnects for various charge patterns on the carbon nanotubes. The plot in the inset presents similar results at 100 K. **(b):** Schematic of the circumferential ring type charge distribution (Banerjee et al, 2007). The dark lines represent sites with negative charges, while lighter ones represent positive charges. 51

Figure 4.5: Hydrogen storage isobars for uncharged nanotubes in the presence of Li ion interconnects. The inset presents the slope of these isobars at various temperatures.

$$\text{Here, } f(T_r) = \left. \frac{\partial \rho_r}{\partial T_r} \right|_{p_r} / 1.2kp_r^{0.8} \dots\dots\dots 54$$

Figure 4.6: Hydrogen storage isotherms for uncharged nanotubes in presence of Li ion interconnects. The inset presents the slope of these isotherms at various pressures. Here,

$$g(p_r) = \left. \frac{\partial \rho_r}{\partial p_r} \right|_{T_r} / 0.8kT_r^{-1.2} \dots\dots\dots 55$$

Figure 4.7: Hydrogen storage isobars for uncharged nanotubes in the presence of C interconnects. The inset presents the slope of these isobars at various temperatures. Here,

$$h(T_r) = \left. \frac{\partial \rho_r}{\partial T_r} \right|_{p_r} / 1.1kp_r^{0.35} \dots\dots\dots 56$$

Figure 4.8: Hydrogen storage isotherms for uncharged nanotubes in presence of C interconnects. The inset presents the slope of these isotherms at various pressures. Here,

$$q(p_r) = \left. \frac{\partial \rho_r}{\partial p_r} \right|_{T_r} / 0.35kT_r^{-1.1} \dots\dots\dots 57$$

Figure 4.9: Variation of hydrogen storage with pressure in open and closed-ended carbon nanotube electrodes in the presence of Li ion interconnects.	59
Figure 5.1: Schematic illustrating the growth modes of carbon nanotubes.	61
Figure 5.2: A two-dimensional orthographic view of the molecular dynamics simulation domain with the carbon nanotube (green), which is surrounded by ambient Ar (gray), growing on top of the metal catalyst particle (blue) that has dissolved carbon (red).	64
Figure 5.3: Variation of the total system energy with time.	66
Figure 5.4: Variation of the energy change with respect to temperature for Ni and Fe. .	67
Figure 6.1: A 3-dimensional view of the molecular dynamics simulation domain in which Ar (cyan) fills a space of 28 nm between two 1 nm thick blocks of solid Fe. Fluid atoms on both sides of the walls indicate periodicity. A close-up orthographic view shows the observed Ar–atom layering at the solid-fluid interface.	72
Figure 6.2: The temperature (dotted line) and density (solid line) distributions across the x-wise direction after the system nears its steady state. The solid Fe walls are located between 14-15 nm and 43-44 nm. The fluid domain is divided into several 4 Å thick slabs along the x-direction for the purpose of spatial characterization, and the density and temperature distributions within them are sampled at uniform time intervals.	74
Figure 6.3: Temporal evolution of the fluid temperature obtained explicitly from the simulations and empirically from an analytical solution to Fourier’s law of heat conduction (assuming homogenous and constant properties).	76
Figure 6.4: Schematic of the system solved using Fourier’s Equation.	77
Figure 6.5: Temporal evolution of the interfacial thermal resistances for wall temperature of 125 K (based on heat fluxes calculated using a first principles and a quasi-continuum	

approach). The interfacial temperature drop is calculated as a time average over 100 ps.

..... 79

Figure 6.6: Change in the Kapitza resistance (based on heat fluxes calculated using a first principles approach) with respect to varying wall temperature. The fluxes and temperature drops are averaged over 2000-4000 ps. 80

LIST OF TABLES

<u>TABLE</u>	<u>PAGE</u>
Table 2.1: Comparative table of the hydrogen storage capacities of various carbon nanostructures.	20
Table 3.1: Values of parameters used in the simulations for preferential ion intake.....	35
Table 3.2: Number of ions, water molecules, and encapsulated solution strength for various surface charge patterns. The surface charge density is 0.825 C/m^2	43
Table 4.1: Values of parameters used in the simulations for hydrogen storage.	47
Table 5.1: Lennard Jones interaction parameters for Fe, Ni, C and Ar.	63
Table 5.2: A chart showing representative energy values for a temperature of 700 K....	68
Table 6.1: Lennard Jones interaction parameters for Fe and Ar.....	71

Chapter 1: Introduction

Recent developments in nanotechnology pay an increasing importance on transport phenomena at the nanoscale. The bulk of the work so far has been either experimental or a theoretical approach modeled after continuum scale phenomena. There is a lack of agreement between the results of various groups. It is therefore important to understand these phenomena from a fundamental perspective. Molecular modeling can provide a basis for understanding nanoscale transport phenomena. Nanoscale transport can be of several kinds, such as charge, mass and thermal transport. The aim of this dissertation is to characterize these three forms of nanoscale transport using molecular dynamics (MD).

1.1. Motivation

Charge transport at the nanoscale is an area of immense interest to the scientific community. Charge separation is of interest to the field of bioanalysis, where desalination is of great importance. A fundamental understanding of ion separation processes is also pertinent to environmental science because they present a means for water purification based on nanofluidics. Electrostatic phenomena can be implemented at the nanoscale with a smaller absolute charge than at larger scales. For instance, due to a large surface area to volume ratio, nanotubes have a larger surface charge density than their mesoscale counterparts for similar local charge values. Thus, electrostatically charged carbon nanotubes (CNTs) can be used effectively as nanopumps for ion separation from a solution, as demonstrated later in the dissertation. Ion encapsulated nanotubes can also be used as nanoreactors for possible chemical reactions.

Mass transport at the nanoscale is pertinent to adsorption by nanomaterials as well as flow through and across nanostructures. It has important applications in hydrogen storage at the nanoscale. The US Department of Energy (DOE) benchmark for hydrogen storage is 6.5 weight percent and a volumetric density of 62 kg H₂/m³ (Wang and Johnson, 1999b) in a storing material. The use of hydrogen as a fuel is limited in large part because of lack of progress in developing suitable storage and delivery systems. Materials that adsorb significant quantities of hydrogen are therefore urgently needed. The special hydrogen adsorbing characteristics of carbon nanomaterials make them rather suited as hydrogen storage devices. Due to their high surface area and capillarity, CNTs have high hydrogen storage capacity. In this dissertation, the feasibility of CNT as a hydrogen storage device is investigated.

Mass transport at the nanoscale is also pertinent to species diffusion and growth due to bond formation. Catalyzed growth of carbon nanostructures occurs mainly through two modes, i.e., base growth when the metal nanoparticle remains at the bottom of the nanotube, or when it is lifted by the growing carbon nanostructure due to tip growth. A correct prediction of the dominant growth mode can be very useful for applications that involve metal-encapsulated CNTs. For instance, ferromagnetic metal particles at the end of CNTs can be used to align them. The dominant growth mode depends on the energy gain due to the addition of C-atoms from the carbon-metal catalyst solution to the graphene sheets forming the carbon nanostructures. Such growth modes are characterized in the dissertation through molecular simulations.

Thermal transport at the nanoscale is a topic of growing interest for researchers. The most significant question surrounding nanoscale thermal transport is the evaluation

of boundary resistances between nanoscale interfaces (Swartz and Pohl, 1989). Quantification of the interfacial thermal resistance (also known as Kapitza resistance (Kapitza, 1941)) has several applications. Thermal management of electronic packaging (thermo-electrics) (Darabi, 2002), nanofabrication techniques (Chen, 2000) as well as efficient nanoscale energy transfer are some of the pertinent applications of nanoscale thermal transport. Molecular dynamics has been one of the tools used to comprehend the physics of thermal conductivity in liquids (Heyes and March, 1996) and to study different modes of thermal transport in nanofluids (Eastman et al., 2004). This dissertation presents results that related to characterization of interfacial thermal transport.

Molecular dynamics simulations have contributed significantly to enhance the fundamental understanding of physical mechanisms at the nanoscale. Molecular simulations can be used to study many important unanswered questions relating to the permeation, adsorption, and selectivity of gases in nanoporous materials (Sourirajan and Matsuura, 1985) that primarily involve molecular forces and, thus, cannot be directly addressed by continuum approaches. A fundamental molecular level approach (such as MD) can address these issues directly and unambiguously. The MD method (Allen, 1987, Haile, 1992, Evans and Morris, 1990, Murad et al., 1993) has been used to investigate a variety of static and dynamic properties of fluids in nanopores (Murad et al., 1993, Lin and Murad, 2001, Murad et al., 1998, Murad et al., 2003) and shown that osmosis, reverse osmosis, ion-exchange and gas separations can be observed for nonpolar, polar and electrolyte solutions. The bulk of the concluded work presented here is related to nanoscale transport. Hence, MD has been chosen as the preferred method.

1.2. Objective

The aim of the research presented is to characterize the transport of mass, charge and heat at the nanoscale through molecular simulations. With regards to charge transport, preferential ion adsorption in CNTs is characterized. The effect of charge pattern on CNT surfaces on the intake of either water or ions is determined. The aim of this project is to come up with an effective strategy by which the intake of either ion or water inside CNT can be controlled. Molecular dynamics is used to investigate the charge transport phenomenon.

Next, mass transport at the nanoscale is characterized. Two relevant problems are presented. The first research project involves hydrogen storage in CNTs. Molecular simulation is used to study the effect of temperature, pressure, configuration, presence of metal interconnects, surface charge on the enhancement of hydrogen storage in CNTs. The objective is to come up with optimal conditions for storage. The second project aims at prediction of the growth mode during catalytic synthesis of CNTs. A variety growth conditions relevant to the CVD synthesis of CNTs, including a range of temperature (700 – 1100 K) and two different catalysts (iron and nickel) are simulated.

Finally, nanoscale thermal transport at solid-fluid interfaces is characterized using non-equilibrium molecular dynamics (NEMD) simulations. The results thus obtained are compared with those obtained using continuum scale approximations. The thermal resistance at the interface is evaluated for various solid temperatures and its time evolution is quantified.

1.3. Contributions

The key contributions highlighted in the dissertation are listed below:

1. The dissertation demonstrates that CNTs with varied charge distributions can be used as devices for the controlled intake of either ions or polar solvents. For a spatially or temporally alternating charge distribution, a nanotube preferentially encapsulates polar solvents (such as water) from a solution, while a uniform charge distribution promotes the intake and encapsulation of ions.
2. The optimal conditions for hydrogen storage in CNTs are identified. While the literature suggests that metallic contaminants enhance storage, the findings presented in this dissertation suggest that this is significant for alkali and not transition metals. Charging the CNT surfaces does not significantly enhance hydrogen storage. It is found that the bulk of the hydrogen storage occurs inside CNTs due to their nanocapillarity effect. However, hydrogen storage is much more dependent on external thermodynamic conditions such as the temperature and the pressure than on these facets of the CNT structure. The dependence of storage on the external thermodynamic conditions is analyzed and the optimal range of operating conditions is identified.
3. The energy gain due to the addition of carbon atoms from the nanoparticle to the CNT is evaluated through atomistic scale MD simulations. The results suggest that while in case of Fe nanoparticle, the surface interaction energy is greater than the energy gain; the converse is true for Ni. Hence, the presence of Ni catalyst promotes tip growth while Fe catalyst promotes base growth.

4. The MD simulation results suggest that thermal transport at the nanoscale is remarkably different from that at the continuum scale. It is observed from the results that the nanoscale system has a discrete temperature drop at the solid-fluid interface due to phase segregation of the fluid. The thermal resistance at the interface is a function of the solid temperature and decreases as the temperature of the solid increases.

1.4. Outline of the dissertation

An introduction to the research presented in the dissertation is provided in Chapter 1. Chapter 2 provides a background to the research and the terminology discussed in the dissertation. It also cites the literature pertinent to the results presented in the chapters that follow. The results and discussion in the dissertation can be essentially divided into four parts, as discussed in Chapters 3 through 6. Chapter 3 presents results related to nanoscale charge transport. It typically deals with the application of nanoscale charge transport to preferential ion intake in CNTs. Chapters 4 and 5 are related to mass transport and talk about two different applications. While Chapter 4 discusses hydrogen storage in CNTs and scopes of enhancement, Chapter 5 presents a molecular model that predicts the growth mode of CNTs. The results presented in the former chapter suggest means to improve hydrogen storage in carbon nanostructures while those presented in the latter chapter are pertinent to several methods used in CNT synthesis such as the Chemical Vapor Deposition (CVD). Simulation results for unsteady nanoscale thermal transport is provided in Chapter 6. Finally, Chapter 7 presents the salient conclusions related to the results discussed in Chapters 3 through 6.

Chapter 2: Background

2.1. Carbon Nanostructures

Carbon nanostructures, such as CNTs and carbon nanofibers (CNFs), are graphitic (sp^2 -hybridized) structures made of carbon that have characteristic dimensions of the order of nanometers. In recent times, carbon nanostructures have attracted wide attention due to their wide range of applications. Carbon nanotubes are graphene sheets rolled into seamless tubes with diameters that are of the order of nanometers. In addition to the ability to store hydrogen, they also possess other outstanding properties such as mechanical strength, metallic or semiconducting behavior and metal particle encapsulation (Yu et al., 1999, Kong et al., 2000, Yu et al., 2000, Collins et al., 2000, Rueckes et al., 2000, Ren and Price, 2001, Akita et al., 2001). Carbon nanofibers basically consist of an intercalation of these graphitic planes at a fixed distance (0.355 nm) from each other to form a variety of structures. Carbon nanotubes and nanofibers are usually grown on metallic surfaces by the catalytic action of one or more transition metals. The nanofibers have enhanced strength, and thermal and electrical properties as compared to nanotubes (Louchev et al., 2003, Heremans and Beetz, 1985, Heremans, 1985, Endo et al., 2001). Activated carbon is an amorphous variety of carbon with high surface area due to the presence of carbon nanoparticles. All these allotropes of carbon exhibit hydrogen adsorption capabilities.

A CNT can be one of three types; (1) armchair, (2) zigzag and (3) chiral depending on the orientation along which the graphitic planes are folded. Figure 2.1 describes the chiral vector $\vec{c} = m\vec{a}_1 + n\vec{a}_2$ and the chiral angle θ . When the value of θ is,

respectively, 30° , 0° or anywhere in between, a nanotube is respectively called zigzag, armchair or chiral. The chiral vector \vec{c} is expressed in terms of the unit vectors \vec{a}_1 and \vec{a}_2

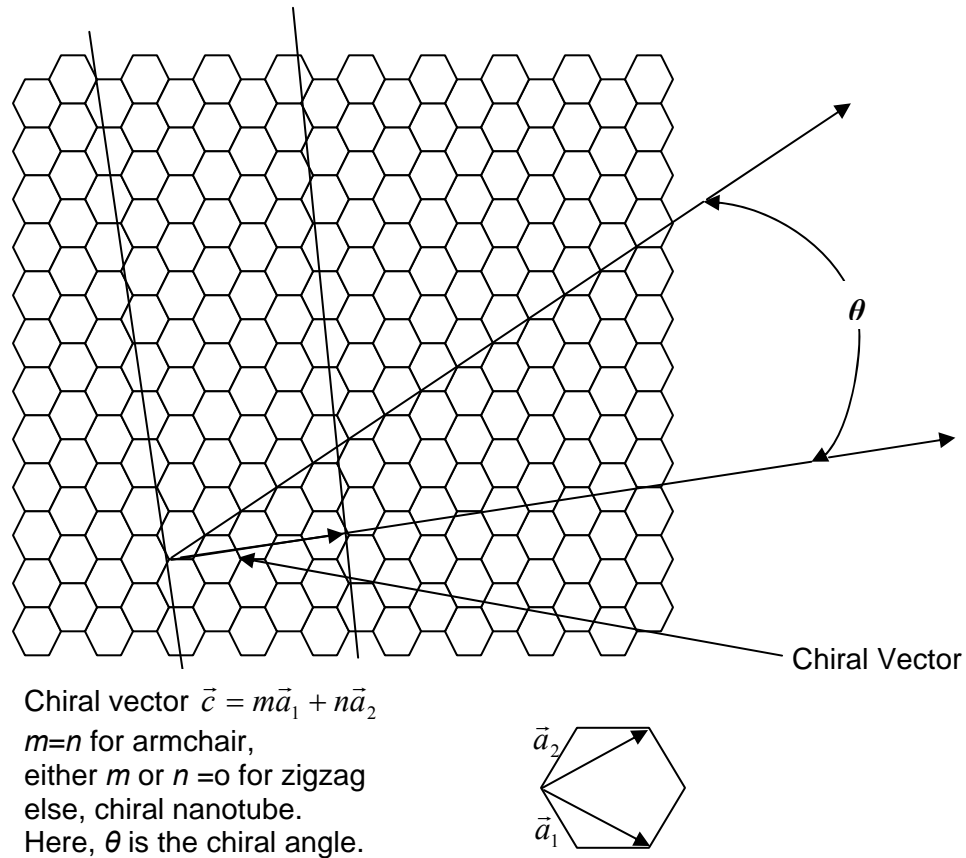


Figure 2.1: Various types of carbon nanotubes are characterized by their respective chiral angles.

that are oriented along two particular directions along the unit hexagonal cell. The constants m and n determine whether the nanotube is of the armchair, zigzag, or chiral type. The nanotube is of the armchair type if $m = n$, zigzag if either m or n are zero, and chiral for all other cases. Similarly, a nanofiber can also be of three types, namely, platelet, tubular or herringbone, based on the orientation of its graphitic planes. If the

planes are perpendicular or parallel to the axis of the fiber, the nanofiber is of a platelet or tubular type, respectively. If the graphitic planes are inclined with respect to the axis, it is referred to as a herringbone nanofiber. The various adsorption, storage and conducting properties of CNTs depend on its chirality.

2.2. Molecular Simulation Methods

Molecular simulation refers to theoretical methods and computational techniques to model or mimic the behavior of molecules. These techniques are frequently used in the fields of computational chemistry, computational biology and materials science for studying molecular systems ranging from a few atoms to a system of millions of molecules. By definition, molecular simulation methods have a lowest level resolution of individual atoms.

Molecular simulations can be used to study many important unanswered questions relating to the permeation, adsorption, and selectivity of gases in nanoporous materials (Sourirajan and Matsuura, 1985) that primarily involve molecular forces and, thus, cannot be directly addressed by continuum approaches. A fundamental molecular level approach (such as MD) can address these issues directly and unambiguously. The MD method (Allen, 1987, Haile, 1992, Evans and Morris, 1990) has been used to investigate a variety of static and dynamic properties of fluids in nanopores (Murad et al., 1993, Lin and Murad, 2001, Murad et al., 1998, Murad et al., 2003) and shown that osmosis, reverse osmosis, ion-exchange and gas separations can be observed for nonpolar, polar and electrolyte solutions.

Molecular dynamics and Monte Carlo methods have relative advantages and disadvantages depending on the system and properties being simulated. While MD is a

deterministic method that solves for the equation of motion of individual molecules and looks at the time evolution of the system, conventional Monte Carlo is stochastic and samples a given set of random movements of atoms/molecules, selecting or rejecting it on the basis of the configurational energy. Monte Carlo is usually time-independent. Computationally too these methods have relative merits and demerits based on the system at hand. In MD the position of each atom/molecule is determined by solving the equation of motion, while in case of Monte Carlo the motion is stochastically sampled and hence generally involves less computational time. However, if there are a large number of rejections in stochastic motions (e.g. dense fluids), the computational time increases. Monte Carlo is better suited to simulation of moderate-density fluids while MD is advantageous in case of higher density fluids such as gases under high pressure or liquids. Further, MD can be used to calculate dynamic properties while conventional Monte Carlo cannot determine these properties. Grand Canonical Monte Carlo can handle a variable number of particles while MD is usually implemented with a constant number of particles. One central similarity in both these methods is the use of a potential function. The accuracy of the results predicted by Monte Carlo or MD depends on the accuracy of the potential function. One therefore needs to be careful in selecting the potential function.

The density functional theory is a quantum mechanistic approach for solving atomic scale systems and is hence more fundamental than MD or Monte Carlo. One of the drawbacks of this method is that the exact form of the universal energy density functional is unknown and approximation is involved. Also, since quantum mechanistic calculations typically involve length scales of the order of Angstroms, it is

computationally expensive to characterize systems with dimensions of several nanometers. Hence, molecular simulations provide an optimal approach to model nanoscale systems.

2.2.1. Molecular Dynamics

Molecular dynamics simulations compute the motions of individual molecules in models of solids, liquids and gases. It provides a technique to compute trajectories and velocities of atoms and molecules in a nanoscale system. Molecular dynamics method can be used effectively to investigate a variety of nanoscale transport processes. For instance, various physical properties of carbon nanostructures depend primarily on the intermolecular forces between the atoms constituting the membrane pores (or surface) and the atoms (or molecules) that surround them. Similarly, the adsorption/absorption of gases on the surface and in the pores of a nanostructure also depend on these forces, as does the ability of certain molecules to diffuse faster in nanopores as compared to other molecules. Only a fundamental molecular level approach (such as MD) can address these issues directly and unambiguously. A typical MD simulation methodology can be implemented using the following steps:

1. Establishing the initial configuration (geometry) of a suitable nanostructure to be used during the molecular simulation:

The initial configuration depends on the system that is characterized. For all the simulations presented in this dissertation, the initial configuration comprises of essentially two different kinds of structures, (1) a complex molecule/membrane, the structure of which is obtained experimentally and is available from the literature (e.g. (Li et al., 2003b)), (2) metal or gaseous atoms. The initially assigned structure for the metal

or gaseous atoms usually comprises of a face centered cubic (fcc) or a body centered cubic lattice. This initial configuration can be far removed from the realistic minimum-energy equilibrium structure. The simulated system is given a random initial velocity distribution that scales with the required temperature and allowed to evolve temporally and the total energy is monitored. The system is said to relax as it evolves from its initial configuration and velocity distribution (that may be arbitrary) towards equilibrium. When the total energy reaches a minimal value, the system is said to have equilibrated. This signifies that the system is independent of its initial state (since it has reached thermodynamic equilibrium) and can be characterized. The active sites or surfaces correspond to simple atoms (such as monatomic gases like Ar) or complicated molecular structures (such as CNTs).

2. Prescribing the intermolecular interactions:

The interactions between the various molecules in the simulated system can be modeled using a suitable empirical potential which is typically a function of the distance between the atoms. A common example of a potential function is the LJ potential with the Coulombic interaction term, represented by the following functional form

$$u_{ij} = 4\varepsilon_{ij} \left[\left(\frac{\sigma_{ij}}{r_{ij}} \right)^{12} - \left(\frac{\sigma_{ij}}{r_{ij}} \right)^6 \right] + \frac{q_i q_j}{r_{ij}}. \quad (2.1)$$

In Eq. (2.1), u_{ij} denotes the interaction potential between sites i and j , r_{ij} the scalar distance between sites i and j , σ_{ij} and ε_{ij} are the LJ interaction parameters, and q_i and q_j represent the charges on sites i and j (although not all sites have charges). The potential parameters σ and ε , and charges q are usually obtained from the literature.

The gradient of the potential function provides the force. At any instant, the total force on an atom due to all other atoms in the system can be evaluated. The acceleration of each atom at each time step can be thus obtained. A suitable numerical integration scheme can then evaluate the velocities and positions of each atom at any instant. This temporal evolution of the system can be then used to evaluate useful properties of the nanoscale system.

An MD simulation can either be based on a system at thermal equilibrium or non-equilibrium. For example, if a nanoscale system has an imposed temperature gradient the system is not at thermal equilibrium. In such situation the dynamics of the molecules can be computed using NEMD.

2.3. Ion Adsorption in Carbon Nanotubes

Interest in nanofluidic fundamentals stems from possible applications of nanoreactors (Tessonier et al., 2005) and nanodevices for fluid transport, bioanalysis (Fan et al., 2005, He et al., 2006, Khandurina and Guttman, 2002) and drug delivery (Martin et al., 2005). For instance, the selectivity in biological ion transport (Bell, 1998) through nanochannels (Duax et al., 2003) is of great importance in bioanalysis. The controlled encapsulation of specific ions within CNTs or their ability to selectively transport various substances is of significance in this regard (Hoos et al., 2006). With the development of fabrication methods for nanochannels (Datta et al., 2006), electro-osmotic flow (Qiao and Aluru, 2005), (Petsev and Lopez, 2006) through them has become a recent focus of research, and novel devices such as nanofluidic transistors (Karnik et al., 2005) and nanofluidic pumps (Chen et al., 2005) have been developed.

Due to their desirable chemical stability and electrical conductivity, the nanoscale dimensions of CNTs produce a relatively large surface area-to-volume ratio, making their use attractive in charge separation devices and as electrodes (Chen et al., 2004a, Dai et al., 2005). The mass transport (Duren et al., 2002), ion concentration (Duax et al., 2003), velocity distribution (Nagayama and Cheng, 2004, Kang et al., 2004, Hanasaki et al., 2004) and slip length (Kotsalis et al., 2004) have been investigated for flow inside CNTs. It is also important to characterize the ion-channel interaction (Duax et al., 2003, Arista, 2001) to properly understand electro-osmotic flows in electrically charged nanochannels. While techniques for the encapsulation of particular species have been proposed (Jeong et al., 2003, Jeong et al., 2002) none seem to be based on a generic controlled intake method. In this dissertation MD simulations have been used to demonstrate the utility of CNTs for water and ion separation (and subsequent encapsulation) from a salt solution.

2.4. Hydrogen Storage in Carbon Nanotubes

2.4.1. Storage Mechanism

The hydrogen adsorbing characteristics of carbon nanomaterials make them attractive candidates for storage devices. The nanosize adds another degree of freedom for fine-tuning the material properties, since the CNT length and its curvature also influence the thermodynamics of storage. In this dissertation methods to systematically evaluate the hydrogen adsorption limitations of various carbon nanostructures using MD simulations have been described. Strategies to overcome these limitations with structural modifications, such as metal encapsulation (Sen and Puri, 2004) have also been suggested. For instance, alkali metal-doped carbon nanostructures have been found to be even better adsorbents than carbon nanostructures (Chen et al., 1999).

Elemental carbon is known to adsorb significant quantities of hydrogen (Wang and Johnson, 1999c, Dillon et al., 1997) due to the strong intermolecular attractive forces between the molecules of the two species. This, in conjunction with exceptional capillarity and high surface area, leads to hydrogen adsorption in CNTs (Pederson and Broughton, 1992, Schmidt, 1993). Hydrogen is adsorbed both on the surface of the nanotubes as well as in the interstitial sites in triangular arrays of nanotubes called nanoropes. In addition, hydrogen is absorbed within the volume described by the nanotubes. The curvature inside the nanotubes subjects hydrogen atoms to stronger attraction than offered by a graphitic plane. This causes the nanotubes to be more efficient in hydrogen adsorption than planar structures. The hydrogen adsorption in a nanotube essentially occurs through two mechanisms (Li et al., 2003a):

1. Physisorption:

Through this process hydrogen molecules are adsorbed inside of a nanotube or in the interstice of a nanotube mesh due to a van der Waals attractive force between the carbon and hydrogen. There is no theoretical limit to the percentage of hydrogen that can be stored by this means because hydrogen is adsorbed in multiple layers. However, at room temperature and atmospheric pressure, only a monolayer of hydrogen is formed on the surface of the tube (Cabria et al., 2006), which limits the adsorption to 3.3% by weight (Zuttel et al., 2002). The effective surface area available for adsorption is an important parameter (Zhou et al., 2004b). The Brunauer-Emmet-Teller (BET) surface area characterization is widely used to estimate the physisorption capacity of CNTs (Ye et al., 1999).

2. Chemisorption:

Here, the hydrogen molecules are covalently bonded to the carbon atoms of the nanotube. Each carbon atom in the nanotube is sp^2 hybridized, bonded with three other carbon atoms and has a dangling π -bond. Therefore, there can be at most one hydrogen atom stored (chemisorbed) per carbon atom. Theoretical calculations based on density functional theory show that this limits the maximum storage limit to 7.7% (Li et al., 2003a) by weight. Desorption of the hydrogen atoms thus adsorbed is more difficult than in the case of physisorption and requires a higher temperature for hydrogen release.

2.4.2. Review of Previous Hydrogen Storage Investigations

1. Carbon Nanotubes:

There is wide disparity in the experimental results reported by researchers for the maximum hydrogen storage in single-walled nanotubes (SWNTs) (Zhou et al., 2004b, Hirscher et al., 2003, Dillon et al., 2000, Liu et al., 1999, Yang, 2000). In addition, as mentioned above, various experimentally obtained high storage capacity results (Dillon et al., 1997, Chambers et al., 1998) have not yet been corroborated (Hirscher et al., 2003, Pinkerton et al., 2000), even theoretically by using MD simulations, Monte Carlo methods or the density functional approach. The hydrogen weight percentage is generally measured by volumetric or gravimetric methods, both of which are prone to errors, causing discrepancies in the results. The impurity and limited quantity of the various nanotube samples might also account for a relatively large scatter in the experimental data (Hirscher et al., 2003). Thermal desorption spectrometry (TDS) is an effective method for the measurement of hydrogen adsorption but calibration using unstable hygroscopic materials like calcium hydride can produce erroneous results. Some of the

more efficient methods to measure the hydrogen adsorption are by the use of sensitive high-pressure microbalances (Pan et al., 2005), the tangent-mass method (Li et al., 2003c), and the elastic recoil detection method (Naab et al., 2006). Hirscher et al. (2003) claim that some of the experiments reported a higher adsorption rate than realistically possible.

Some experiments have implied that in SWNTs hydrogen storage is possible at moderate temperatures and ambient pressures at levels above the minimum volumetric storage prescribed by DOE (Wang and Johnson, 1999b, Dillon et al., 2000). However, other investigators have reported that a useful amount of hydrogen can only be stored at cryogenic temperatures and/or very high pressures (Ye et al., 1999, Liu et al., 1999). In addition, the experimentally obtained high storage capacity results of Chambers et al. (1998) and Dillon et al. (1997) have not yet been corroborated by theoretical or numerical simulations. Table 2.1 compares the various experimental results for hydrogen storage in nanotubes (Hirscher et al., 2003). It is clear from the data that it is important to more fully understand the hydrogen storage mechanism in carbon nanostructures to resolve the discrepancies.

Reference	Material	Temperature (K)	Pressure (Mpa)	Maximum Storage (weight %)
Callejas et al., 2004	Reduced CNT	77	0.04	3
Chambers et al., 1998	GNF	300	12	65
Chambers et al., 1998	GNF (tubular)	298	11.35	11.26

Chambers et al., 1998	GNF (herringbone)	298	11.35	67.55
Chambers et al., 1998	GNF (platelet)	298	11.35	53.68
Chen et al., 1999	Li-CNT	473-673	0.1	20
Chen et al., 1999	Li-CNT	<313	0.1	14
Chen et al., 2004	CNT	298	0.1	1
Darkrim et al., 2000	SWNT	80	10	11
Dillon et al., 1997	SWNT (low purity)	273	0.04	5-10
Dillon et al., 2000	SWNT (high purity)	298	0.04	3.5~4.5
Fan et al., 1999	CNF	300	10.1	~10
Guay et al., 2004	CNT	293	10	<1
Gupta et al., 2000	GNF	300	12	10
Haluska et al., 2004	SWNT	77	0.1	<0.46
Hirscher et al., 2001	SWNT-Fe	Ambient	0.08	<0.005
Hirscher et al., 2002	SWNT (ball-milled in Ar)	Ambient	0.08	<0.1
Hirscher et al., 2002	SWNT (ball-milled in D ₂)	Ambient	0.9	1.0

Liu et al., 1999	SWNT (50% purity)	300	10.1	4.2
Lueking, 2004	CNT	300	0.1	~0.1
Nishimiya et al., 2002	SWNT	295 77	0.1 0.1	0.86 2.12
Nützenadel et al., 1999	SWNT (50-70% pure, electrochemical)	-	-	~2
Orimo et al., 1999	Nanostructured graphite	300	1	7.4
Panella et al., 2005	CNT	300 77	~6 ~6	~0.5 ~2.5
Pinkerton et al., 2000	Li-CNT	473-663	0.1	0.72-4.2
Rajalakshmi et al., 2000	SWNT (80% pure, electrochemical)	-	-	2.9
Shen et al., 2004	CNT	300	<1.5	1
Tibbetts et al., 2001	MWNT	296	3.59	0.04
Wang et al., 1999	SWNT	80	10	2
Yang et al., 2000	Li-MWNT	~473-673	0.1	~2.5

Yang et al., 2000	K-MWNT	<313	0.1	~1.8
Ye et al., 1999	SWNT (high purity)	80	7.18	8.25
Yin et al., 2000	SWNT	300	16	6.5
Yoo et al., 2005	CNT	573	0.1	1.5
Zacharia et al., 2005	CNT (Pd doped)	300	2	0.66
	CNT (V doped)	300	2	0.69
Zhou et al., 2006	Activated Carbon	77	6	10.8
Zhu et al., 2001	MWNT	~290	~10	>3
Züttel et al., 2002	SWNT	~293	~0.1	<2

Table 2.1: Comparative table of the hydrogen storage capacities of various carbon nanostructures.

Numerical simulations of hydrogen storage have been mostly performed using molecular modeling. The three widely used techniques are the Monte Carlo (Guay et al., 2004), MD (Dodziuk and Dolgonos, 2002) and density functional theory approach. In the first two of these methods the interaction between the carbonaceous material and hydrogen is usually represented by a classical empirical potential function (Wang and Johnson, 1999b, Wang and Johnson, 1999a, Gordon and Saeger, 1999, Williams and Eklund, 2000, Bernholc et al., 1997, Rzepka et al., 1998, Darkrim and Levesque, 1998). Another frequently used approach accounts for the chemisorption process in CNTs. This

type of modeling requires that the electronic states be explicitly simulated. Examples of such simulations are available in the work by Lee et al. (2000) and Lee and Lee (2000).

Molecular simulations have contributed significantly to enhance fundamental understanding of the physical mechanisms and intermolecular forces that account for the considerable hydrogen adsorption/storage in carbon nanopores (Wang and Johnson, 1999c, Bernholc et al., 1997, Rzepka et al., 1998, Darkrim and Levesque, 1998, Wang and Johnson, 1999a). However, there are disparities in the results obtained by these methods that are mainly due to the potential function used and the geometry and chirality of the nanotube that are considered. These numerical approaches have not yet addressed some important issues that will be described in this dissertation. The most important of these is an investigation of the enhancement of the hydrogen storage capacity of a carbon nanopore/nanorope by making structural changes in the pore as well as in the overall nanostructure composition (for instance, by encapsulating selected metals within the nanostructure).

2. Carbon Nanofibers and Active Carbon:

Apart from single and multi-walled CNTs, there are other carbon nanostructures such as CNFs and activated carbon that can adsorb large quantities of hydrogen (Chambers et al., 1998, Fan et al., 1999, Gupta et al., 2000, Zhou et al., 2006, Panella et al., 2005). This is due to the large surface area of these nanostructures as well as the inherent strong attractive intermolecular force between carbon and hydrogen. Carbon nanofibers or graphitic nanofibers (GNF) are usually formed by the catalytic action of metals (like Ni, Co, Fe) on certain gas phase fullerenic species or carbon derivatives. A form of graphite called beta-graphite saturates out of the metal catalyst surface to form

the nanofibers. Carbon nanofibers are of three types, tubular, herringbone and platelet and have an interlayer distance of 0.355 nm just as in CNTs. (Chambers et al., 1998) have reported an unusually large amount of hydrogen uptake in nanofibers. They claimed that the material is able to adsorb 20 L of hydrogen per gram of carbon at 120 atmospheres and 25 °C, which is equivalent to more than 60% by weight. That claim has not been corroborated through experiments by other groups, which have produced different results (Ahn et al., 1998, Tibbetts et al., 2001, Orimo et al., 1999). The theoretical calculations of Li et al. (2003a) show that at room temperature the adsorption cannot exceed 7.7% by weight.

Activated carbon, such as AX-21, is a form of carbon with a high surface area and pore volume. Several experiments performed to measure the hydrogen adsorption in activated carbon have concluded that this form of carbon has a better adsorption capacity than even CNTs (Zhou et al., 2004a, Schimmel et al., 2004). While the surface area of the nanotubes is the highest at normal temperatures and pressures, at high pressures and/or low temperature, the surface area of activated carbon is much greater than that of the SWNTs. This is because of the bundling of the nanotubes at such conditions. Hence, at high pressures, activated carbon adsorbs more hydrogen than CNTs (Schimmel et al., 2004).

2.4.3. Means of Enhanced Storage

The goal of current research is to further explore additional ideas, since most experimental and theoretical investigations show that while carbon nanostructures are advantageous in comparison to other materials used for hydrogen storage, they are still unable to attain storage greater than desired limits, such as one set by DOE. Various

means have been proposed to increase the hydrogen storage capacity of carbon nanostructures. For instance, nanotube characterization has revealed that the ends of the nanotubes are covered with hemispherical fullerene caps (Hirscher et al., 2001). Thus, in order to enable the access of hydrogen into the interior of the tube, the end of the nanotube must be cut or opened (Liu et al., 1999, Stepanek et al., 2000, Hirscher et al., 2002, Darkrim and Levesque, 2000). While nanotubes with open ends can be synthesized, those with closed ends can be cut open by either exposing a nanotube to ultrasonic treatment (Dillon et al., 1997) or by ball milling. The closed ends of the nanotubes are also susceptible to being opened by oxidation because of the strained nature of the rings (Thess et al., 1996, Tsang et al., 1993, Ajayan et al., 1993). A dilute solution of an acid can be used to sonicate the nanotube sample and open its ends by oxidation. Some reports on high hydrogen adsorption properties of sonicated nanotubes by Dillon et al. (1997) have been put in doubt by Hirscher et al. (2001) who claimed that the high adsorption was due to the Ti particles that were trapped in the nanotubes during the sonication process in the titanium sonicator.

Ball milling is another method to remove the fullerene caps at the ends of nanotubes so as to enhance the hydrogen storage. Reactive ball milling has shown that this strategy is effective. It is also an effective means to enhance storage in other carbon nanomaterials (Awasthi et al., 2002). The process of ball milling destroys the crystalline structure at places and opens up traps for hydrogen storage. This is an interesting issue that can be resolved by careful simulations of carbon nanostructures that have purposefully inserted defects. The geometry of the nanotubes also plays an important role in the storage capacity. The adsorption characteristic changes with variation of chirality

and diameter (Gu et al., 2001, Shen et al., 2004). The diameter of a nanotube changes the packing geometry and hence influences the hydrogen take-up.

Carbon nanoropes and nanofibers, which are two-dimensional triangular lattices of SWNTs, have been found to have a larger storage capacity than simple SWNTs (Cao et al., 2001, Stan and Cole, 1998a, Zhu et al., 2001, Yin et al., 2000). This is due to a larger effective surface area that can be exposed to adsorption, since the interstitial space is also utilized for enhanced hydrogen storage. Careful modeling of these arrays of nanotubes requires a suitable choice of van der Waal's gap between the tubes. The van der Waal's gap changes with changing pressure and temperature conditions and so it is important to assume a realistic value.

Density functional theory investigations have shown that hydrogen storage is enhanced when the hydrogen molecules are dissociated into atoms (Han and Lee, 2004). Atoms can easily penetrate the CNT pores and get chemisorbed as well (Haluska et al., 2004). This can be achieved either at low temperature and high-pressure conditions or through catalysis by metals (Yoo et al., 2005). Thus hydrogen storage capacity of carbon nanostructures increases at high pressures (Tarasov et al., 2003, Volpe and Cleri, 2003) and low temperatures (Nishimiya et al., 2002). Experiments as well as molecular modeling studies have shown that at pressures much larger than atmospheric pressure, CNTs exhibit a higher hydrogen storage capacity, since at higher pressures hydrogen molecules are physisorbed in the interstices of the nanotubes as well as in the interior. While temperatures near cryogenic (77K) enhance hydrogen storage (Wang and Johnson, 1999b, Williams and Eklund, 2000, Meregalli and Parrinello, 2001), such low temperatures are not acceptable as practical operating temperatures.

Ci et al. (2003) have reported an enhancement in the storage capacity by annealing CNTs in the temperature range 1700-2200 °C. This is attributed to the modification of the grain structures for the as-synthesized nanotubes that use a floating catalyst. In addition, since as-synthesized CNTs have a variety of functional groups attached to their surfaces that can retard the process of hydrogen adsorption by reducing the available surface area, heat treatment removes these groups and thus increases hydrogen adsorption.

Carbon nanotubes also have enhanced storage capacities when they carry a charge (Simonyan et al., 1999) or have encapsulated metal nanoparticles (Endo et al., 2003). This is due to the increased electrostatic interaction between the fluid and solid phases as well as due to dissociation of hydrogen molecule into atoms. Insertion of Pt, Li, Rb (Che et al., 1999), Cs, K (Gao et al., 1998), and Ni (Shaijumon et al., 2005) induces a charge on the nanotubes. The insertion of K or Cs leads to an excess negative charge of about $-1e$ per 8 C atoms (Grigorian et al., 1998) that leads to increased hydrogen adsorption. Alkali metals (such as Li) doped CNTs also display a marked increase in hydrogen storage at room temperature (Chen et al., 1999).

Experiments have shown that CNTs can electrochemically store relatively large amounts of hydrogen (Heremans, 1985, Nutzenadel et al., 1999, Rajalakshmi et al., 2000, Chen et al., 2004b). As-synthesized CNTs have been used as electrodes that can be charged and discharged in cycles. Rajalakshmi et al. (2000) have used an 80% pure nanotube sample and reported hydrogen storage of up to 2.9 weight %. They observed that the maximum storage was reached after about 20 cycles of charge and discharge. Lee

et al. (2000) further identified adsorption sites on the exterior, interior of the nanotubes, as well as in the interstices of bundles of nanotubes.

Hydrogen spillover is an important phenomenon where hydrogen molecules are first adsorbed by metal atoms and later desorbed and physisorbed by carbon atoms (Zacharia et al., 2005). The experimental results have shown that multi-walled nanotubes (MWNTs) synthesized by metal oxide catalysts have a large hydrogen adsorption capacity. The active temperature range for adsorption is 25 to 100 degrees C, which is useful for practical applications. Callejas et al. (2004) have investigated an effect similar to spillover and reported the enhanced storage of around 3% by weight at 77K and 0.04 MPa.

Recently, Yildirim and Ciraci (2005) have reported enhanced hydrogen storage by coating a SWNT with Ti atoms. They claimed that each Ti atom binds with up to four hydrogen molecules. The first hydrogen molecule is adsorbed by way of dissociation but the later adsorptions involve intact hydrogen molecules. They claimed hydrogen storage of up to 8%. Previous results have demonstrated an enhancement of storage in alkali-metal doped nanotubes (Chen et al., 1999) due to the catalytic action of alkali-metal ions in hydrogen dissociative adsorption. These findings support future investigations of hydrogen adsorption in nanotubes that contain encapsulated metal ions.

To summarize the results from the literature review presented in this section (and Table 2.1), current experimental results for hydrogen storage do not agree with each other. Thus, an accurate and reliable theoretical or numerical approach is required to understand these discrepancies.

2.5. Carbon Nanotube Growth Mode

The first detailed observation of the synthesis and growth of graphitic CNFs (“filamentary carbon”) was made by Baker *et al.* by decomposing acetylene in the presence of a nickel catalyst (Baker, 1989). A catalytically active transition metal nanoparticle (i.e., of Fe, Ni and their alloys, such as stainless steel) can be created through the initial formation of a carbon deposit. This deposit develops in a reducing environment that has high gas-phase carbon activity at elevated temperatures (Sacco *et al.*, 1984), (Kock *et al.*, 1985). The deposited carbon diffuses into the catalyst nanoparticle, nucleates within it, and emerges in the form of CNTs or nanofibers (CNFs). The subsequent catalyzed growth of CNTs and CNFs occurs mainly through two modes. The base growth mode arises when the metal nanoparticle catalyzing the growing carbon nanostructure remains at the bottom of the nanotube. For this type of growth the adhesive forces between the substrate and the catalyst nanoparticle are typically too large for the particle to be lifted as the CNT/CNF grows. Alternately, the catalyst nanoparticle is lifted by the growing carbon nanostructure during tip growth, and remains at the tip of the CNT/CNF after its growth ceases.

The experimentally observed base growth mode by Wu *et al.* was facilitated by an Fe catalyst immersed in C_2H_4 with a ~ 162.86 torr partial pressure and 1048 K temperature (Wu *et al.*, 2008). The other gaseous species were H_2 (carrier gas) and Ar (inert). The experimental results of Ducati *et al.* revealed a predominance of vertically aligned CNTs grown through a tip-growth mode with Ni as catalyst and C_2H_2 as the carbon source gas at a temperature of 823 K and 1.5 torr partial pressure (Ducati *et al.*, 2004). However, experimental results related to growth mode of CNTs show wide

variation. Hence, it is important to develop a simulation tool to successfully predict the growth mode of CNT at various conditions. Molecular dynamics simulation results that predict the growth mode of CNTs is presented in this dissertation.

2.6. Nanoscale Heat Transfer at Solid-Fluid Interfaces

The application of MD and NEMD has found wide usage in the determination of thermal properties of Silicon (Kebblinski et al., 2002) and the effects of grain size (Bodapati et al., 2006, Tang and Yao, 2006) and phonon scattering (Schelling et al., 2004) on thermal resistance across grain boundaries have also been explored. The interest in studying interfacial thermal transport using NEMD has received considerable attention for solid-solid interfaces (Stevens et al., 2007) as well as for interfaces between liquids (Patel et al., 2005) and thin films (Twu and Ho, 2003, Angadi et al., 2006, Hegedus and Abramson, 2006, Chiritescu et al., 2007).

There is, however, limited literature that have addressed a basic understanding of thermal transport phenomenon between simple solid-fluid interfaces and the bonding between liquid and solid atoms (Xue et al., 2003, Xue et al., 2004) using a simple model of alternate liquid and solid blocks. Recent study of heat transfer through a solid trapped between liquid region shows that the structural details exercise an effect on the thermal properties of solid (Chaudhuri et al., 2007a). Non-equilibrium MD is the simulation technique applied for the study of simple solid-fluid interfacial heat transfer phenomena. Also, the dependence of thermal slip on interaction at the interface has been discussed in literature (Khare et al., 2006).

Since the length scales associated with nanostructures are comparable with those of the energy carriers that facilitate thermal transport, the corresponding nanoscale

properties are different from those at the continuum. The role of the interfacial resistance (Swartz and Pohl, 1989) during nanoscale thermal transport thus also differs from its characteristics at larger scales (Cahill et al., 2003). Moreover, the structural details of a nanoscale interface have a significant influence on the local thermal properties. The attraction of liquid molecules to hydrophilic surfaces promotes structural ordering at interfaces, which enhances the local thermal conductivity (Murad and Puri, 2008, Henderson and Vanswol, 1984). There is also evidence that the local intermolecular interactions can introduce temperature discontinuities across these interfaces (Khare et al., 2006). Kapitza first discussed the existence of an interfacial contact resistance during heat transfer between liquid helium and heated metal surfaces such as copper and lead (Kapitza, 1941). The interfacial (Kapitza) resistance,

$$R_k = \Delta T / \dot{q}, \quad (2.2)$$

represents the ratio of the temperature drop at the interface to the normal heat flux across it (Barrat and Chiaruttini, 2003, Pollack, 1969). Thermal transport across nanoscale solid-fluid interfaces, e.g., those formed when nanoparticles and nanostructures are immersed in fluids, is also influenced by the locally large surface area to volume ratio (Eastman et al., 2004).

In summary, the literature provides some information and results on nanoscale heat transfer at solid-fluid interfaces. However, a lot of the research on nanoscale thermal transport makes implicit assumptions of the validity of continuum scale relations. Also, not much research data is available on transient heat transfer. This dissertation presents comparison of heat transfer evaluated from MD simulations with that obtained from continuum scale assumptions.

Chapter 3: Ion Adsorption in Carbon Nanotubes

3.1. Introduction

It is important to characterize the ion-channel interaction (Akita et al., 2001, Qiao and Aluru, 2005) to properly understand electro-osmotic flows in electrically charged nanochannels. While techniques for the encapsulation of particular species have been proposed (Petsev and Lopez, 2006, Karnik et al., 2005) none seem to be based on a generic controlled intake method. Molecular dynamics simulations have been used to demonstrate the utility of CNTs for water and ion separation (and subsequent encapsulation) from a salt solution.

The magnitude of the charge placed on each atom of a CNT provides a finite overall surface charge density. Three different electrostatic charge distributions on the nanotube (that can be implemented in applications (Chen et al., 2005, Zhao et al., 2002)), as shown schematically in Figure 3.1, have been considered:

1. First, the CNTs are assumed to behave as conventional electrodes for which one half of the nanotube atoms have a positive charge (on the positive electrode) with negative charges on the other half (that acts as the negative electrode).
2. Next, the CNTs are assumed to contain alternate axial bands of positive and negative charges along the length of each CNT in the form of lengthwise arrays of charged carbon atoms.
3. Finally, rings of alternate positive and negative charges arrayed along the circumferences of the CNTs are considered. (The conventional electrode discussed above is a special case of this configuration. As a consequence of the

imposed periodic boundary conditions with regards to the position of the atoms, such an electrode is essentially a single nanotube divided into two halves, one charged positive and the other negative.)

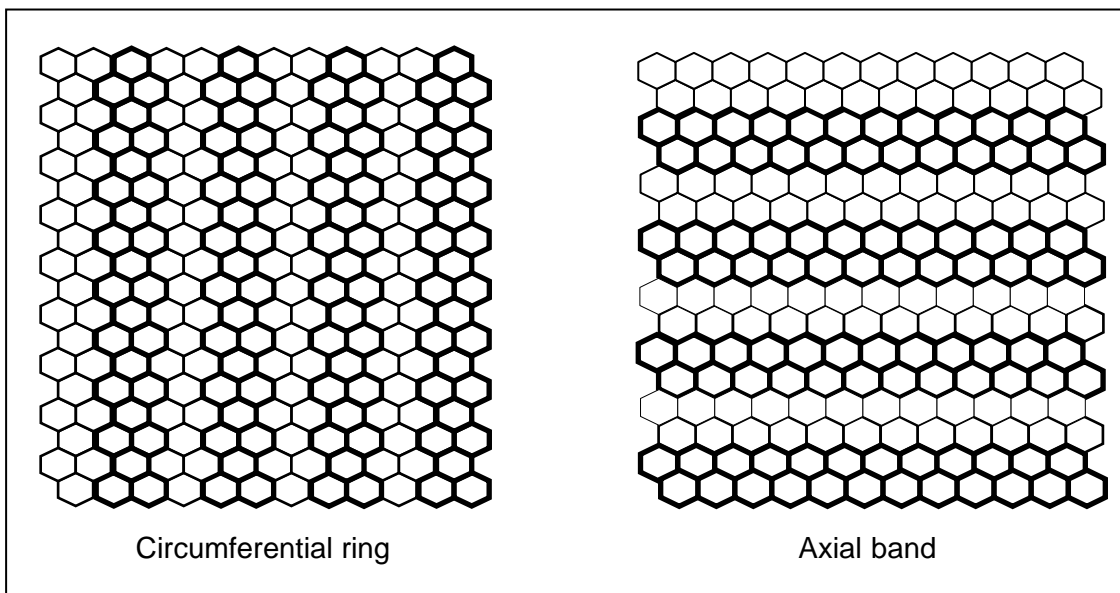


Figure 3.1: Schematic diagrams of the simulated charge distributions. (The deeper shade corresponds to a negative charge on a carbon atom while the lighter shade is for a positive charge.)

3.2. Methodology

The MD method that has been used is based on an extension of a technique developed to investigate confined fluids. This method has been used to investigate a variety of static and dynamic properties of fluids in nanopores (Murad et al., 1993, Lin and Murad, 2001, Murad et al., 1998, Murad et al., 2003) and it has been demonstrated that osmosis, reverse osmosis, ion-exchange and gas separations can be observed in a simulation that uses this technique for both nonpolar, polar and electrolyte solutions.

These studies have clarified many issues related to the separation of ionic solutions using reverse osmosis, ion exchange, and gases using zeolite membranes.

Molecular dynamics simulations are widely used in nanofluidics (Qiao and Aluru, 2005, Duren et al., 2002, Hanasaki et al., 2004) because usual continuum scale simulations do not accurately predict the flow characteristics (Qiao and Aluru, 2005). The MD simulations are based on a method used to investigate osmosis (Murad and Lin, 1999, Murad and Lin, 2002). Two (10,10) single-walled armchair CNTs of 1.375 nm diameter, 1.122 nm length, and 2.49 Å pore size are considered. In the simulation, the nanotubes are placed in a 2.75 x 2.75 x 3.366 nm box. The carbon atoms of each nanotube are placed at their known equilibrium positions using a simple harmonic-type tethering potential that approximately corresponds to the atoms' vibrational frequency. The CNTs in the cuboid domain are initially surrounded by a uniform (13.96% or 8.03% by weight) aqueous sodium chloride solution. Periodic boundary conditions on the position of the atoms are used in all directions to eliminate surface effects. Hence, the system is effectively infinite in all directions as shown in Figure 3.2. Due to these periodic boundary conditions, the nanotubes on the two opposite sides of the cuboid shaped domain are essentially joined end to end in the form of a single CNT.

A typical simulation considers 1302 molecules/atoms in a cyclically replicated cuboid, of which 400 atoms constitute the CNTs. There are 41 ions each of sodium and chloride with an additional 820 water molecules. A Gaussian thermostat maintains constant temperature (Allen, 1987) and the molecules initially have a Gaussian velocity distribution corresponding to the system temperature, which is 300 K. The timestep for all the simulations is constant throughout and has a value of 1 fs.

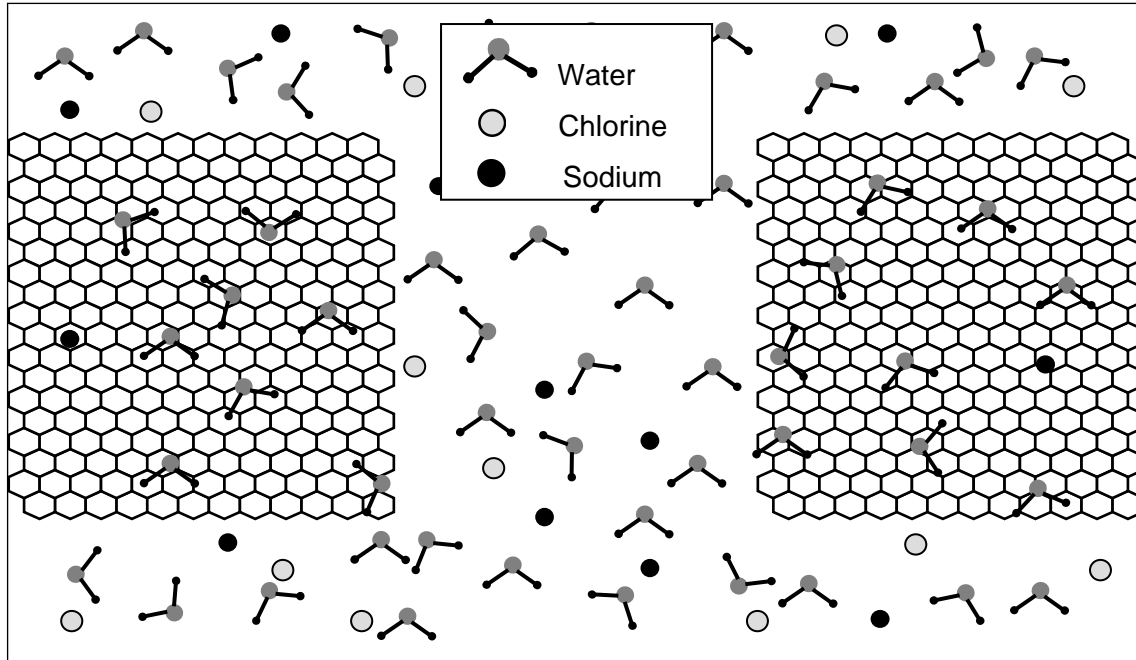


Figure 3.2: Schematic diagram of the simulated system.

The solution density determines the length of the solution compartment in the direction that is parallel to the axis of the CNTs. The 8.03% and 13.96% solutions have densities of 1054.42 kg/m^3 and 1097.9 kg/m^3 , respectively. The other two dimensions are fixed at 2.75 nm in order to ensure that the CNTs are completely immersed in the solution. A fifth-order Gear predictor–corrector algorithm is used to numerically model translational motion and a fourth-order predictor–corrector algorithm for rotational motion using the quaternion method (Allen, 1987, Evans and Murad, 1977). The size independence of the simulations is verified by considering a larger domain that had double the volume of a smaller test domain. It consisted of 1700 water molecules, 85 ions each of sodium and chlorine, and 400 carbon atoms (that made up the CNTs). The nanotube size, fluid density, temperature and sodium chloride solution concentration

were identical to the typical simulations in the smaller domain. The results of both simulations agreed closely and there was at most a difference in water intake of 9 molecules.

Established models for water, ions and carbon pores (Berendsen et al., 1981, Chandrasekhar et al., 1984, Turner et al., 2002) have been chosen to simulate the nanoscale system under consideration (described in Figure 3.2). Water was modeled using the simple point charge (SPC) model (Berendsen et al., 1981), ions with the so-called primitive intermolecular potential model (Chandrasekhar et al., 1984, Turner et al., 2002, Jorgensen et al., 1982) and CNTs using the parameters provided in Ref. (Turner et al., 2002). All site-site interactions in the present study were thus modeled using the LJ potential model with the Coulombic potential term, as described earlier in Eq. (2.1). The potential parameters σ and ϵ , and charges q were obtained from the literature. These models have been shown to closely represent experimental geometries, energies of ion-water complexes, and energies of solvation, etc. (Chandrasekhar et al., 1984). Lorentz-Berthelot mixing rules were used for cross interactions (Allen, 1987) and the reaction field method, with a cut-off radius of 9.5 Å, was used to model long range interactions (Watts, 1974, Tironi et al., 1995). It has been verified that the transport processes taking place in the simulations are insensitive to cut-off radii greater than the one used here. The parameters σ_{ii} and ϵ_{ii} used in the present study are given in Table 3.1. The cross interaction parameters σ_{ij} and ϵ_{ij} are obtained from Lorentz-Berthelot mixing rules, $\sigma_{ij} = (\sigma_{ii} + \sigma_{jj})/2$, $\epsilon_{ij} = \sqrt{\epsilon_{ii}\epsilon_{jj}}$.

Molecule	Interacting sites	σ (Å)	ϵ (kJ/mole)	q (e)
Water	H	3.17	0.65	-0.82
	O	0	0	+0.41
Ions	Na	1.9	6.7	+1
	Cl	4.42	0.49	-1
Carbon	C	3.4	4.94	+/- 0.25

Table 3.1: Values of parameters used in the simulations for preferential ion intake.

3.3. Results and Discussion

The various charge patterns on the CNTs induce dissimilar effects on water (Qiao and Aluru, 2005) and ion separation, and change their intake effectiveness. The first observation from the results is that the alternate charge distributions (using the lengthwise axial band and round circumferential ring patterns) almost entirely inhibit ion intake into the nanotubes while allowing for water transport. In contrast, the conventional electrodes promote ion separation and both water and preferential ion transport. For all cases, charged CNTs behave as reservoirs for the intake of water and/or ions.

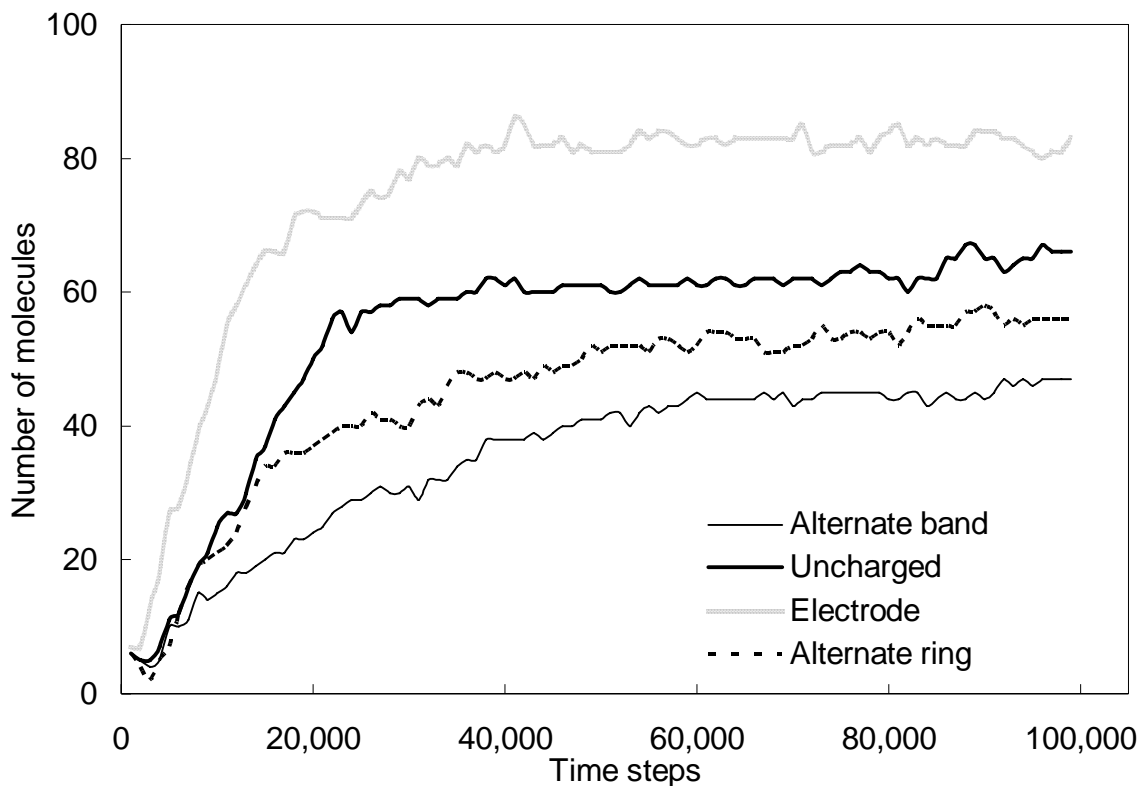


Figure 3.3: Water molecule intake by the nanotubes for different charge distributions. Initially, a 13.96% sodium chloride solution surrounds the carbon nanotube and the system is at ambient temperature and pressure. The surface charge density in each case (except for the uncharged nanotube) is 0.825 C/m^2 .

The number of water molecules inside a CNT reaches a saturation limit, as shown in Figure 3.3. (There, the charge magnitude on each CNT electrode is 0.125 times the electronic charge, i.e., $2 \times 10^{-20} \text{ C}$, resulting in a surface charge density of 0.825 C/m^2 .)

It is evident from Figure 3.3 that the maximum number of water molecules inside a nanotube occurs when it is used as a conventional electrode. The minimum intake takes place when an axial band charge pattern is applied. An uncharged nanotube contains more water molecules at equilibrium than when the CNTs are charged with either

alternate axial band or circumferential ring patterns due to the polar behavior of water molecules that act as dipoles due to small charges on the H (positive) and O (negative) atoms. As a result, water is both attracted and repelled by charged electrodes, whether positive or negative, while an uncharged CNT behaves neutrally. An uncharged nanotube surface has a graphitic structure and is thus hydrophobic. When charged, water molecules are attracted to the nanotube wall due to Coulombic interaction that can thus be made hydrophilic as suggested by experimental results (Valentini et al., 2005). In the case of an electrode, the nanotube wall is homogeneously charged. Hence, depending on the local charge, either a hydrogen or oxygen atom in water orients itself towards the wall (Qiao and Aluru, 2005, Valentini et al., 2005), which makes the nanotube surface less hydrophobic and more hydrophilic thereby increasing the water intake. When the carbon atoms are charged in the form of alternate bands or rings, the charge distribution does not assist the geometric structure of a water molecule. Consequently, partially positive hydrogen or partially negative oxygen atoms do not become oriented end-to-end efficiently, which decreases water intake.

The conventional electrodes have a larger intake of water molecules than uncharged CNTs, since the negative electrode and positive electrode, respectively, attract the sodium and chloride ions. As these ions move into the negative electrode and positive electrode CNTs, they drag the polar water molecules with them. Thus, two types of nanotube configurations are possible (which are differentiated by the charge pattern), one for separating ions using conventional electrodes and another to separate water from a salt solution (or conversely enrich the ion concentration within a solution by removing water molecules).

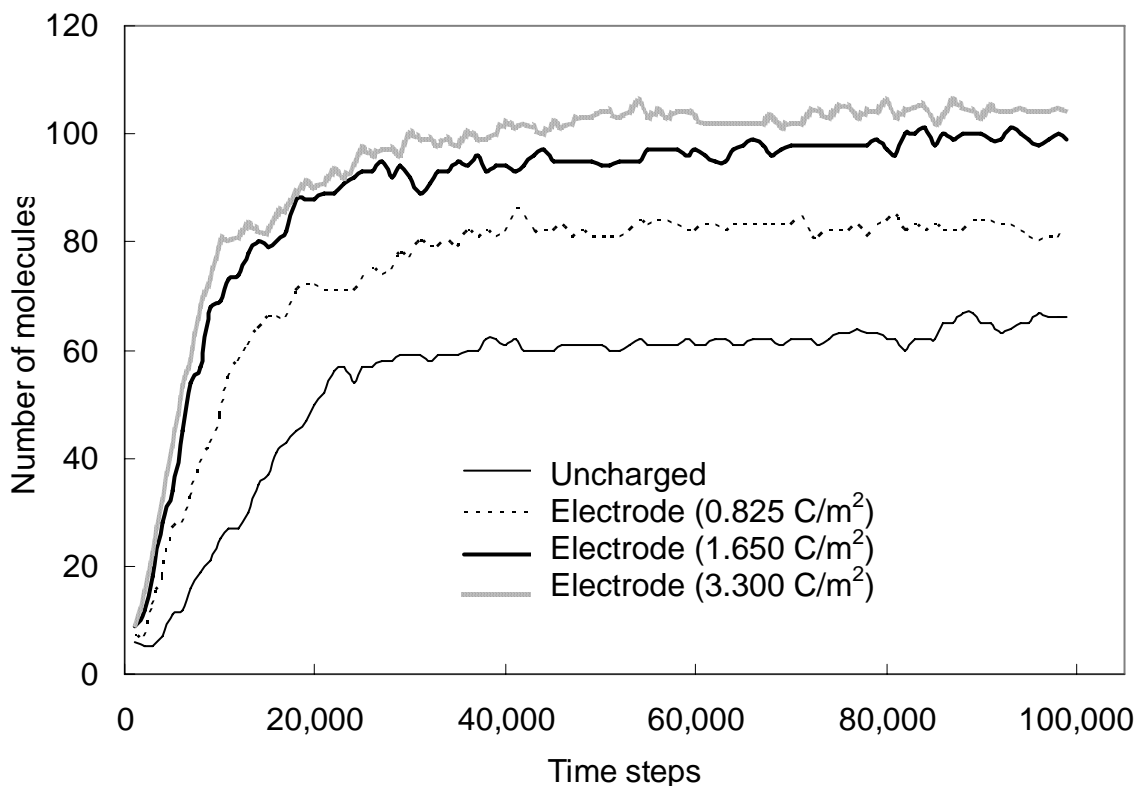


Figure 3.4: Water molecule intake by carbon nanotubes used as conventional electrodes for different charge densities, also for a 13.96% initial sodium chloride solution. The surface charge densities on the electrodes are zero (uncharged nanotube), 0.825 C/m^2 , 1.65 C/m^2 and 3.3 C/m^2 .

Figure 3.4 shows results for conventional electrodes with surface charge densities of 0.825 C/m^2 , 1.65 C/m^2 and 3.3 C/m^2 . (In comparison, the surface charge density of a sodium ion is 0.353 C/m^2 .) The number of water molecules inside a CNT increases with an increase in the surface charge density. The fractions of water molecules encapsulated inside the CNTs from the surrounding bath for the three cases are, respectively, 10.12%, 12.07%, and 12.68% (as compared to an 8.05% intake for an uncharged nanotube). For a 0.825 C/m^2 charge density, the encapsulated solution strength is 15.27%, which is more

concentrated than the residual solution external to the nanotube. Further, as the electrode surface charge density increases to 1.65 C/m^2 and 3.3 C/m^2 , this encapsulated solution strength also increases.

Due to its smaller size, the surface charge density of a sodium ion is about 5.4 times larger than of a chloride ion (0.065 C/m^2). Sodium has a higher absolute hydration enthalpy of -406 kJ/mol than chlorine (-363 kJ/mol) because of this larger charge density. Both sodium and chloride ions become hydrated and associate with water molecules in the simulations. However, a sodium ion-water cluster is structurally more rigid (due to the higher Na^+ surface charge density) than a corresponding chloride ion-water cluster so that the latter is the more flexible of the two. A sodium ion-water cluster has a size of $\sim 10 \text{ \AA}$ (Murad and Lin, 2002) while a typical chloride ion-water cluster is $\sim 13 \text{ \AA}$. While the diameter of a simulated CNT is 13.75 \AA , the available diameter for ion and water transport is smaller ($\sim 10 \text{ \AA}$) once the dimensions of the carbon atoms on the two opposite sides of the circular cross section are accounted for. Thus, a hydrated chloride ion-water cluster that is more flexible has a better chance of entering a nanotube since it can squeeze into it more readily. The higher surface charge density of the sodium ion and the relatively greater flexibility of the chloride ion-water cluster are therefore two competing factors that determine the relative uptake of these ions by the CNT. This hypothesis is in agreement with the simulation results.

Figure 3.5(a) and (b) show that, for all the different charge patterns on the CNT, the number of chloride ions absorbed inside the nanotube is greater than or equal to the number of sodium ions absorbed for lower surface charge densities (uncharged or 0.825 C/m^2). Thus, the relatively higher flexibility of the chloride ion-water cluster is the

dominant factor in case of lower surface charge density on the CNTs. The concentrations of sodium ions in mass percent in the negative CNT electrodes are 5.79%, 10.40% and 26.24%, respectively, for surface charge densities of 0.825 C/m², 1.65 C/m² and 3.3 C/m². For the same surface charge densities, the chloride anion concentrations in the CNTs are 10.60%, 12.21% and 18.50%, respectively. Clearly, as compared to sodium ions, the number of chloride ions is larger, for a surface charge density of 0.825 C/m² and lower when there are higher surface charge densities on the CNT electrodes. Thus, in case of electrodes with higher surface charge densities, such as 1.65 C/m² and 3.3 C/m², the larger surface charge density of the sodium ion is a dominating factor due to the presence of a relatively stronger electrostatic field due to the presence of the charge on the surface of the CNTs. Consequently, the number of sodium ions entrapped in the CNT is larger. These results show that a charged nanotube can be utilized to separate and encapsulate water and/or ions from a surrounding solution. Further, the ion adsorption can be modified quantitatively by varying the CNT surface charge density.

The numbers of sodium and chloride ions entering the CNTs for different charge distributions are shown in Figure 3.5(a) and (b), respectively. Figure 3.5(a) shows that the number of sodium cations encapsulated inside a CNT is highest when a conventional electrode is used. This is due to the electrostatic attraction force between the negatively charged nanotube wall and the sodium ions (Arista, 2001).

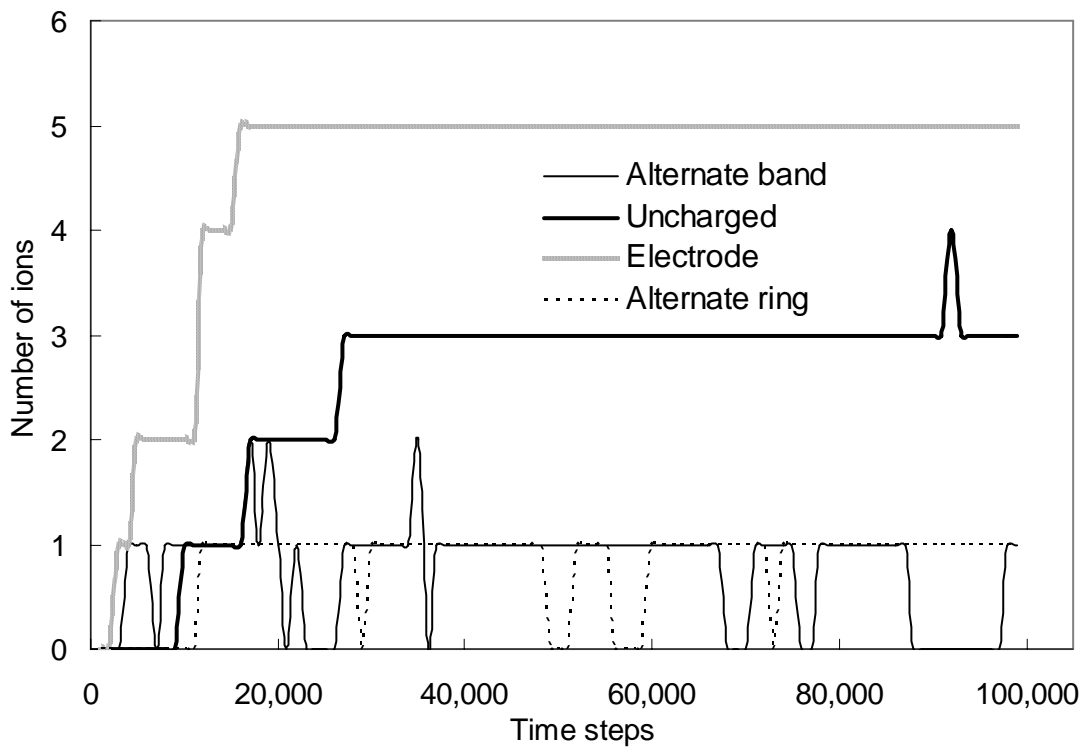
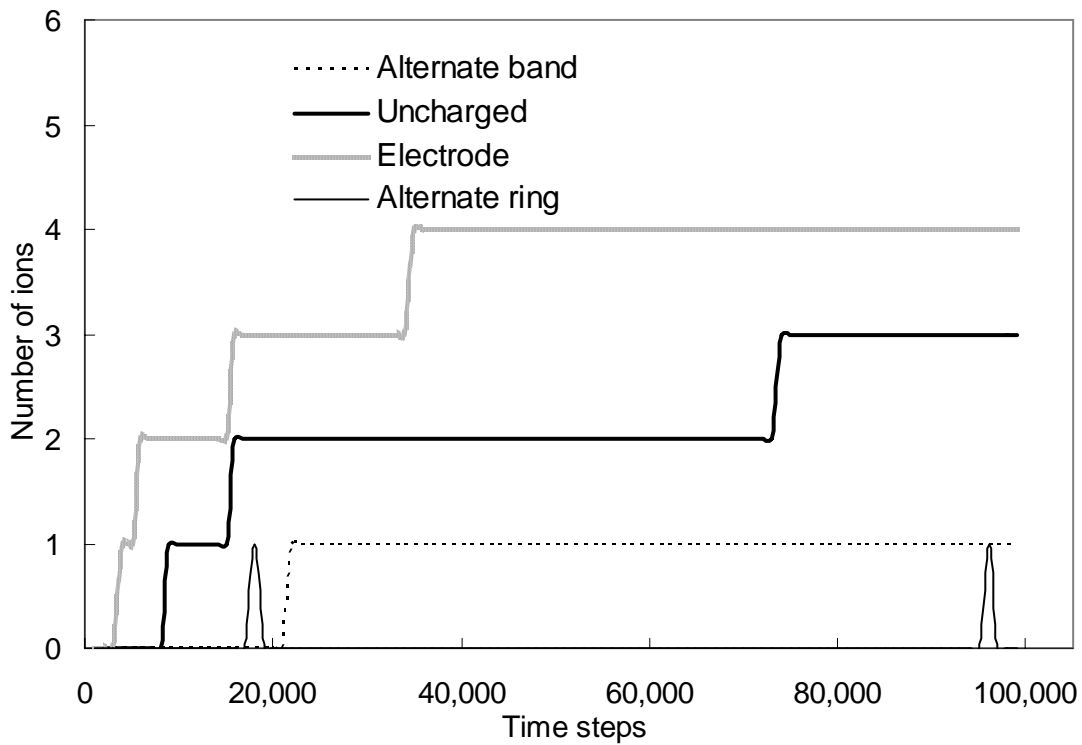


Figure 3.5: (a) Sodium and (b) chloride ion intake by the nanotubes for different charge distributions and for conditions that are used to obtain the results in Fig. 3.3.

In case of uncharged nanotubes, some sodium ions do enter the nanotube along with water molecules due to the attractive force between the negatively charged oxygen at the center of a water molecule and a positively charged sodium ion. In case of the alternate band or ring pattern charges on the nanotube, the entry of sodium ions is restricted. Chloride ions behave similarly, as shown in Figure 3.5(b).

The selective intake of the ions by the nanotubes for three different charge patterns is shown in Figure 3.5(a) and (b) for a CNT surface charge density of 0.825 C/m^2 . With an alternate axial band pattern, at equilibrium only 2.44% each of sodium and chloride ions are found to enter the CNTs from the surrounding bath. With the alternate circumferential ring pattern no sodium ions and 2.44% chloride ions are encapsulated. The water intake for the two alternate patterns is 5.73% (band) and 6.83% (ring) of the initial surrounding solution. For the alternate bands, the encapsulated solution strength inside the nanotube is 6.9% as compared to the initial 13.96% NaCl solution outside it. The circumferential ring pattern is more effective at precluding ions. It completely disallows transport of chloride ions into the nanotubes and only a single sodium ion enters the nanotube, thus encapsulating a dilute 2.23% sodium ion solution in water. When the external solution strength is lowered to 8.03% for a CNT surface charge density of 0.825 C/m^2 , both the alternate band and ring charge patterns are more efficient at purifying water. In this case, there is an intake of only a single sodium ion and no chloride ions into the CNT for the axial band distribution, while there is no ion intake at all for the circumferential ring pattern.

Table 3.2 summarizes the results for various surface charge patterns. The results suggest that spatially alternating charge patterns placed on CNTs favor water intake but

significantly inhibit ion encapsulation. In order to verify whether these effects also occur if the charges alternate temporally, the surface charge density (0.825 C/m^2) on a conventional electrode was alternated every 0.2 picoseconds, i.e. the negative electrode periodically became a positive electrode and *vice versa*. Then, the electrode acted solely as a water intake device (with a 61 water molecule intake) and no ions were encapsulated.

Species	Ambient	Alternate band	Alternate ring	Electrode
Water	820	47	56	83
Sodium	41	1	0	4
Chlorine	41	1	1	5
Solution strength(%)	13.96	6.47	~3.4	~15.28

Table 3.2: Number of ions, water molecules, and encapsulated solution strength for various surface charge patterns. The surface charge density is 0.825 C/m^2 .

Chapter 4: Hydrogen Storage in Carbon Nanotubes

4.1. Introduction

Carbon nanotube is considered a prospective material for hydrogen storage. However, there is a wide disparity in the hydrogen storage measurements for SWNTs (Liu et al., 1999, Zhou et al., 2004a, Hirscher et al., 2003, Dillon et al., 2000). Reports of high storage capacities (Dillon et al., 1997, Chambers et al., 1998) remain uncorroborated (Hirscher et al., 2003, Pinkerton et al., 2000).

As described earlier in Section 2.4, some experiments imply that storage in CNTs is possible at levels above the minimum volumetric storage prescribed by DOE at moderate temperatures and ambient pressure (Wang and Johnson, 1999b, Dillon et al., 2000) but other investigations have found that a useful amount of hydrogen can only be stored at cryogenic temperatures and/or very high pressures (Liu et al., 1999). It has been suggested that some measurements erroneously provide a higher adsorption rate than is realistically possible (Hirscher et al., 2003), since the CNT storage capacity at normal temperature and pressure is limited (Becher et al., 2003).

The intent of the research presented here is to resolve this conflicting information using a fundamental molecular approach based on MD simulations, which are used to evaluate hypothetically possibilities that could enhance hydrogen storage in CNTs through changes in the ambient conditions and structural or surface modifications. The latter include formulating a linear CNT ensemble of closed- or open-ended CNTs joined with metal or carbonaceous interconnects (Chen et al., 1999, Sen and Puri, 2004) (as shown in Figure 4.2), or providing surface charges to the CNTs.

4.2. Methodology

To validate the results obtained from LAMMPS hydrogen storage in (10,10) armchair SWNT (diameter 1.375 nm) has been simulated using MD at 10 K for pressure ranging between 10 atmospheres (1.01 MPa) to 75 atmospheres (7.6 MPa). The same system has been simulated with the well-established MD code of Professor Murad. Figure 4.1 shows the storage isotherm. It can be seen that storage of more than 4% can be achieved at an extremely low temperature and high pressure although in reality such low temperatures (cryogenic) cannot be generally implemented.

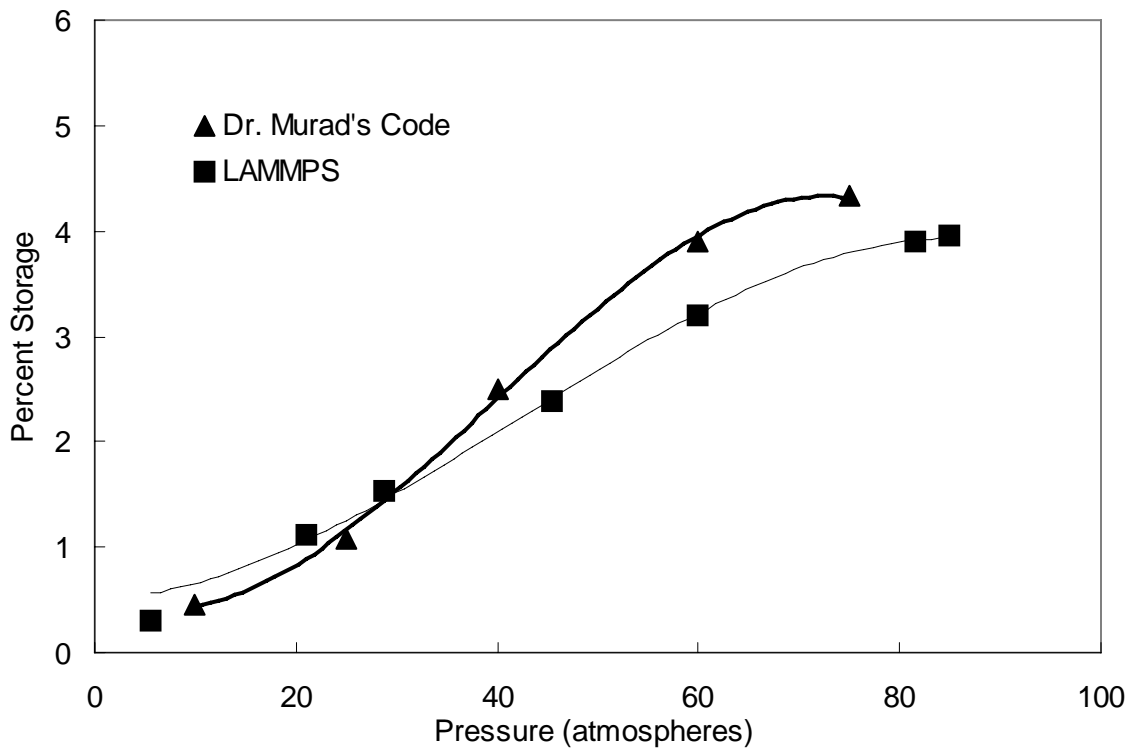


Figure 4.1: Comparison of result from Prof. Murad's Code with that of LAMMPS.

Figure 4.1 compares the results from Dr. Murad's code (Murad et al., 2003) to that obtained from LAMMPS. The external conditions of temperature and pressure were the same. The dimensions of the nanotubes were the same. Reasonable agreement is seen at pressures lower than 50 atmospheres. This pressure range (1 -50 atm) has been used for the hydrogen storage simulation using LAMMPS.

Various simulation techniques have been used for the molecular modeling of nanoscale adsorption, such as MD (Dodziuk and Dolgonos, 2002), Monte Carlo (Guay et al., 2004) and density functional theory (Tarasov et al., 2003). These can all illuminate the physical mechanisms and intermolecular forces that promote hydrogen adsorption/storage in carbon nanopores (Wang and Johnson, 1999c, Rzepka et al., 1998, Darkrim and Levesque, 1998). The interaction between a carbonaceous material and hydrogen is usually represented in MD simulations through an empirical potential function (Wang and Johnson, 1999c, Tarasov et al., 2003). The results presented here are from simulations that are based on the massively parallel LAMMPS code in which these interactions are modeled using a LJ potential that considers Coulombic interactions, as described earlier in Eq. (2.1). The parameters σ_{ij} and ϵ_{ij} , are obtained from the literature (Turner et al., 2002, Egorov et al., 2000, Mitchell et al., 2004) and are listed in Table 4.1 for various cases. The cross interaction parameters σ_{ij} and ϵ_{ij} are obtained from Lorentz-Berthelot mixing rules, $\sigma_{ij} = (\sigma_{ii} + \sigma_{jj})/2$, $\epsilon_{ij} = \sqrt{\epsilon_{ii}\epsilon_{jj}}$. A typical input file and a data file used for the simulations are included in Appendix A.

The simulation configuration is described in Figure 4.2. The cuboid 25.967 nm × 6.875 nm × 6.875 nm domain consists of two (10,10) single-walled armchair CNTs of

Molecule	Interacting sites	σ (Å)	ϵ (kJ/mole)
Hydrogen	H	2.915	0.3158
Ions	Li	2.27	0.016
	Ti	1.13	1608.0
	Pd	2.45	33.08
Carbon nanotube	C	3.40	0.2327

Table 4.1: Values of parameters used in the simulations for hydrogen storage.

1.375 nm diameter, 1.122 nm length, and 2.49 Å pore size that are surrounded by hydrogen. The system temperature is varied between 25 K and 470 K and the pressure varied between 10 and 50 atmospheres (or 1.01 MPa-5.05 MPa). A hollow nanowafers consisting either of metal ions or carbon connects the interiors of the two CNTs but it is not chemically bonded to them.

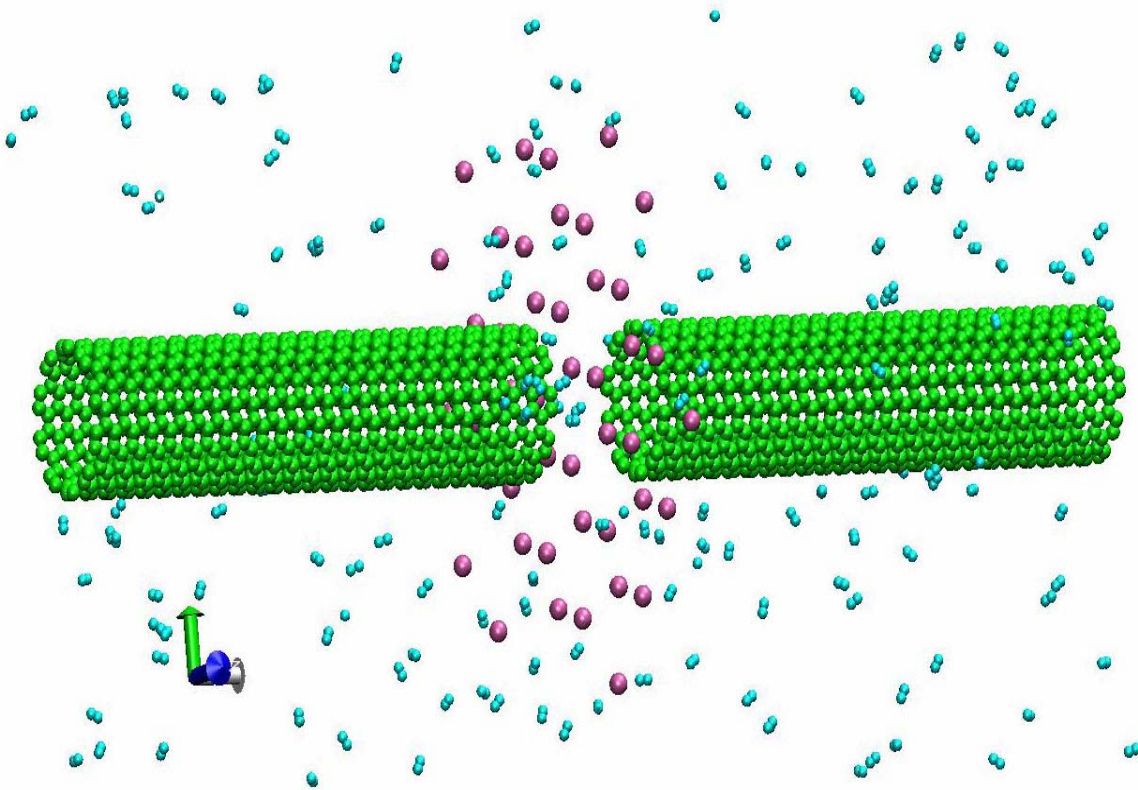


Figure 4.2: Schematic diagram of the simulated system. Interconnects made of Li-, Pd- and Ti-ions, and C atoms (purple) are used to join adjacent carbon nanotubes (green), surrounded by hydrogen molecules (blue).

When the nanowafer has metal ions, these are provided with alternate positive and negative charges that maintain overall charge neutrality. The carbon atoms in the CNTs are either uncharged, or carry positive (anode) or negative (cathode) charges. A circumferential pattern has been considered that consists of rings of alternate positive and negative charges that are arrayed along the circumference of the CNTs as described in Figure 4.4a. Periodic boundary conditions apply in all directions to eliminate wall effects so that the system is effectively infinite in all directions. The number of hydrogen

molecules depends on the external pressure and temperature, which at 10 atm and 273 K is 330. These molecules initially form an fcc lattice that equilibrates through the simulations. A Gaussian thermostat maintains constant temperature (Darkrim and Levesque, 1998) and the molecules have an initial velocity distribution corresponding to the system temperature. A cutoff distance of 9 \AA is used for both LJ and Coulombic forces. Results obtained by implementing the Ewald sum in selected cases are compared with those obtained with long-range cut-offs and no appreciable changes are detected.

Based on the equilibrium configuration, the number (hence mass) of hydrogen molecules that are either stored inside the CNTs or physisorbed on their surfaces has been calculated. Each data point in the plots presented in the next section represents results obtained from a single run of the MD simulation. One of the objectives of this research is to investigate the enhancement of storage inside and on the surface of the CNTs due to spillover of hydrogen (Zacharia et al., 2005, Lueking and Yang, 2002) in presence of metal ions. Hence, physisorbed hydrogen on the surface of the metal interconnect is not considered.

4.3. Results and Discussion

Figure 4.3 presents results for hydrogen storage in open-ended CNTs at 273 K and pressures in the range from 1 to 55 atm. The CNTs are uncharged and connected to a hollow nanowafer consisting of Li, Pd or Ti ions, or electrostatically inert C atoms. While the presence of Li ions is found to increase H₂ storage, in contrast with some earlier findings (Guay et al., 2004, Zacharia et al., 2005, Yoo et al., 2005) it is found that the heavier transition metals Ti and Pd do not enhance it. At 54.75 atm, Li ions augment storage by 12.33% (as compared to storage with a carbon interconnect). At that pressure,

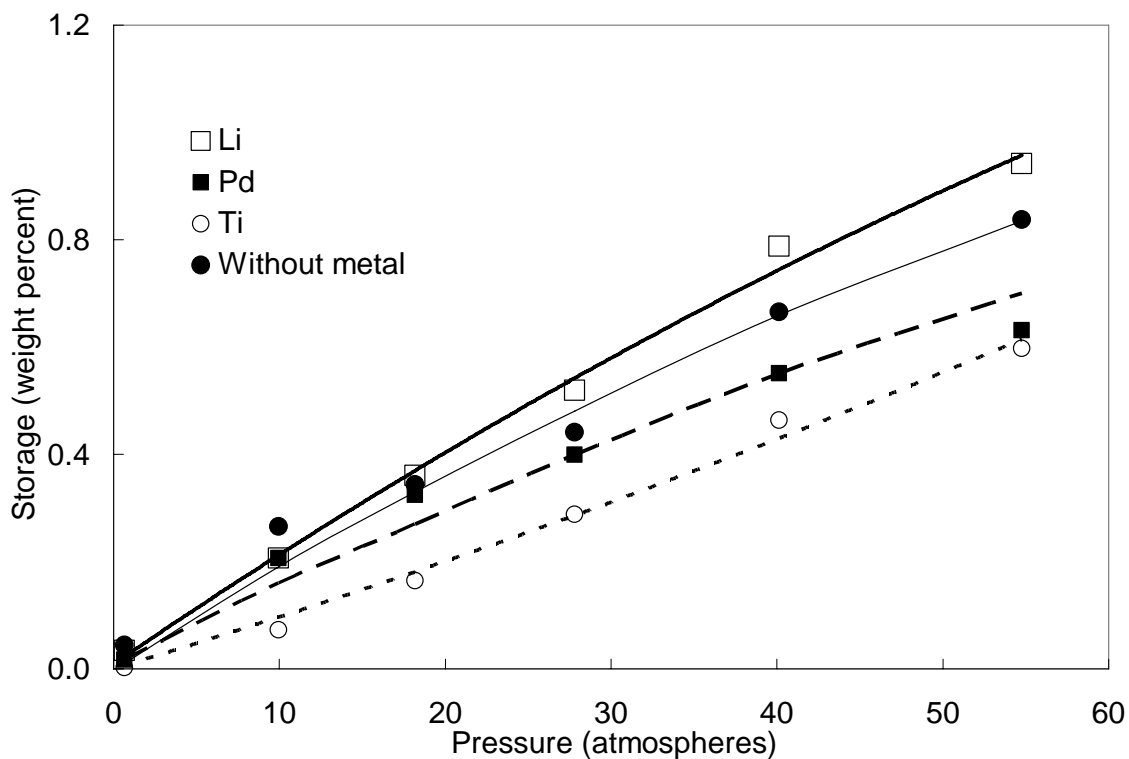


Figure 4.3: Variation of hydrogen storage with pressure at 273 K for various interconnect materials joining the carbon nanotubes.

a nanowafer containing Li ions also induces 57.48% and 49.11% more storage than the corresponding configurations containing Ti and Pd ions, respectively. The experimental finding that alkali metal ions have a positive influence on hydrogen storage in carbon nanostructures (Haluska et al., 2004) has been corroborated but it has been found that this enhancement is significant only at higher pressures (it is 1% by weight at 273 K). Surprisingly, however, it is found that a transition ion nanowafer interconnect placed between two CNTs diminishes H₂ storage.

Figure 4.4 presents the influence of electrostatic charges placed on CNT surfaces on hydrogen storage at 273 K when the nanotubes are joined by a Li ion interconnect or nanowafer.

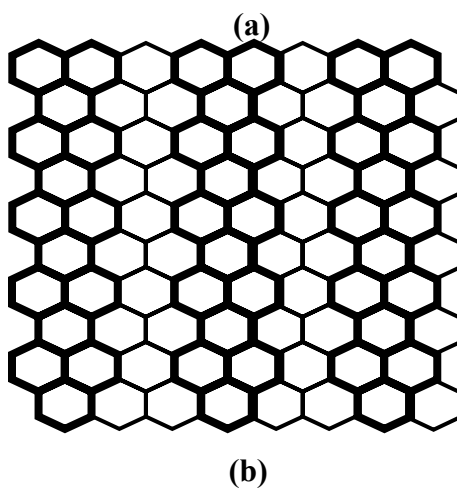
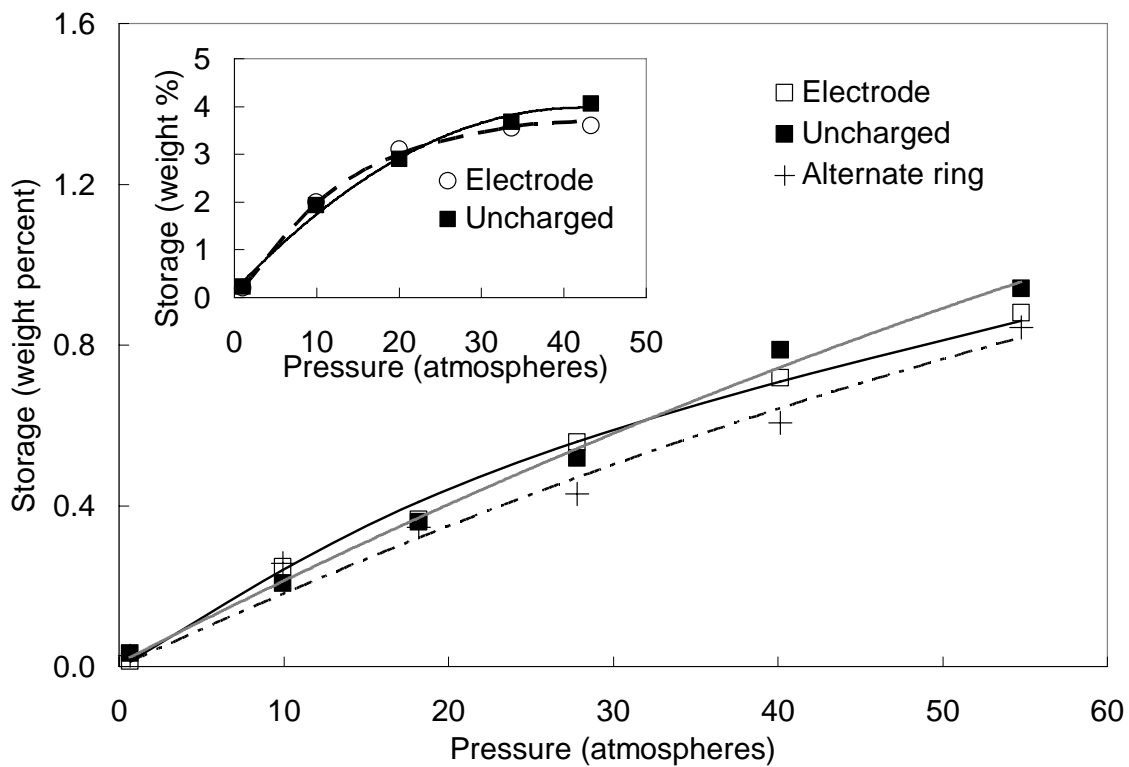


Figure 4.4: (a) Variation of hydrogen storage with pressure at 273 K in the presence of Li ion interconnects for various charge patterns on the carbon nanotubes. The plot in the inset presents similar results at 100 K. (b): Schematic of the circumferential ring type charge distribution (Banerjee et al, 2007). The dark lines represent sites with negative charges, while lighter ones represent positive charges.

The details for CNT electrodes and circumferential ring-type alternating charges (Banerjee et al., 2007) is described in the previous chapter and schematically described in the Figure 4.4a. At lower pressures, CNT electrodes store more hydrogen (resulting in a 20.27% enhancement at 9.94 atm) but at higher pressures, uncharged CNTs are more effective. At all pressures, the alternating circumferential ring charge induces the lowest storage.

The hydrogen molecule is charge neutral but has a dipole moment in the presence of charged surfaces (Toffolo et al., 2005). Hence, at lower pressures this molecule orients itself according to the electrostatic field (that is created due to the presence of charges on the surface of the CNTs), thereby increasing storage. In contrast, at pressures exceeding 35 atm (i.e., at higher densities) the average hydrogen-hydrogen and hydrogen-CNT intermolecular distance decreases so that the repulsion due to the Coulombic potential becomes more significant than the electrostatic attraction. Thus, hydrogen molecules are no longer able to orient themselves as they do at lower pressures. Additionally, the adsorbate-adsorbate (i.e., H₂-H₂) repulsion dominates in the presence of a charged surface when a hydrogen monolayer is present on the CNT surface (Yun and Gyeong, 2005). Hence, CNT electrodes exhibit lower storage at higher pressures.

The effect of increasing pressure on hydrogen storage at 100 K in the presence of a Li ion nanowafer interconnect is presented in the inset of Figure 4.4. It shows that higher pressures promote storage for both uncharged CNTs and CNT electrodes. Consistent with the results for 273 K, storage at higher pressures (> 22 atm) is greater for uncharged nanotubes than for electrodes. At lower pressures, storage is higher for CNT electrodes, e.g., at 20.06 atm storage is 6.94% greater with electrodes as compared to

uncharged CNTs. These results indicate that storage in the presence of Li ions depends upon both the pressure and the charge on the CNT surfaces.

Figure 4.5 and Figure 4.6 present the effects of temperature and pressure on hydrogen storage for three isobars (at 1, 5 and 10 atm) and two isotherms (at 273K and 100K) for uncharged CNTs connected by a Li ion nanowafer. Lower system temperatures promote storage as previously reported (Han and Lee, 2004). At 100K, the storage is almost 8.5 times greater at a 10 atm pressure as compared to that at 1 atm.

The volumetric storage density ρ is the storage per unit volume at a given temperature and pressure. A regression analysis to fit a curve through the data in Figure 4.5 and Figure 4.6 provides the relation

$$\rho_r \sim \frac{(p_r)^{0.8}}{(T_r)^{1.2}}, \text{ where } \rho_r = \frac{\rho}{\rho_0}, p_r = \frac{p}{p_0}, \text{ and } T_r = \frac{T}{T_0}, \quad (4.1)$$

which differs from the ideal gas law. This variation can be attributed to the van der Waals forces between the CNTs, metal ions and hydrogen molecules. In Eq. (4.1) ρ_0 , p_0 , and T_0 denote a reference density (at STP), pressure (1 atm) and temperature (273 K). In comparison with the ideal gas relation, the dependence of ρ on the temperature in Eq.

(4.1) is stronger than on the pressure. The slope of the isotherms $\left. \frac{\partial \rho_r}{\partial p_r} \right|_{T_r} = 0.8kT_r^{-1.2} p_r^{-0.2}$

varies as $\sim p_r^{-0.2}$ and, as seen in the inset in Figure 4.6, increases most rapidly in the range 0–40. When $p_r > 40$, the increase in slope tapers and becomes virtually linear, denoting diminishing returns for hydrogen storage with increasing pressure. The ideal value in this

context for $p_r \approx 40$ (or $p = 40$ atm). The slope of the isobars $\left. \frac{\partial \rho_r}{\partial T_r} \right|_{p_r} / 1.2kp_r^{0.8}$ varies as

$\sim -T_r^{-2.2}$, and decreases rapidly for $T_r > 0.6$ as demonstrated in the inset in Figure 4.6. This implies that storage increases most when $T_r < 0.6$ (or $T < 165$ K). This behavior can be utilized for the sequential adsorption (increasing p , decreasing T) and desorption (increasing T , decreasing p) of hydrogen. Decreasing the temperature however involves an additional energy input into the system, although it is one which could be harvested when the temperature is increased to desorb hydrogen.

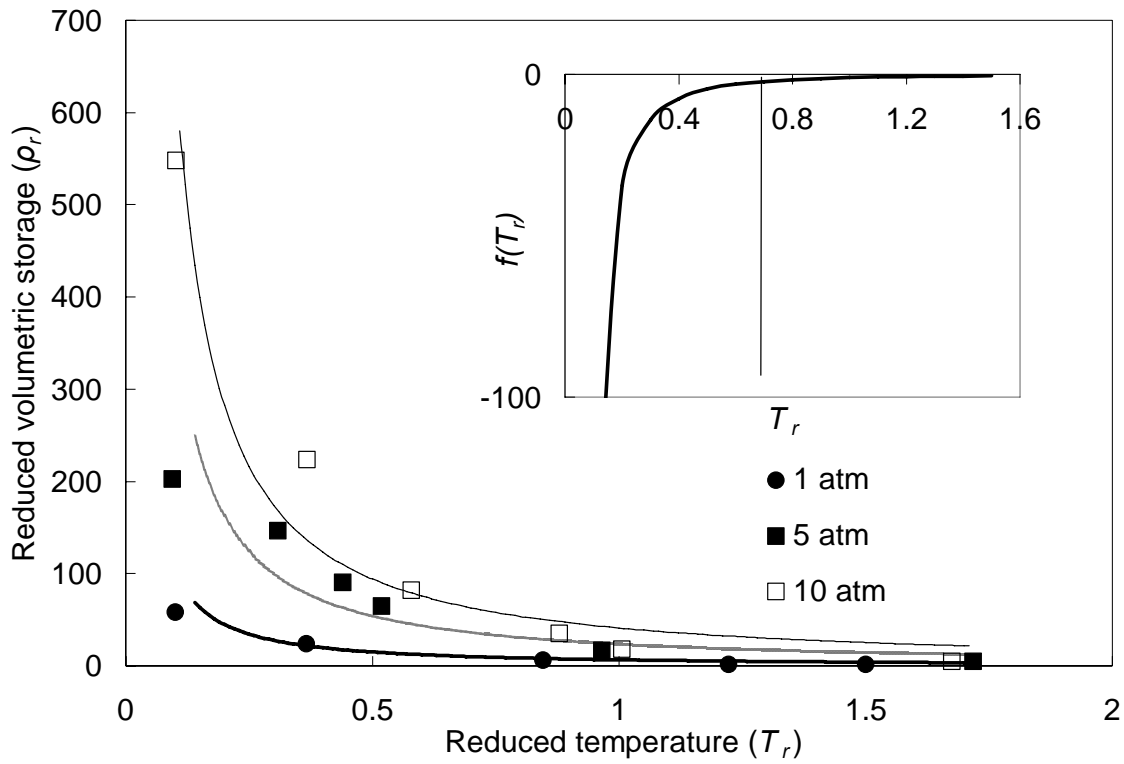


Figure 4.5: Hydrogen storage isobars for uncharged nanotubes in the presence of Li ion interconnects. The inset presents the slope of these isobars at various temperatures.

$$\text{Here, } f(T_r) = \left. \frac{\partial \rho_r}{\partial T_r} \right|_{p_r} / 1.2 k p_r^{0.8}.$$

Figure 4.6 shows that CNTs store significantly more hydrogen than can be compressed in an equivalent volume. For instance, at 273 K and 10 atm, volumetric storage in CNTs connected by a Li-ion nanowafer is 183% greater than for simply compressed hydrogen. While the mass density of compressed hydrogen increases linearly with pressure in accord with the ideal gas relation, the corresponding storage in CNTs is nonlinear.

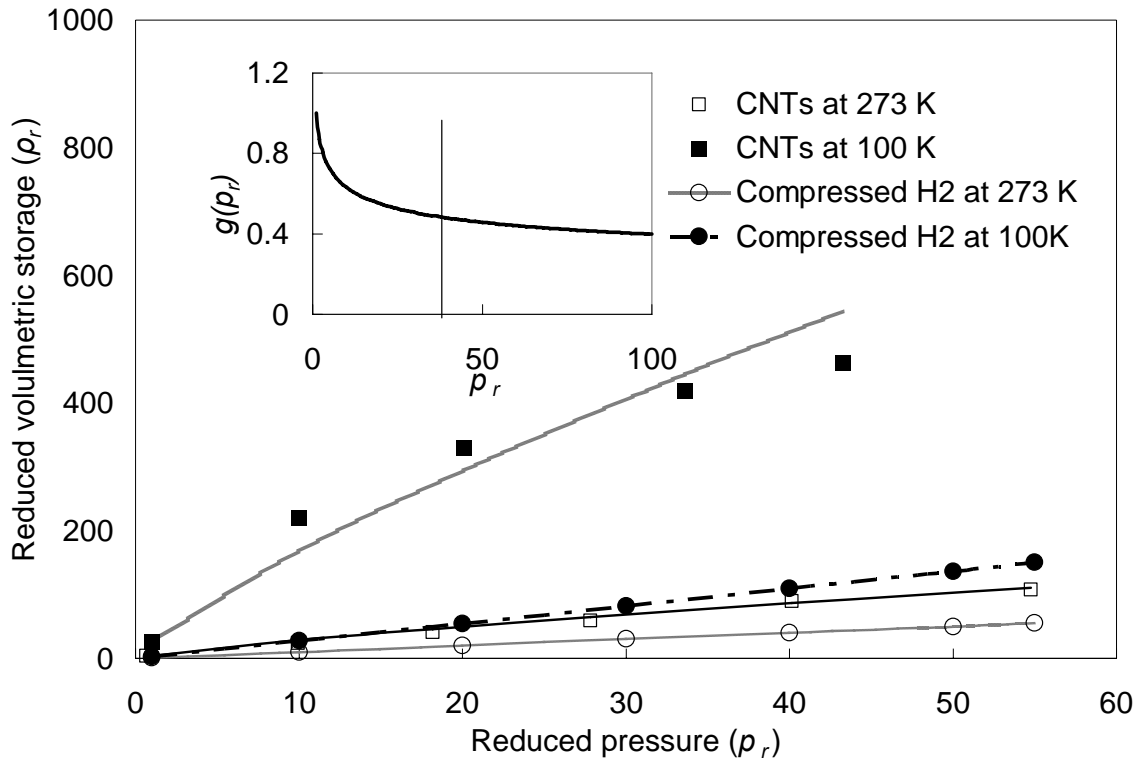


Figure 4.6: Hydrogen storage isotherms for uncharged nanotubes in presence of Li ion interconnects. The inset presents the slope of these isotherms at various pressures. Here,

$$g(p_r) = \left. \frac{\partial \rho_r}{\partial p_r} \right|_{T_r} / 0.8kT_r^{-1.2}.$$

A similar analysis is presented in Figure 4.7 and Figure 4.8 for uncharged CNTs connected by an uncharged C interconnect. A regression analysis suggests that

$$\rho_r \sim \frac{(p_r)^{0.35}}{(T_r)^{1.1}}, \quad (4.2)$$

which again differs from the ideal gas relation. Moreover, the exponents on the reduced pressure and temperature are different from those for Li ion interconnects under otherwise identical conditions. This suggests that hydrogen storage in the presence of Li ion interconnects is more sensitive to variations in the pressure and temperature.

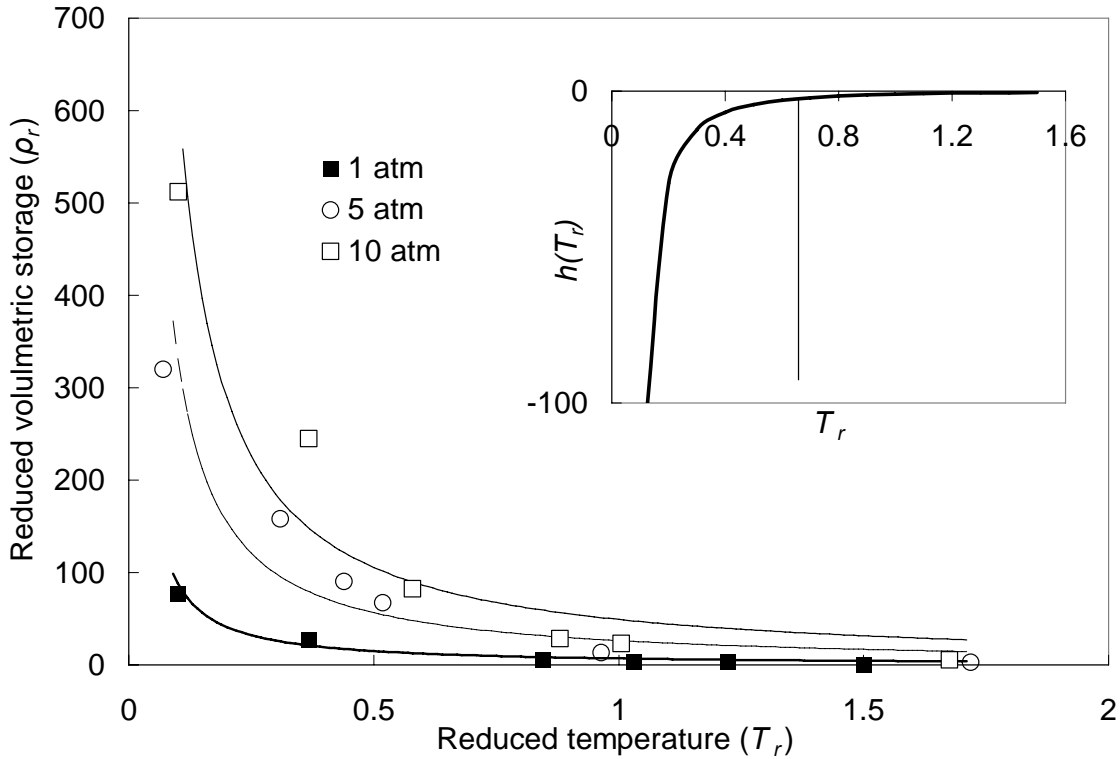


Figure 4.7: Hydrogen storage isobars for uncharged nanotubes in the presence of C interconnects. The inset presents the slope of these isobars at various temperatures.

Here, $h(T_r) = \left. \frac{\partial \rho_r}{\partial T_r} \right|_{p_r} / 1.1 k p_r^{0.35}$.

This is attributed to the higher physisorption binding energies in Li-doped CNTs as compared to pristine CNTs (Cabria et al., 2005).

Figure 4.7 and Figure 4.8 again show that hydrogen storage increases at higher pressures and lower temperatures. The correlation coefficients for the fitted curves in Figure 4.7 are 0.988, 0.995 and 0.9605 for the 1 atm, 5 atm and 10 atm isotherms respectively. The inset of Figure 4.7 shows the variation of the slopes of the isobars

$$\left(\frac{\partial \rho_r}{\partial T_r} \right)_{p_r} = -1.1k p_r^{0.35} T_r^{-2.1}$$

occurs when $T_r > 0.65$ ($T < 180$ K).

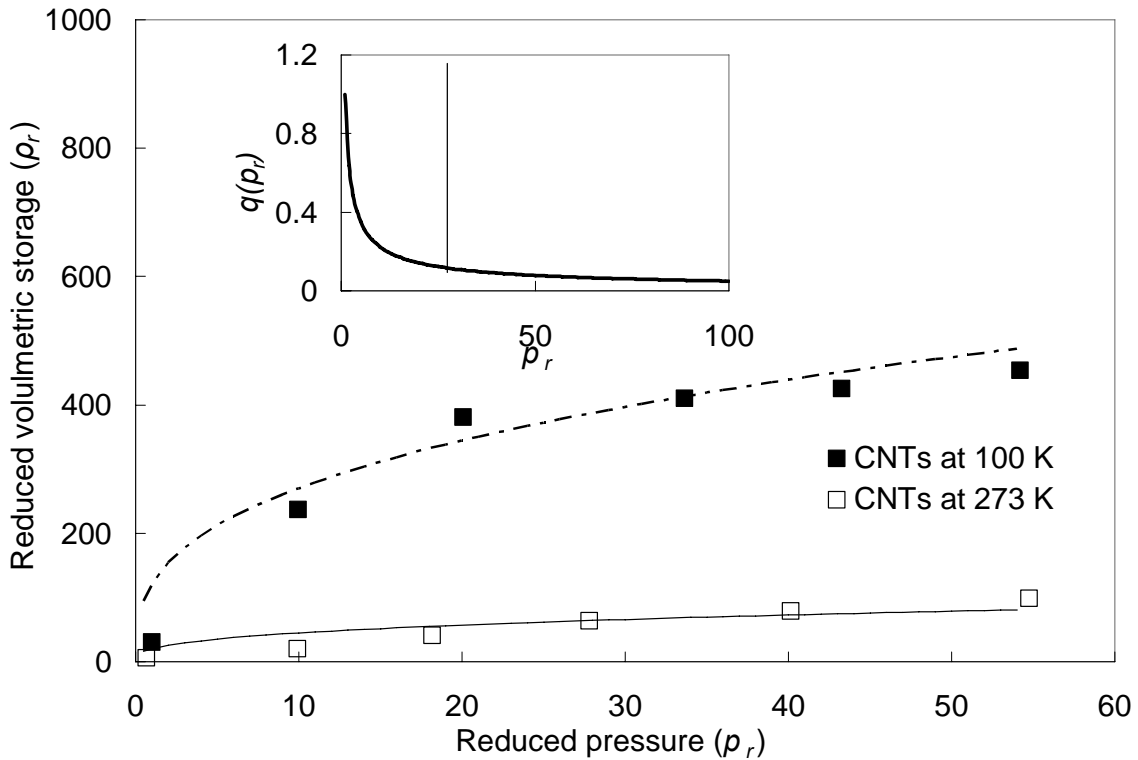


Figure 4.8: Hydrogen storage isotherms for uncharged nanotubes in presence of C interconnects. The inset presents the slope of these isotherms at various pressures. Here,

$$q(p_r) = \left. \frac{\partial \rho_r}{\partial p_r} \right|_{T_r} / 0.35k T_r^{-1.1}.$$

The dependence of storage on pressure with a C interconnect differs from one in which Li ions are present, as shown in Figure 4.8. Since the exponent on the pressure term is small (0.35), the slope of the isotherm ($\left. \frac{\partial \rho_r}{\partial p_r} \right|_{T_r} = 0.35kT_r^{-1.1} p_r^{-0.65}$) is almost linear (inset of Figure 4.8) when $p_r > 25$ (or $p > 25$ atm). The chemical stability of Li-doped CNTs produces a wider pressure range over which H₂ storage increases appreciably (Chen et al., 1999). Despite the qualitative similarities in storage when the two interconnects are used, the optimal storage conditions when C interconnect are employed are different from those containing Li ions.

Whether a CNT is open or closed also plays a role in storage. Figure 4.9 compares storage at two temperatures (100 K and 273 K) in CNT electrodes with either open or closed ends joined by a Li ion nanowafer interconnect. At 273K and ~20 atm, storage in open CNTs is 294% higher than in the closed nanotubes, since in the former case the CNT interiors are also available for hydrogen physisorption through a capillary effect. The effective volume inside each CNT is 87% of the volume of the layer of hydrogen molecules physisorbed on its exterior surface. However, at 273 K and 20 atm the storage inside CNTs accounts for about 75% of the total storage. Thus, hydrogen molecules are more densely stored inside a CNT than outside it. (The behavior at 100 K is similar.) The dense storage inside CNTs as compared to their exteriors is due to the smaller short-range hydrogen-hydrogen repulsive force inside the nanotubes, as described by (Zheng et al., 2005).

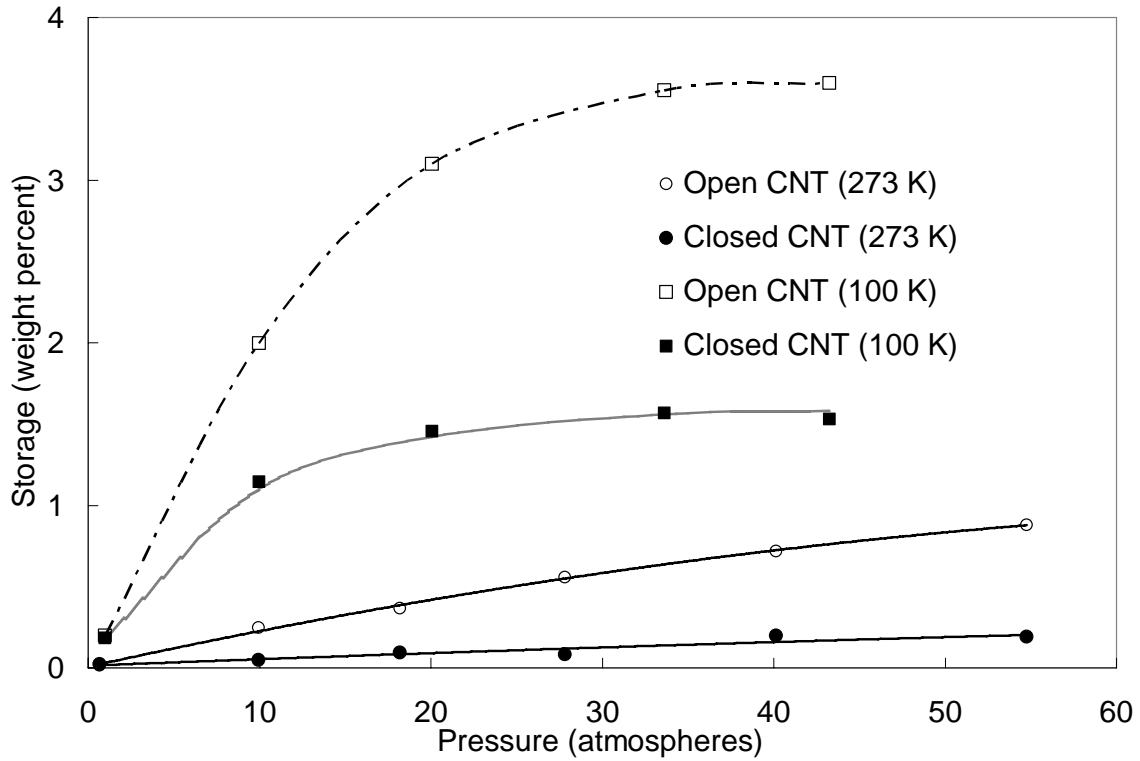


Figure 4.9: Variation of hydrogen storage with pressure in open and closed-ended carbon nanotube electrodes in the presence of Li ion interconnects.

In spite of the van der Waals forces between the hydrogen molecules and the carbon atoms of the CNTs, storage is limited by the repulsive forces between the hydrogen molecules. (Stan and Cole, 1998b) have demonstrated through theoretical calculations that there is a stronger adsorbate-adsorbate binding inside such nanotubes. This results in greater storage inside the CNTs.

Chapter 5: Carbon Nanotube Growth Mode

5.1. Introduction

A carbon deposit can be created at elevated temperatures on catalytically active transition metal nanoparticles that are placed in a reducing environment with high gas-phase carbon activity (Sacco et al., 1984), (Kock et al., 1985). The deposited carbon diffuses into the catalyst nanoparticle, nucleates within it, and emerges in the form of CNTs or CNFs. The subsequent catalyzed growth of CNTs and CNFs occurs mainly through two modes. The base growth mode arises when the metal nanoparticle catalyzing the growing carbon nanostructure remains at the bottom of the nanotube. For this type of growth the adhesive forces between the substrate and the catalyst nanoparticle are typically too large for the particle to be lifted as the CNT/CNF grows. Alternately, the catalyst nanoparticle is lifted by the growing carbon nanostructure during tip growth, and remains at the tip of the CNT/CNF after its growth ceases.

The nature of the growth mode, whether tip or base, is important for various applications. For instance, the nucleation of metal particles on the end caps of CNTs can assist in the alignment of these nanostructures in the presence of external electric or magnetic fields, thus imparting directional properties to materials in which these are embedded (Park et al., 2008), (Camponeschi et al., 2007). Such functionalized tips can also be used to attract other molecules for various applications, e.g., for functionalization with protonated amines ($-\text{NH}_3^+\text{Cl}^-$) that add positive charges to CNTs, which allows binding to negatively charged RNA molecules (Krajcik et al., 2008). Continuum scale

CNT growth models that typically assume a certain growth mode (Zhang and Smith, 2005) can also benefit from these predictions.

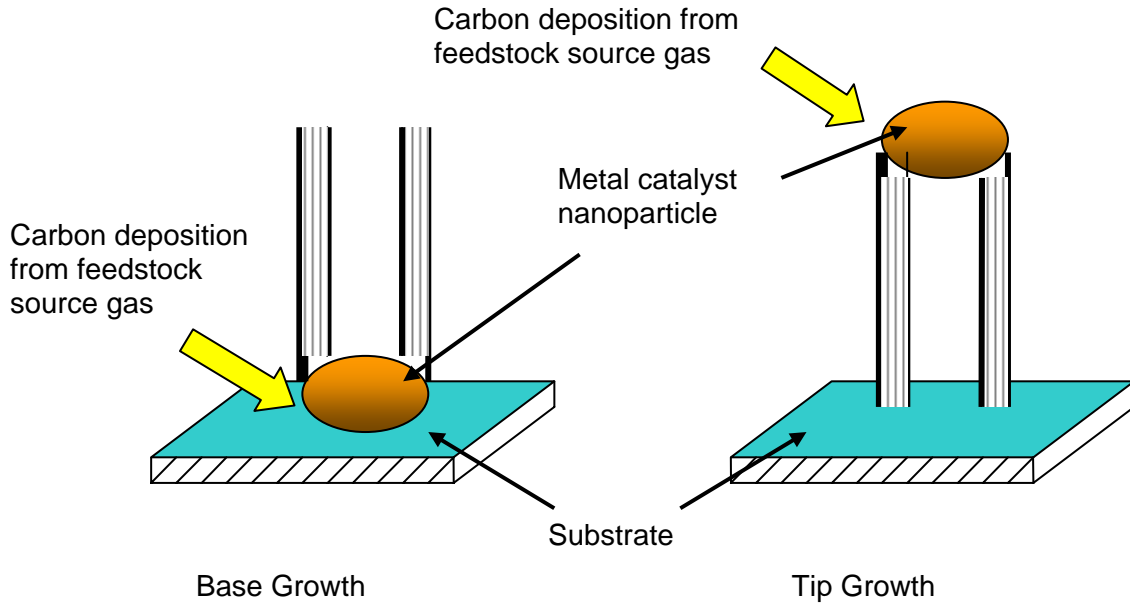


Figure 5.1: Schematic illustrating the growth modes of carbon nanotubes.

Illustrations of the two growth modes are presented in Figure 5.1. The likely growth (tip or base) mode depends on the energy gain $\Delta E_{np \rightarrow CNT}$ due to the addition of C-atoms from the carbon-metal catalyst solution to the graphene sheets forming the CNTs and CNFs. For tip growth to occur, the catalyst particle is lifted from a substrate only if the energy gain is sufficient to overcome the surface binding or interface energy between the nanoparticle and the substrate, i.e., $\Delta E_{np \rightarrow CNT} \geq \gamma R_p^2$, where γ and R_p respectively denote the surface energy per unit area and the diameter of the metal catalyst particle. Smaller energy gains lead to base growth. The prediction of the dominant growth mode for a specific condition requires that $\Delta E_{np \rightarrow CNT}$ be determined using MD

simulations. One can justify either growth mode on the predicted energy gain, an analysis that is found to be more robust than one based on characteristic time scale considerations.

The experimentally observed base growth mode by Wu *et al.* was facilitated by an Fe catalyst immersed in C₂H₄ with a ≈ 162.86 torr partial pressure and 1048 K temperature (Wu et al., 2008). The other gaseous species were H₂ (carrier gas) and Ar (inert). The experimental results of Ducati *et al.* revealed a predominance of vertically aligned CNTs grown through a tip-growth mode with Ni as catalyst and C₂H₂ as the carbon source gas at a temperature of 823 K and 1.5 torr partial pressure (Ducati et al., 2004). The simulations correspond to conditions for these two representative cases.

5.2. Methodology

The MD simulations are based on the massively parallel LAMMPS code.(Plimpton, 1995) The interaction between the carbon atoms in the metal and the nanotube are modeled using the Adaptive Intermolecular Reactive Empirical Bond Order (AIREBO) potential

$$E = \frac{1}{2} \sum_{i=1}^N \sum_{j \neq i}^N \left[E_{ij}^{REBO} + E_{ij}^{LJ} + \sum_{k \neq i, j} \sum_{l \neq i, j, k} E_{kijl}^{TORSION} \right]. \quad (5.1)$$

The E^{REBO} term has the same functional form as the hydrocarbon REBO potential (Brenner et al., 2002). The E^{LJ} term adds longer-range interactions ($2 \text{ \AA} < r < r_{cutoff}$) using a form similar to the standard LJ potential. The $E^{TORSION}$ term is an explicit four-body potential that describes various dihedral angle preferences in hydrocarbon configurations. The Ni-Ni and Fe-Fe interactions are modeled using the Embedded Atom Model (EAM) potential,

$$E_i = F_\alpha \left(\sum_{j \neq i}^N \rho_\alpha(r_{ij}) \right) + \frac{1}{2} \sum_{j \neq i}^N \phi_{\alpha\beta}(r_{ij}), \quad (5.2)$$

where F denotes the embedding energy, which is a function of the atomic electron density ρ , ϕ a pair potential interaction, and α and β the element types of atoms i and j . The manybody nature of the EAM potential is a result of the embedding energy term. Both summations in the formula are over all neighbors j of atom i within the cutoff distance r_{cutoff} . The interactions between Ar-Ar, Ar-Ni/Fe, Ar-C and Ni-C are modeled using a LJ potential, as described earlier in Eq. (2.1). The LJ interaction parameters σ_{ij} and ϵ_{ij} are obtained from the literature (Nigra et al., 2004, Turner et al., 2002) and are listed in Table 5.1 for various cases.

Interaction parameters	ϵ (eV)	σ (Å)
Ar-Ar	0.0103	3.4
Ar-Ni	0.1426	3.57
Ar-Fe	0.0516	3.7
C-Ar	0.00497	3.4
C-Ni	0.0688	3.57
C-Fe	0.02495	3.7

Table 5.1: Lennard Jones interaction parameters for Fe, Ni, C and Ar.

The simulation configuration is schematically described in Figure 5.2. The $13.75 \text{ nm} \times 2.75 \text{ nm} \times 54.8 \text{ nm}$ cuboid domain consists of a (10, 10) single-walled armchair CNT of 1.375 nm diameter, 2.74 nm length, and 2.49 Å pore size. The CNT, placed on top of a Ni or Fe nanoparticle with dissolved C atoms, is surrounded with an Ar ambient. Thus, the simulations model experimental conditions following carbon diffusion into the metal catalyst and its subsequent nucleation. The C-atom concentration in the metal is 6.67% for both cases. The system temperature is varied between 700K and 1100K, and the pressure is maintained at 760 torr (1 atm). Periodic conditions apply to the boundaries in order to eliminate wall effects so that the system is effectively infinite in all directions.

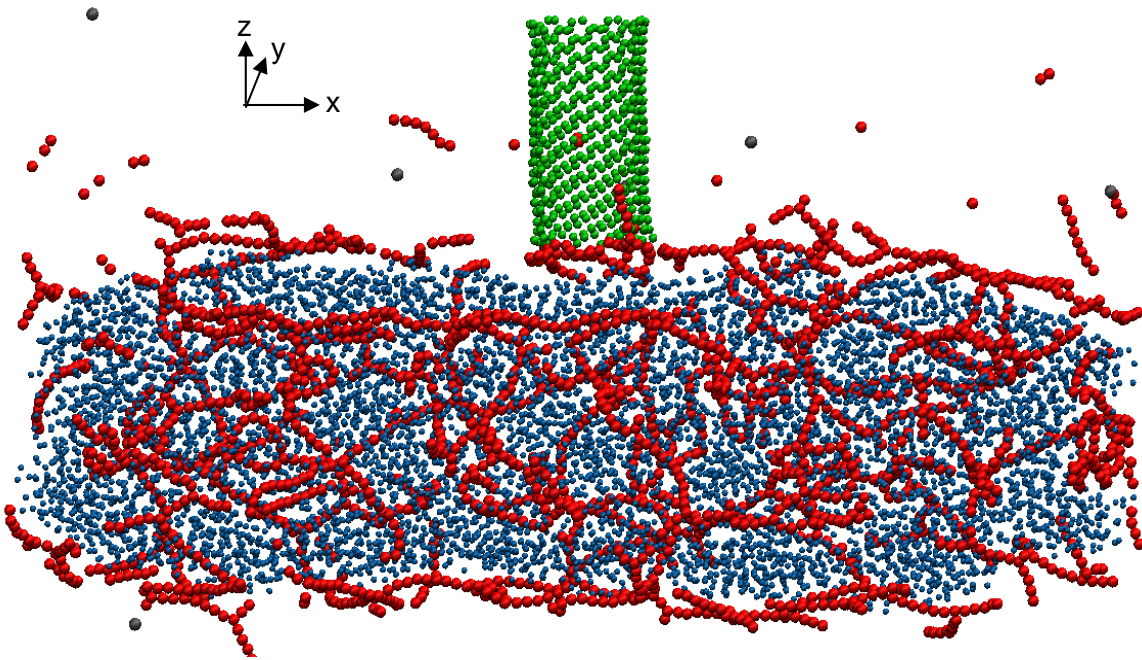


Figure 5.2: A two-dimensional orthographic view of the molecular dynamics simulation domain with the carbon nanotube (green), which is surrounded by ambient Ar (gray), growing on top of the metal catalyst particle (blue) that has dissolved carbon (red).

A typical simulation for a Fe nanoparticle consists of 6825 Fe atoms, 2748 C atoms, 44 Ar atoms and the CNT. A similar simulation for Ni consists of 8253 Ni atoms, 2275 C-atoms, 44 Ar atoms and the CNT. Initially, all molecules that are not part of the CNT form an fcc lattice that equilibrates through the simulations. A thermostat maintains constant temperature so that the molecules have an initial velocity distribution corresponding to the system temperature. A cutoff distance of 3 Å for the AIREBO and 6 Å for the LJ potential is used. Once the configuration equilibrates, the total energy of the carbon atoms that have attached to the CNT is calculated, since the difference between the initial and final energies of these atoms equal $\Delta E_{np \rightarrow CNT}$. A typical input file for LAMMPS and the data file specifying the initial configuration are provided in Appendix A.

5.3. Results and Discussion

The time evolution of the total system energy at 800K is presented in Figure 5.3. The system under consideration is the one with the Fe nanoparticle. The system energy reaches a minimum value and remains constant after 75 fs. The data is sampled between 8,500 fs and 18,500 fs, which is well beyond this equilibration time, to obtain the equilibrium energy values for the various cases. The initial energy of the carbon atoms dissolved in the catalyst particle is likewise sampled between 100 fs and 2,500 fs, and the corresponding average values are reported.

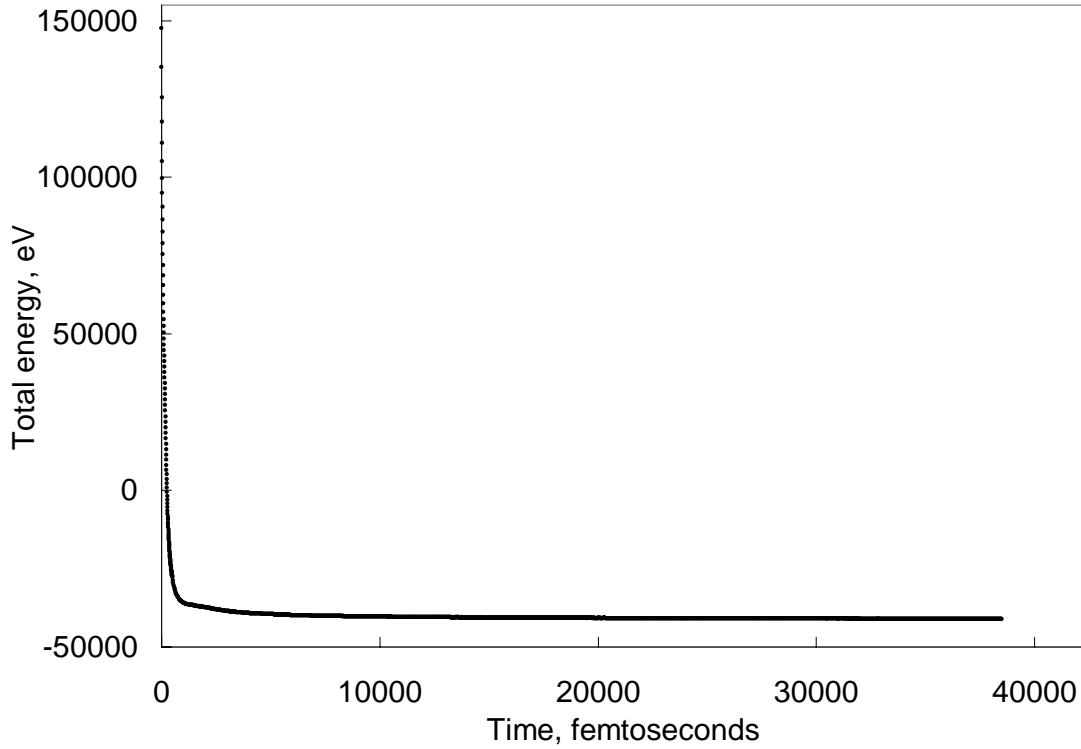


Figure 5.3: Variation of the total system energy with time.

Figure 5.4 presents the temperature dependence of $\Delta E_{np \rightarrow CNT}$ for both Fe and Ni catalysts. In the case of Fe, the magnitude of the energy change decreases with an increase in temperature between 700 and 900K, but is thereafter constant at higher temperatures. The specific surface energy for Fe $\gamma = 0.17 \text{ eV}/\text{\AA}^2$ (Vitos et al., 1998) so that the surface interaction energy for a typical 10 nm Fe catalyst particle $\gamma R_p^2 \approx 1700 \text{ eV}$. For temperatures between 700-1100K, $\Delta E_{np \rightarrow CNT} < 600 \text{ eV}$, Since $\Delta E_{np \rightarrow CNT} < \gamma R_p^2$, this indicates a base growth mode. There is a weak temperature dependence of the energy change in the case of Ni and $\Delta E_{np \rightarrow CNT} > 125 \text{ eV}$ over the entire temperature range. For Ni, $\gamma = 0.125 \text{ eV}/\text{\AA}^2$, i.e., for a typical 3 nm Ni catalyst particle, $\gamma R_p^2 \approx 113 \text{ eV}$, which is

smaller in value than $\Delta E_{np \rightarrow CNT}$. Hence, the energy change due to bond formation is large enough to induce tip growth. Table 5.2 provides representative energy values for a simulation at 700K. It demonstrates that while $\Delta E_{np \rightarrow CNT} > \gamma R_p^2$ for Ni, the converse is true for Fe catalyst.

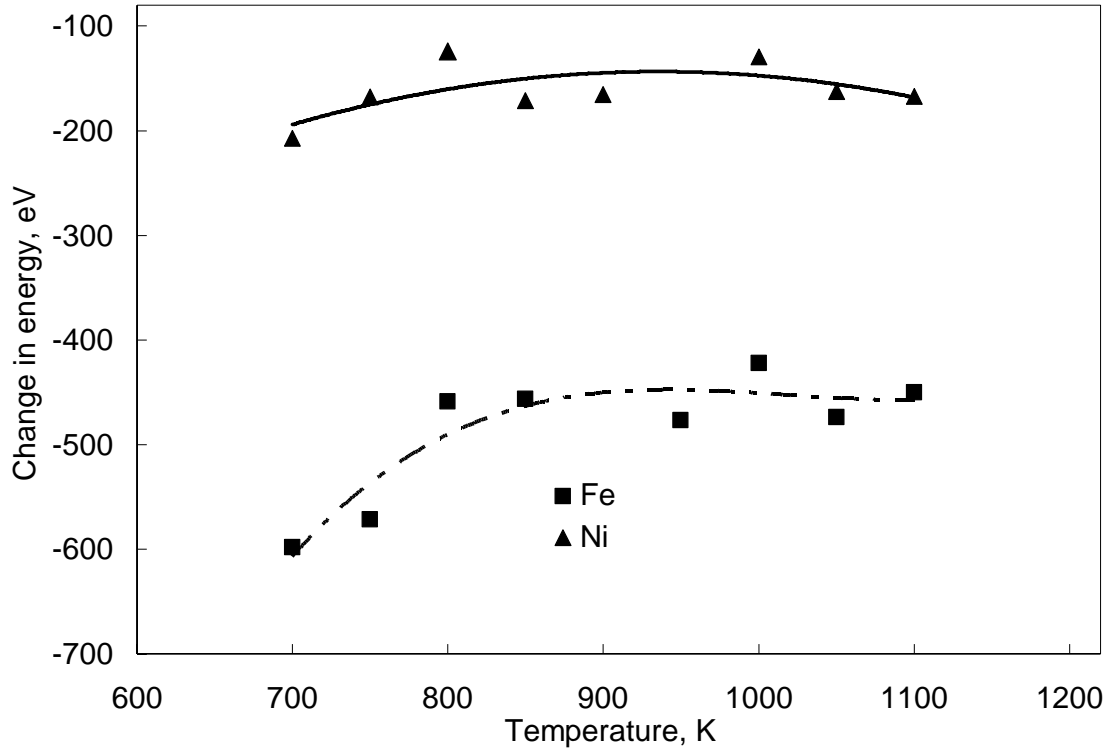


Figure 5.4: Variation of the energy change with respect to temperature for Ni and Fe.

Catalyst	ΔE (eV)	γ (eV/Å²)	γR_p^2 (eV)	Growth Type
Fe	598.46	0.170	1700.0	Base
Ni	207.43	0.125	112.5	Tip

Table 5.2: A chart showing representative energy values for a temperature of 700 K.

Chapter 6: Nanoscale Heat Transfer at Solid-Fluid Interfaces

6.1. Introduction

Recent interest in nanoscale cooling has led to increasing research on thermal transport at the nanoscale. This in turn provides key inputs into the mechanisms involved in heat conduction. As particle size is decreased the surface area to volume ratio increases, thereby making the heat transfer at the solid-fluid (nanoparticle-fluid) interface more important (Eastman et al., 2004). The physics of interfacial heat transfer, especially for simple solid-fluid interfaces, is thus an important area of concern for researchers, and the complete understanding of the temperature jump at interfaces due to thermal resistance (Kapitza resistance) for different combination of materials and at different temperatures is an area waiting to be explored. The temporal variation of Kapitza length is also an interesting problem to be aware of.

One of the exciting areas of research that is drawing huge attention is multi-scale analysis and the attempt to construct the necessary bridge between the same physical phenomena occurring at two different scales; heat transfer at interfaces in the continuum level and at the nanoscale need to shake hands (Xiao and Belytschko, 2004), and the ability to suitably incorporate the boundary conditions for such problems remains a hurdle to be overcome (Xu and Li, 2007).

In the nanoscale, heat transfer at solid-fluid interfaces involves a thermal slip that characterizes the resistance at the interface. It is very important to measure the slip values in order to fully understand this phenomenon. It is extremely difficult to design experiments at the nanoscale. Hence, molecular simulations are used to model heat

transfer at the nanoscale. The results from these simulations can provide useful information. The literature in this field is scanty and only characterizes the resistance at steady state. However, keeping in mind the inherent transient nature of the phenomena, it is important to characterize the time evolution of the temperature profile at the interface. This Chapter presents results related to heat transfer at solid-fluid interfaces. Nanoscale thermal transport has been simulated at a solid-fluid interface by placing cooler liquid-vapor Ar mixtures adjacent to warmer Fe walls. The equilibration of the system towards a uniform overall temperature is investigated using NEMD simulations from which the heat flux is also determined explicitly.

6.2. Methodology

Atomistic simulations, such as those based on MD which is a fundamental technique rooted in the principles of classical mechanics (Poulikakos et al., 2003), can help explain interfacial effects (Murad and Puri, 2007b, Murad and Puri, 2007a) during nanoscale thermal transport (Heyes and March, 1996). Examples of such MD studies (Xue et al., 2003) include investigations of heat transfer between simple solid-fluid interfaces (Wang et al., 2007, Murad and Puri, 2008) and of the bonding between liquid and solid atoms (Xue et al., 2004). These simulations have been limited to steady state investigations of nanoscale thermal transport across interfaces (Chaudhuri et al., 2007b, Khare et al., 2006, Wang et al., 2007, Maruyama, 1999, Chaudhuri et al., 2007a). Another limitation is that the heat flux is not typically determined explicitly in these simulations, but rather *a posteriori* using the Fourier heat conduction law (Maruyama, 1999). In order to address these two issues, a NEMD approach is employed to investigate

the transient thermal transport across a nanoscale interface in which the values of \dot{q} are explicitly determined.

Interaction Parameters	ϵ (eV)	σ (Å)
Ar-Ar	0.0103	3.4
Ar-Fe	0.0516	3.7

Table 6.1: Lennard Jones interaction parameters for Fe and Ar.

The Fe-Ar and Ar-Ar interactions have been modeled using the LJ potential as described in Eq. (2.1). The values of the LJ interaction parameters σ_{ij} and ϵ_{ij} are listed in Table 6.1 (Lummen and Kraska, 2004).

Molecular dynamics simulations have also been able to reproduce the temperature discontinuities across solid-fluid interfaces by modeling the solid atoms with a harmonic potential function (Ohara and Suzuki, 2000, Maruyama, 1999). While this is a better representation than the LJ model which tethers solid atoms to their respective equilibrium positions, we employ the even more realistic EAM potential which incorporates many-atom interactions (Mendelev et al., 2003, Daw et al., 1993) that are otherwise neglected in a pair-potential scheme (Johnson, 1989). It has been demonstrated in the literature that EAM potentials are very accurate in modeling properties involving metal (such as Fe) surfaces (Daw and Baskes, 1984). The EAM model has been explained in details in Eq. (5.2) in Chapter 5. The relevant parameters for the EAM model are obtained from the literature (Mendelev et al., 2003).

The simulation configuration is described in Figure 6.1. The $3 \text{ nm} \times 3 \text{ nm} \times 58 \text{ nm}$ cuboid contains two $3 \text{ nm} \times 3 \text{ nm} \times 1 \text{ nm}$ Fe blocks that restrain a liquid-vapor Ar

mixture (with an initial 33% vapor volume fraction) between them. These solid Fe blocks extend from 14-15 nm and 43-44 nm along the x-direction. The Ar liquid-vapor mixture consists of 3402 atoms that initially form an fcc lattice which equilibrates through the simulations. Periodic boundary conditions apply in all directions to eliminate wall effects so that the system is essentially infinite. The cut-off distance for the LJ interactions between both the metal-fluid and the fluid-fluid atoms is 10 Å, or roughly 3 atomic diameters. Linear momentum is conserved throughout the entire simulation. In the simulation, the linear momentum is rescaled to the initial value every 10 timesteps.

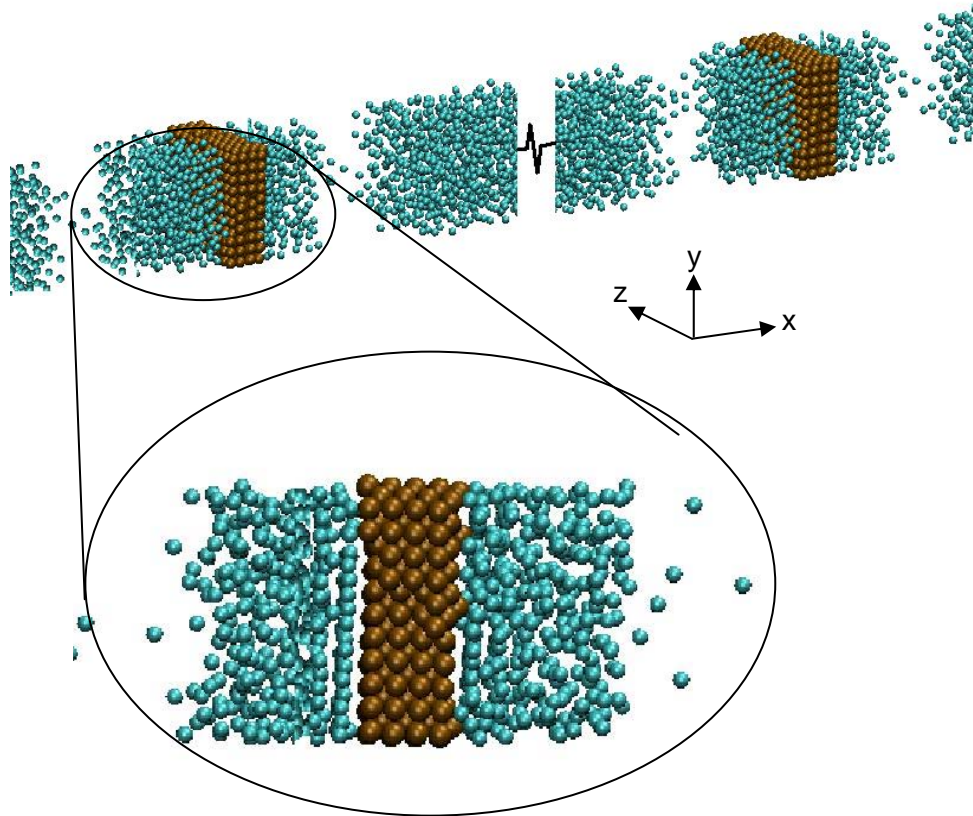


Figure 6.1: A 3-dimensional view of the molecular dynamics simulation domain in which Ar (cyan) fills a space of 28 nm between two 1 nm thick blocks of solid Fe. Fluid atoms on both sides of the walls indicate periodicity. A close-up orthographic view shows the observed Ar-atom layering at the solid-fluid interface.

The system is initialized at a temperature of 100K. During the first 300 picoseconds (ps), a velocity-rescaling temperature control is applied for all atoms. This ensures an initial equilibrium state for which the entire system is at uniform temperature. Subsequently, for the next 700 ps, the temperature of the solid atoms is controlled while fluid atoms are allowed to behave freely and equilibrate. At 1000 ps, the Fe blocks are provided with a step increase to a higher temperature (by increasing the kinetic energy of the atoms), which is thereafter maintained with constant velocity rescaling for the remainder of the simulation. The simulations are based on the massively parallel LAMMPS code (Steve, 1995, Plimpton, 1993) and are advanced through successive 0.1 fs time steps. A typical input file for LAMMPS and the data file specifying the initial configuration are provided in Appendix A.

6.3. Results and Discussion

Figure 6.2 presents the averaged number density distribution of the Fe and Ar atoms when both Fe blocks are maintained at 120 K. The figure shows that the fluid atoms adjacent to the solid walls migrate closer towards them due to the Fe-Ar intermolecular interactions to form discrete interfacial layers in agreement with previous investigations (Murad and Puri, 2008, Xue et al., 2004, Xue et al., 2003, Ohara and Suzuki, 2000, Maruyama, 1999).

The consequent higher Ar atom density at the interface causes a local increase in the interfacial pressure so that the packed fluid layers are quasi solid-like. Since the fluid is initially a liquid-vapor mixture, this inhomogeneous density distribution occurs due to phase segregation. Ar atoms that are further removed from the walls do not experience the wall-vapor intermolecular attraction and thus remain homogeneously distributed. In

contrast, the migration of the fluid Ar atoms towards the walls to form the quasi-crystalline layers from proximal vapor-containing regions that are a few atomic diameters removed from the interfaces creates local vacancies. Essentially, Ar atoms closest to the walls exhibit a denser and more packed quasi-crystalline behavior, those further removed from the walls behave as fluid, with vacancies separating these two regions.

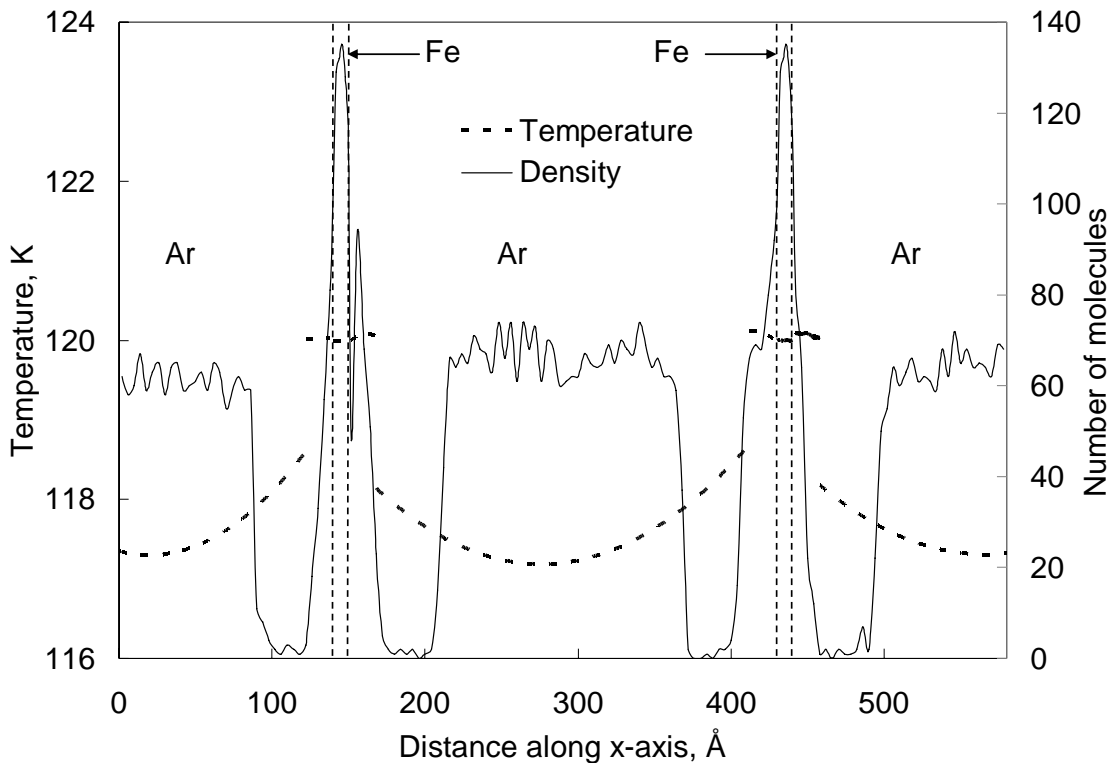


Figure 6.2: The temperature (dotted line) and density (solid line) distributions across the x-wise direction after the system nears its steady state. The solid Fe walls are located between 14-15 nm and 43-44 nm. The fluid domain is divided into several 4 Å thick slabs along the x-direction for the purpose of spatial characterization, and the density and temperature distributions within them are sampled at uniform time intervals.

Figure 6.2 also presents the average temperature (based on a local equilibrium approximation) of each 4 Å thick slab in the domain. The temperature of each slab is calculated from the velocities of the atoms in the slab using the equi-partition assumption, i.e. $T = mv_{rms}^2 / k_b$. Here, m is the mass of the Ar atom, k_b is the Boltzmann constant, and v_{rms} is the root mean square velocity of the atoms in the slab. The Ar atom layers adjacent to each wall have a temperature nearly equal to that of the solid. This is followed by a sharp temperature drop in the fluid extending from approximately four molecular layers away from each wall (Murad and Puri, 2008, Freund, 2005). The Ar atoms in the four molecule thick interfacial regions show little tendency towards significant translational motion since, being attracted to the Fe atoms, they are held relatively immobile. These quasi-crystalline Ar layers have a higher effective thermal conductivity than atoms in the corresponding fluid phase (Freund, 2005). In contrast to fluid behavior at the continuum scale, a significant temperature discontinuity occurs in the vacancies that follow the interfacial Ar atom layers, since energy transfer through these sparsely populated regions is hindered.

Figure 6.3 presents the temporal evolution of the characteristic fluid temperature, which is averaged over all slabs, as the simulation proceeds from its initial thermodynamic nonequilibrium state to a steady state. An analogous average temperature can also be obtained from the analytical solution of the continuum Fourier heat equation $\partial\theta / \partial\tau = (\partial^2\theta / \partial X^2)$, where θ denotes a dimensionless temperature $(T(x,t)-T_w)/(T_i- T_w)$, τ a dimensionless time $\alpha t / L^2$ ($\alpha = 1.12 \times 10^{-7}$ m²/s denotes the bulk Ar thermal diffusivity at the initial system temperature of 100 K, L the length of the domain in x-direction), X a dimensionless length x/L . The boundary conditions correspond to fixed

wall temperatures of T_w . The solution follows the

expression $\theta(X, \tau) = \sum_{n=1}^{\infty} \frac{2}{n\pi} (1 - \cos(n\pi)) \sin(n\pi X) e^{-n^2\pi^2\tau}$. The geometry along with

initial and boundary conditions for this solution are shown in Figure 6.4.

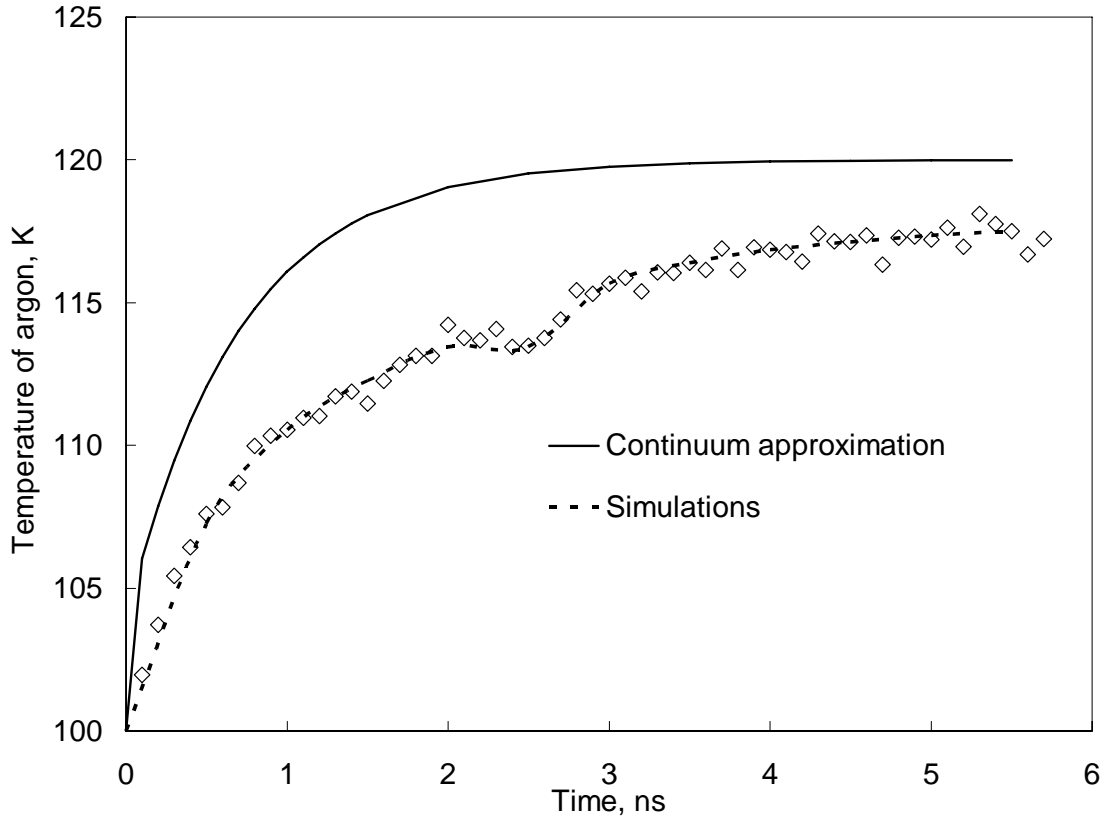


Figure 6.3: Temporal evolution of the fluid temperature obtained explicitly from the simulations and empirically from an analytical solution to Fourier’s law of heat conduction (assuming homogenous and constant properties).

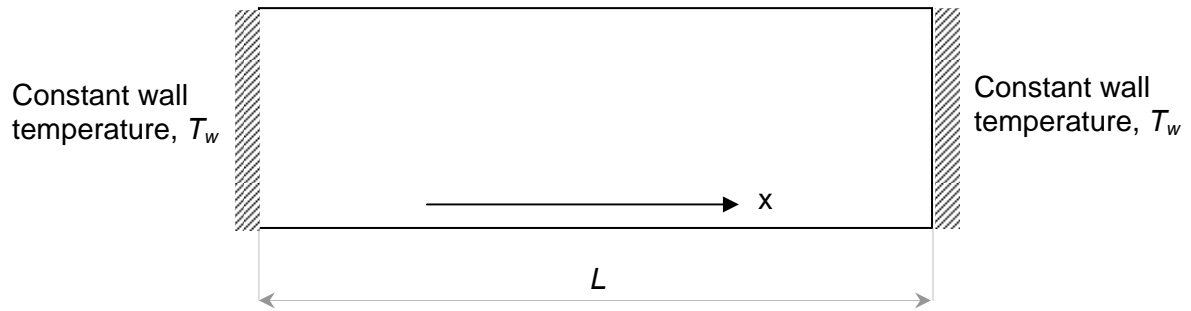


Figure 6.4: Schematic of the system solved using Fourier's Equation.

The response of the MD simulations to thermodynamic non-equilibrium differs from that of the analytical continuum solution. The simulation provides evidence of nonequilibrium effects even after 5000 ps whereas the analytical solution reaches steady state by 3000 ps. Moreover, Figure 6.3 also shows that the bulk temperature temporarily stabilizes after ≈ 2500 ps. This occurs due to a temporary departure from the quasi-crystalline interfacial layering of Ar atoms as the system equilibrates. This reordering impedes heat transfer for ≈ 200 -400 ps so that the fluid temperature remains virtually constant. Thermal transport resumes following the molecular rearrangement, but at a slower rate. In contrast, the continuum analysis assumes homogenous system properties for all times, although the simulation results presented in Figure 6.2 contain evidence to the contrary. The source for the discrepancy between the continuum analytical solution and the MD simulations is attributed to the heterogeneous system characteristics due to the interfacial layering of Ar atoms. This provides emphasis for the assertion that for values of the heat flux to be accurate, these must be determined explicitly from nanoscale simulations rather than implicitly using continuum relations.

This issue is investigated further. It is typical to determine the heat flux across nanoscale interfacial layers using a bulk thermal conductivity, i.e., by essentially making

a quasi-continuum approximation. Instead the net energy flux \dot{q}_{sl} is calculated from the solid molecules s to the fluid molecules l , i.e., $\dot{q}_{sf} = (\dot{E}_{fs} - \dot{E}_{sf})/2$, where \dot{E}_{fs} and \dot{E}_{sf} denote the energy fluxes from a fluid to solid and solid to fluid molecules, respectively (Ohara, 1999). Here, the intermolecular energy transfer \dot{E}_{fs} is computed from the scalar product of the relative force \vec{f}_{fs} and the velocity \vec{v}_{fs} . With this approach, the total thermal energy transferred from a high temperature wall to the low temperature fluid adjacent to it is $\dot{q} = \sum_s \sum_l \dot{q}_{sf}$, which can also be used to determine R_k (Eq. 2.2) explicitly from the simulation. Further, assuming for a specified mass $m=N_{Ar}M_{Ar}$ that the approximate energy flux $\dot{q}_{ap} = (mc/A)(dT_{av}/dt)$, where N_{Ar} and M_{Ar} denote the number of Ar atoms in the system and their molecular mass, A the interfacial area through which heat flows, c the constant volume specific heat of Ar, and T_{av} the average fluid temperature, an expression is obtained for the approximate Kapitza resistance $R_{k,ap} = (A/mc)\Delta T/(dT_{av}/dt)$. Figure 6.5 presents the temporal variation of R_k and $R_{k,ap}$ when the temporal values of ΔT are identical. Again, there is almost an order of magnitude difference in the values of these two interfacial resistances. The thermal resistance values obtained from the molecular simulations are consistently higher in magnitude when compared to the values obtained using the continuum approximation. The presence of the temperature jump at the interface restricts the thermal transport causing an increase of the thermal resistance at the interface. Such discontinuity in the temperature profile is neglected in the corresponding continuum model and hence it provides a lower value of the thermal resistance. Their behaviors are similar although their rates of increases are different. The interfacial thermal resistance increases over time.

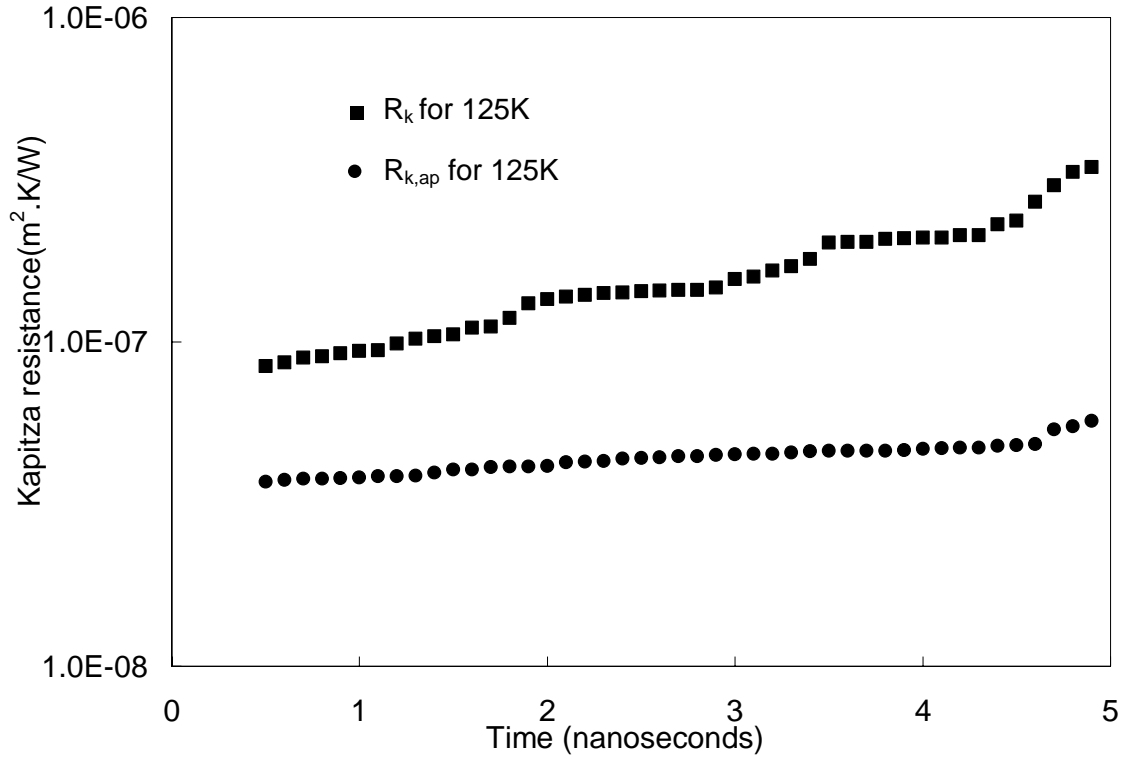


Figure 6.5: Temporal evolution of the interfacial thermal resistances for wall temperature of 125 K (based on heat fluxes calculated using a first principles and a quasi-continuum approach). The interfacial temperature drop is calculated as a time average over 100 ps.

The influence of wall temperature on the thermal resistance is examined next. For each simulated case, the value of ΔT is averaged over the period from 2000-4000 ps, and the heat flux $\dot{q}_{av} = (1/2000) \sum_{i=2000ps}^{4000ps} \dot{q}_i$ to determine the average interfacial resistance $R_{k,av}$, which is presented in Figure 6.6 with respect to increasing wall temperature T_w .

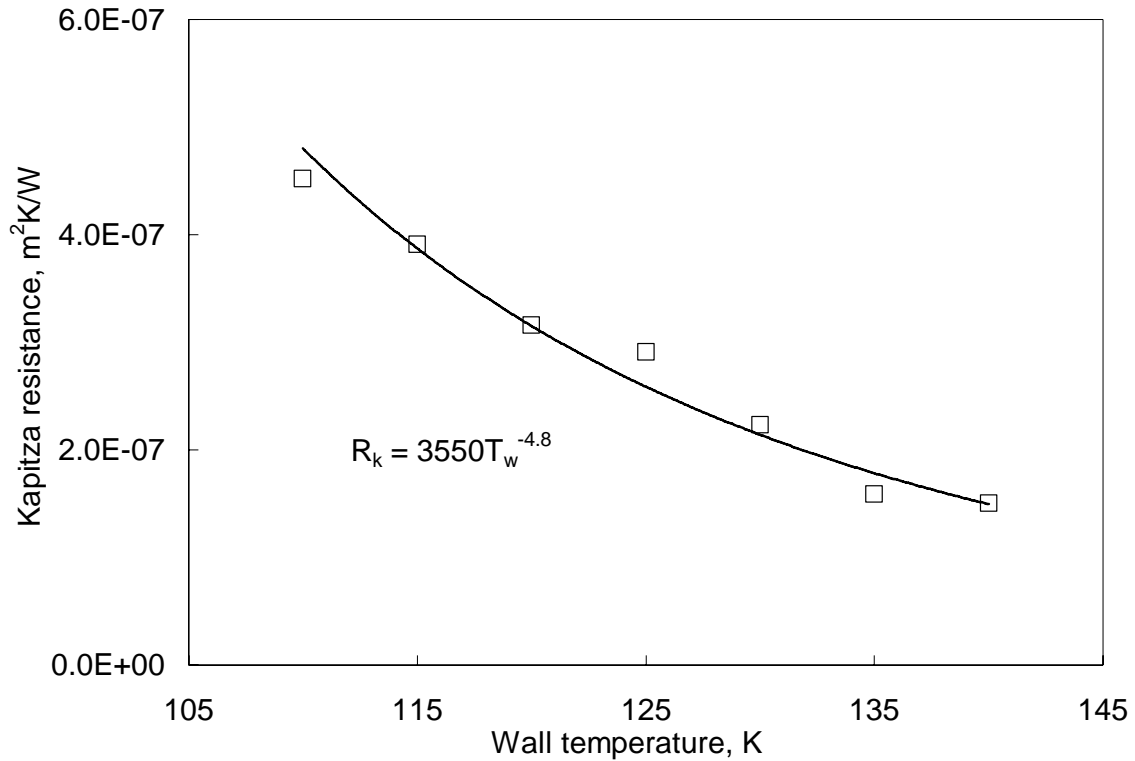


Figure 6.6: Change in the Kapitza resistance (based on heat fluxes calculated using a first principles approach) with respect to varying wall temperature. The fluxes and temperature drops are averaged over 2000-4000 ps.

As T_w increases, the pressure within the fluid and hence on the quasi-crystalline layers rises. Consequently, the interfacial molecular layers become more closely packed and the local intermolecular interactions are enhanced. Consequently, thermal transport through these layers also increases, leading to a decrease in the interfacial thermal resistance according to the relation $R_{k,av} \propto T_w^{-4.8}$.

Chapter 7: Conclusions

7.1. Ion Adsorption in Carbon Nanotubes

The results presented in this dissertation demonstrate that when spatially or temporally alternate charge patterns are applied to CNTs, ion intake into them is minimal. While ion flow through charged nanochannels has been previously investigated (Qiao and Aluru, 2005, Kang et al., 2004), the role of alternating spatial or temporal charge patterns to accomplish the controlled intake of either ions or polar solvents such as water has not been described. The interesting consequence of the results presented here is that nanotubes can be used for the preferential intake of only water molecules. They can thus be used as water-purifying devices (or conversely as ion concentrators for the solution external to CNTs). These CNTs can also be used as water or ion encapsulation devices, depending on the applied charge pattern.

7.2. Hydrogen Storage in Carbon Nanotubes

The results indicate that while alkali metal nanowafer interconnects increase storage, albeit by a relatively small amount, the inclusion of unassociated transition metal ions such as Pd and Ti do not. Carbon nanotube electrodes store only slightly higher amounts of hydrogen in the presence of Li ions at pressures lower than 25 atm. Results from the simulations also show that nanotubes with open ends store significantly more hydrogen than those with closed ends. In general, the simulated data imply that CNTs do not store more than 1% hydrogen by weight at 273 K. Thus a high pressure and low temperature operating condition is necessary for reasonable storage. The dependence of storage on the ambient temperature and pressure is influenced by the interconnect

material. In presence of an interconnect made of Li ions, increasing the ambient pressure above 40 atm and decreasing the temperature below 165 K leads to the largest incremental enhancement in hydrogen storage. However, in presence of a C atom interconnect pressures greater than 25 atm and temperatures less than 180 K produce similar results.

7.3. Carbon Nanotube Growth Mode

The growth modes of CNTs using atomistic MD simulations are investigated and the results are qualitatively validated against experimental evidence. The MD results suggest different growth modes for Ni and Fe catalysts. While the magnitude of energy gain for a wide range of temperatures typically encountered in catalyzed CNT growth is smaller than the surface interaction energy for Fe, the converse is true for Ni. The MD simulation results suggest that Ni catalyst nanoparticles are conducive for tip growth while Fe nanoparticles promote base growth. Use of Ni produces a local minimum energy at approximately 900K while for Fe-catalyzed growth, the energy gain decreases to a constant minimum value at temperatures exceeding 900K. A phenomenological time scale is insufficient to definitively characterize the nature of the growth mode. Thus, it is imperative to quantify the energy gain due to the addition of carbon atoms to a CNT based on more fundamental considerations such as MD simulations.

7.4. Nanoscale Heat Transfer at Solid-Fluid Interfaces

It is concluded that unsteady nanoscale thermal transport differs from that at the continuum scale. It takes longer for a nanoscale system to respond to an imposed temperature difference (applied through velocity rescaling) than predicted by an analytical continuum solution. The steady state temperature distribution between the

quasi-crystalline fluid interfacial layers adjacent to a solid wall and the rarified fluid–side vacancy-containing region following these layers exhibits a discontinuity due to phase segregation in the fluid. As the average temperature difference between the warmer interface and cooler fluid equilibrates over time, the heat flux also decreases. Overall, the interfacial thermal resistance decreases with increasing wall temperatures as $R_{k,av} \propto T_w^{-4.8}$.

BIBLIOGRAPHY

- Ahn, C.C., Ye, Y., Ratnakumar, B.V., Witham, C., Bowman, R.C. & Fultz, B. (1998). Hydrogen desorption and adsorption measurements on graphite nanofibers. *Applied Physics Letters*, Vol. 73, No. 23, pp. 3378-3380.
- Ajayan, P.M., Ebbesen, T.W., Ichihashi, T., Iijima, S., Tanigaki, K. & Hiura, H. (1993). Opening Carbon Nanotubes With Oxygen And Implications For Filling. *Nature*, Vol. 362, No. 6420, pp. 522-525.
- Akita, S., Nakayama, Y., Mizooka, S., Takano, Y., Okawa, T., Miyatake, Y., Yamanaka, S., Tsuji, M. & Nosaka, T. (2001). Nanotweezers consisting of carbon nanotubes operating in an atomic force microscope. *Applied Physics Letters*, Vol. 79, No. 11, pp. 1691-1693.
- Allen, M.P. (1987). *Computer simulation of liquids*, Oxford [England] : New York :: Clarendon Press ; Oxford University Press.
- Angadi, M.A., Watanabe, T., Bodapati, A., Xiao, X.C., Auciello, O., Carlisle, J.A., Eastman, J.A., Keblinski, P., Schelling, P.K. & Phillpot, S.R. (2006). Thermal transport and grain boundary conductance in ultrananocrystalline diamond thin films. *Journal of Applied Physics*, Vol. 99, No. 11, pp.114301(1-6).
- Arista, N.R. (2001). Interaction of swift ions with surface modes in microcapillaries and nanotubes. *Nuclear Instruments & Methods in Physics Research Section B-Beam Interactions with Materials and Atoms*, Vol. 182, pp. 109-115.
- Awasthi, K., Kamalakaran, R., Singh, A.K. & Srivastava, O.N. (2002). Ball-milled carbon and hydrogen storage. *International Journal of Hydrogen Energy*, Vol. 27, No. 4, pp. 425-432.

- Baker, R.T.K. (1989). Catalytic growth of carbon filaments. *Carbon*, Vol. 27, No. 3, pp. 315-323.
- Banerjee, S., Murad, S. & Puri, I.K. (2007). Preferential ion and water intake using charged carbon nanotubes. *Chemical Physics Letters*, Vol. 434, No. 4-6, pp. 292-296.
- Barrat, J.L. & Chiaruttini, F. (2003). Kapitza resistance at the liquid-solid interface. *Molecular Physics*, Vol. 101, No. 11, pp. 1605-1610.
- Becher, M., Haluska, M., Hirscher, M., Quintel, A., Skakalova, V., Dettlaff-Weglikovska, U., Chen, X., Hulman, M., Choi, Y., Roth, S., Meregalli, V., Parrinello, M., Strobel, R., Jorissen, L., Kappes, M.M., Fink, J., Zuttel, A., Stepanek, I. & Bernierg, P. (2003). Hydrogen storage in carbon nanotubes. *Comptes Rendus Physique*, Vol. 4, No. 9, pp. 1055-1062.
- Bell, T.W. (1998). Carriers and channels: current progress and future prospects. *Current Opinion in Chemical Biology*, Vol. 2, No. 6, pp. 711-716.
- Berendsen, H.J.C., Postma, J.P.M. & von Gunsteren, W.F. (1981). Intermolecular Forces. Pullman, B. (Ed.). Dordrecht: Reidel.
- Bernholc, J., Roland, C. & Yakobson, B.I. (1997). Nanotubes. *Current Opinion in Solid State & Materials Science*, Vol. 2, No. 6, pp. 706-715.
- Bodapati, A., Schelling, P.K., Phillpot, S.R. & Koblinski, P. (2006). Vibrations and thermal transport in nanocrystalline silicon. *Physical Review B*, Vol. 74, No. 24, pp. 245207(1-11).
- Brenner, D.W., Shenderova, O.A., Harrison, J.A., Stuart, S.J., Ni, B. & Sinnott, S.B. (2002). A second-generation reactive empirical bond order (REBO) potential

- energy expression for hydrocarbons. *Journal of Physics: Condensed Matter*, Vol. 14, No. 4, pp. 783-802.
- Cabria, I., Lopez, M.J. & Alonso, J.A. (2005). Enhancement of hydrogen physisorption on graphene and carbon nanotubes by Li doping. *Journal of Chemical Physics*, Vol. 123, No. 20, 204721(1-9).
- Cabria, I., Lopez, M.J. & Alonso, J.A. (2006). Density functional study of molecular hydrogen coverage on carbon nanotubes. *Computational Materials Science*, Vol. 35, No. 3, pp. 238-242.
- Cahill, D.G., Ford, W.K., Goodson, K.E., Mahan, G.D., Majumdar, A., Maris, H.J., Merlin, R. & Phillpot, S.R. (2003). Nanoscale thermal transport. *Journal of Applied Physics*, Vol. 93, No. 2, pp. 793-818.
- Callejas, M.A., Anson, A., Benito, A.M., Maser, W., Fierro, J.L.G., Sanjuan, M.L. & Martinez, M.T. (2004). Enhanced hydrogen adsorption on single-wall carbon nanotubes by sample reduction. *Materials Science and Engineering B-Solid State Materials for Advanced Technology*, Vol. 108, No. 1-2, pp. 120-123.
- Camponeschi, E., Vance, R., Al-Haik, M., Garmestani, H. & Tannenbaum, R. (2007). Properties of carbon nanotube-polymer composites aligned in a magnetic field. *Carbon*, Vol. 45, No. 10, pp. 2037-2046.
- Cao, A.Y., Zhu, H.W., Zhang, X.F., Li, X.S., Ruan, D.B., Xu, C.L., Wei, B.Q., Liang, J. & Wu, D.H. (2001). Hydrogen storage of dense-aligned carbon nanotubes. *Chemical Physics Letters*, Vol. 342, No. 5-6, pp. 510-514.

- Chambers, A., Park, C., Baker, R.T.K. & Rodriguez, N.M. (1998). Hydrogen storage in graphite nanofibers. *Journal of Physical Chemistry B*, Vol. 102, No. 22, pp. 4253-4256.
- Chandrasekhar, J., Spellmeyer, D.C. & Jorgensen, W.L. (1984). Energy component analysis for dilute aqueous solutions of lithium(1+), sodium(1+), fluoride(1-), and chloride(1-) ions. *J. Am. Chem. Soc.*, Vol. 106, No. 4, pp. 903-910.
- Chaudhuri, D., Chaudhuri, A. & Sengupta, S. (2007a). Heat conduction through a trapped solid: the effect of structural changes on the thermal conductance. *Journal of Physics-Condensed Matter*, Vol. 19, No. 15, pp. 152201
- Che, G.L., Lakshmi, B.B., Martin, C.R. & Fisher, E.R. (1999). Metal-nanocluster-filled carbon nanotubes: Catalytic properties and possible applications in electrochemical energy storage and production. *Langmuir*, Vol. 15, No. 3, pp. 750-758.
- Chen, G. (2000). Particularities of Heat Conduction in Nanostructures. *Journal of Nanoparticle Research*, Vol. 2, No. 2, pp. 199-204.
- Chen, L.X., Guan, Y.F., Ma, J.P., Luo, G.A. & Liu, K.H. (2005). Application of a high-pressure electro-osmotic pump using nanometer silica in capillary liquid chromatography. *Journal of Chromatography A*, Vol. 1064, No. 1, pp. 19-24.
- Chen, P., Wu, X., Lin, J. & Tan, K.L. (1999). High H₂ uptake by alkali-doped carbon nanotubes under ambient pressure and moderate temperatures. *Science*, Vol. 285, No. 5424, pp. 91-93.

- Chen, Q.L., Xue, K.H., Shen, W., Tao, F.F., Yin, S.Y. & Xu, W. (2004a). Fabrication and electrochemical properties of carbon nanotube array electrode for supercapacitors. *Electrochimica Acta*, Vol. 49, No. 24, pp. 4157-4161.
- Chen, X., Zhang, Y., Gao, X.P., Pan, G.L., Jiang, X.Y., Qu, J.Q., Wu, F., Yan, J. & Song, D.Y. (2004b). Electrochemical hydrogen storage of carbon nanotubes and carbon nanofibers. *International Journal of Hydrogen Energy*, Vol. 29, No. 7, pp. 743-748.
- Chiritescu, C., Cahill, D.G., Nguyen, N., Johnson, D., Bodapati, A., Keblinski, P. & Zschack, P. (2007). Ultralow thermal conductivity in disordered, layered WSe₂ crystals. *Science*, Vol. 315, No. 5810, pp. 351-353.
- Ci, L.J., Zhu, H.W., Wei, B.Q., Xu, C.L. & Wu, D.H. (2003). Annealing amorphous carbon nanotubes for their application in hydrogen storage. *Applied Surface Science*, Vol. 205, No. 1-4, pp. 39-43.
- Collins, P.G., Bradley, K., Ishigami, M. & Zettl, A. (2000). Extreme oxygen sensitivity of electronic properties of carbon nanotubes. *Science*, Vol. 287, No. 5459, pp. 1801-1804.
- Dai, K., Shi, L.Y., Fang, J.H., Zhang, D.S. & Yu, B.K. (2005). NaCl adsorption in multi-walled carbon nanotubes. *Materials Letters*, Vol. 59, No. 16, pp. 1989-1992.
- Darabi, J. (2002). Micro- and nanoscale heat transfer: Challenges and opportunities. *Heat Transfer Engineering*, Vol. 23, No. 2, pp. 1-2.
- Darkrim, F. & Levesque, D. (1998). Monte Carlo simulations of hydrogen adsorption in single-walled carbon nanotubes. *Journal of Chemical Physics*, Vol. 109, No. 12, pp. 4981-4984.

- Darkrim, F. & Levesque, D. (2000). High adsorptive property of opened carbon nanotubes at 77 K. *Journal of Physical Chemistry B*, Vol. 104, No. 29, pp. 6773-6776.
- Datta, A., Gangopadhyay, S., Temkin, H., Pu, Q.S. & Liu, S.R. (2006). Nanofluidic channels by anodic bonding of amorphous silicon to glass to study ion-accumulation and ion-depletion effect. *Talanta*, Vol. 68, No. 3, pp. 659-665.
- Daw, M.S. & Baskes, M.I. (1984). Embedded-atom method: Derivation and application to impurities, surfaces, and other defects in metals. *Physical Review B*, Vol. 29, No. 12, pp. 6443.
- Daw, M.S., Foiles, S.M. & Baskes, M.I. (1993). The embedded-atom method: a review of theory and applications. *Materials Science Reports*, Vol. 9, No. 7-8, pp. 251-310.
- Dillon, A.C., Gennet, T., Alleman, J.L., Jones, K.M., Parilla, P.A. & Heben, M.J. (2000). In *Proceedings of the 2000 Hydrogen Program Review*.
- Dillon, A.C., Jones, K.M., Bekkedahl, T.A., Kiang, C.H., Bethune, D.S. & Heben, M.J. (1997). Storage of hydrogen in single-walled carbon nanotubes. *Nature*, Vol. 386, No. 6623, pp. 377-379.
- Dodziuk, H. & Dolgonos, G. (2002). Molecular modeling study of hydrogen storage in carbon nanotubes. *Chemical Physics Letters*, Vol. 356, No. 1-2, pp. 79-83.
- Duax, W.L., Pletnev, V. & Burkhart, B.A. (2003). Mechanism of ion transport and gating in gramicidin nanotubes. *Journal of Molecular Structure*, Vol. 647, No. 1-3, pp. 97-111.
- Ducati, C., Alexandrou, I., Chhowalla, M., Robertson, J. & Amaratunga, G.A.J. (2004). The role of the catalytic particle in the growth of carbon nanotubes by plasma

- enhanced chemical vapor deposition. *Journal of Applied Physics*, Vol. 95, No. 11, pp. 6387-6391.
- Duren, T., Keil, F.J. & Seaton, N.A. (2002). Composition dependent transport diffusion coefficients of CH₄/CF₄ mixtures in carbon nanotubes by non-equilibrium molecular dynamics simulations. *Chemical Engineering Science*, Vol. 57, No. 8, pp. 1343-1354.
- Eastman, J.A., Phillpot, S.R., Choi, S.U.S. & Keblinski, P. (2004). Thermal transport in nanofluids. *Annual Review of Materials Research*, Vol. 34, pp. 219-246.
- Egorov, A.V., Komolkin, A.V. & Chizhik, V.I. (2000). Influence of temperature on the microstructure of the lithium-ion hydration shell. A molecular dynamics description. *Journal of Molecular Liquids*, Vol. 89, No. 1-3, pp. 47-55.
- Endo, M., Kim, Y.A., Ezaka, M., Osada, K., Yanagisawa, T., Hayashi, T., Terrones, M. & Dresselhaus, M.S. (2003). Selective and efficient impregnation of metal nanoparticles on cup-stacked-type carbon nanofibers. *Nano Letters*, Vol. 3, No. 6, pp. 723-726.
- Endo, M., Kim, Y.A., Hayashi, T., Nishimura, K., Matusita, T., Miyashita, K. & Dresselhaus, M.S. (2001). Vapor-grown carbon fibers (VGCFs) - Basic properties and their battery applications. *Carbon*, Vol. 39, No. 9, pp. 1287-1297.
- Evans, D.J. & Morris, G.P. (1990). *Statistical Mechanics of Nonequilibrium Liquids*, London: Academic Press.
- Evans, D.J. & Murad, S. (1977). Singularity Free Algorithm For Molecular-Dynamics Simulation Of Rigid Polyatomics. *Molecular Physics*, Vol. 34, No. 2, pp. 327-331.

- Fan, R., Karnik, R., Yue, M., Li, D.Y., Majumdar, A. & Yang, P.D. (2005). DNA translocation in inorganic nanotubes. *Nano Letters*, Vol. 5, No. 9, pp. 1633-1637.
- Fan, Y.Y., Liao, B., Liu, M., Wei, Y.L., Lu, M.Q. & Cheng, H.M. (1999). Hydrogen uptake in vapor-grown carbon nanofibers. *Carbon*, Vol. 37, No. 10, pp. 1649-1652.
- Freund, J.B. (2005). The atomic detail of an evaporating meniscus. *Physics of Fluids*, Vol. 17, No. 2, 022104(1-9).
- Gao, G.H., Cagin, T. & Goddard, W.A. (1998). Position of K atoms in doped single-walled carbon nanotube crystals. *Physical Review Letters*, Vol. 80, No. 25, pp. 5556-5559.
- Gordon, P.A. & Saeger, P.B. (1999). Molecular modeling of adsorptive energy storage: Hydrogen storage in single-walled carbon nanotubes. *Industrial & Engineering Chemistry Research*, Vol. 38, No. 12, pp. 4647-4655.
- Grigorian, L., Sumanasekera, G.U., Loper, A.L., Fang, S., Allen, J.L. & Eklund, P.C. (1998). Transport properties of alkali-metal-doped single-wall carbon nanotubes. *Physical Review B*, Vol. 58, No. 8, pp. R4195-R4198.
- Gu, C., Gao, G.H., Yu, Y.X. & Mao, Z.Q. (2001). Simulation study of hydrogen storage in single walled carbon nanotubes. *International Journal of Hydrogen Energy*, Vol. 26, No. 7, pp. 691-696.
- Guay, P., Stansfield, B.L. & Rochefort, A. (2004). On the control of carbon nanostructures for hydrogen storage applications. *Carbon*, Vol. 42, No. 11, pp. 2187-2193.

- Gupta, B.K., Awasthi, K. & Srivastava, O.N. (2000). New carbon variants: graphitic nanofibres and nanotubules as hydrogen storage materials. In *Proceedings of the 13th World Hydrogen Energy Conference*. Beijing, China. p. 487.
- Haile, J.M. (1992). *Molecular dynamics simulation : elementary methods*, New York :: Wiley.
- Haluska, M., Hirscher, M., Becher, M., Dettlaff-Weglikowska, U., Chen, X. & Roth, S. (2004). Interaction of hydrogen isotopes with carbon nanostructures. *Materials Science and Engineering B-Solid State Materials for Advanced Technology*, Vol. 108, No. 1-2, pp. 130-133.
- Han, S.S. & Lee, H.M. (2004). Adsorption properties of hydrogen on (10,0) single-walled carbon nanotube through density functional theory. *Carbon*, Vol. 42, No. 11, pp. 2169-2177.
- Hanasaki, I., Nakatani, A. & Kitagawa, H. (2004). Molecular dynamics study of Ar flow and He flow inside carbon nanotube junction as a molecular nozzle and diffuser. *Science and Technology of Advanced Materials*, Vol. 5, No. 1-2, pp. 107-113.
- He, L.Z., Dexter, A.F. & Middelberg, A.P.J. (2006). Biomolecular engineering at interfaces. *Chemical Engineering Science*, Vol. 61, No. 3, pp. 989-1003.
- Hegedus, P.J. & Abramson, A.R. (2006). A molecular dynamics study of interfacial thermal transport in heterogeneous systems. *International Journal of Heat and Mass Transfer*, Vol. 49, No. 25-26, pp. 4921-4931.
- Henderson, J.R. & Vanswol, F. (1984). On The Interface Between A Fluid And A Planar Wall - Theory And Simulations Of A Hard-Sphere Fluid At A Hard-Wall. *Molecular Physics*, Vol. 51, No. 4, pp. 991-1010.

- Heremans, J. (1985). Electrical-Conductivity Of Vapor-Grown Carbon-Fibers. *Carbon*, Vol. 23, No. 4, pp. 431-436.
- Heremans, J. & Beetz, C.P. (1985). Thermal-Conductivity And Thermopower Of Vapor-Grown Graphite Fibers. *Physical Review B*, Vol. 32, No. 4, pp. 1981-1986.
- Heyes, D.M. & March, N.H. (1996). Theoretical approaches to thermal conductivity in liquids. *Physics and Chemistry of Liquids*, Vol. 33, No. 2, pp. 65-83.
- Hirscher, M., Becher, M., Haluska, M., Dettlaff-Weglikowska, U., Quintel, A., Duesberg, G.S., Choi, Y.M., Downes, P., Hulman, M., Roth, S., Stepanek, I. & Bernier, P. (2001). Hydrogen storage in sonicated carbon materials. *Applied Physics a-Materials Science & Processing*, Vol. 72, No. 2, pp. 129-132.
- Hirscher, M., Becher, M., Haluska, M., Quintel, A., Skakalova, V., Choi, Y.M., Dettlaff-Weglikowska, U., Roth, S., Stepanek, I., Bernier, P., Leonhardt, A. & Fink, J. (2002). Hydrogen storage in carbon nanostructures. *Journal of Alloys and Compounds*, Vol. 330, pp. 654-658.
- Hirscher, M., Becher, M., Haluska, M., von Zeppelin, F., Chen, X.H., Dettlaff-Weglikowska, U. & Roth, S. (2003). Are carbon nanostructures an efficient hydrogen storage medium? *Journal of Alloys and Compounds*, Vol. 356, pp. 433-437.
- Hoos, J.S., Sudergat, H., Hoelck, J.P., Stahl, M., de Vlieger, J.S.B., Niessen, W.M.A., Lingeman, H. & Irth, H. (2006). Selective quantitative bioanalysis of proteins in biological fluids by on-line immunoaffinity chromatography-protein digestion-liquid chromatography-mass spectrometry. *Journal of Chromatography B*

- Analytical Technologies in the Biomedical and Life Sciences*, Vol. 830, No. 2, pp. 262-269.
- Jeong, G.H., Farajian, A.A., Hirata, T., Hatakeyama, R., Tohji, K., Briere, T.M., Mizuseki, H. & Kawazoe, Y. (2003). Encapsulation of cesium inside single-walled carbon nanotubes by plasma-ion irradiation method. *Thin Solid Films*, Vol. 435, No. 1-2, pp. 307-311.
- Jeong, G.H., Hirata, T., Hatakeyama, R., Tohji, K. & Motomiya, K. (2002). C-60 encapsulation inside single-walled carbon nanotubes using alkali-fullerene plasma method. *Carbon*, Vol. 40, No. 12, pp. 2247-2253.
- Johnson, R.A., Oh, D. J. (1989). Analytic Embedded Atom Method Model for BCC Metals. *Journal of Material Research*, Vol. 4, No. 5, pp. 1195-1201.
- Jorgensen, W.L., Bigot, B. & Chandrasekhar, J. (1982). Quantum and statistical mechanical studies of liquids. 21. The nature of dilute solutions of sodium and methoxide ions in methanol. *J. Am. Chem. Soc.*, Vol. 104, No. 17, pp. 4584-4591.
- Kang, J.W., Byun, K.R., Lee, J.Y., Kong, S.C., Choi, Y.W. & Hwang, H.J. (2004). Molecular dynamics study on the field effect ion transport in carbon nanotube. *Physica E: Low-dimensional Systems and Nanostructures*, Vol. 24, No. 3-4, pp. 349-354.
- Kapitza, P.L. (1941). The Study of Heat Transfer in Helium II. *Journal of Physics, USSR*, Vol. 4, pp. 177.
- Karnik, R., Fan, R., Yue, M., Li, D.Y., Yang, P.D. & Majumdar, A. (2005). Electrostatic control of ions and molecules in nanofluidic transistors. *Nano Letters*, Vol. 5, No. 5, pp. 943-948.

- Keblinski, P., Bazant, M.Z., Dash, R.K. & Treacy, M.M. (2002). Thermodynamic behavior of a model covalent material described by the environment-dependent interatomic potential. *Physical Review B*, Vol. 66, No. 6, 064104.
- Khandurina, J. & Guttman, A. (2002). Bioanalysis in microfluidic devices. *Journal of Chromatography A*, Vol. 943, No. 2, pp. 159-183.
- Khare, R., Keblinski, P. & Yethiraj, A. (2006). Molecular dynamics simulations of heat and momentum transfer at a solid-fluid interface: Relationship between thermal and velocity slip. *International Journal of Heat and Mass Transfer*, Vol. 49, No. 19-20, pp. 3401-3407.
- Kock, A.J.H.M., de Bokx, P.K., Boellaard, E., Klop, W. & Geus, J.W. (1985). The formation of filamentous carbon on iron and nickel catalysts : II. Mechanism. *Journal of Catalysis*, Vol. 96, No. 2, pp. 468-480.
- Kong, J., Franklin, N.R., Zhou, C.W., Chapline, M.G., Peng, S., Cho, K.J. & Dai, H.J. (2000). Nanotube molecular wires as chemical sensors. *Science*, Vol. 287, No. 5453, pp. 622-625.
- Kotsalis, E.M., Walther, J.H. & Koumoutsakos, P. (2004). Multiphase water flow inside carbon nanotubes. *International Journal of Multiphase Flow*, Vol. 30, No. 7-8, pp. 995-1010.
- Krajcik, R., Jung, A., Hirsch, A., Neuhuber, W. & Zolk, O. (2008). Functionalization of carbon nanotubes enables non-covalent binding and intracellular delivery of small interfering RNA for efficient knock-down of genes. *Biochemical and Biophysical Research Communications*, Vol. 369, No. 2, pp. 595-602.

- Lee, S.M. & Lee, Y.H. (2000). Hydrogen storage in single-walled carbon nanotubes. *Applied Physics Letters*, Vol. 76, No. 20, pp. 2877-2879.
- Lee, S.M., Park, K.S., Choi, Y.C., Park, Y.S., Bok, J.M., Bae, D.J., Nahm, K.S., Choi, Y.G., Yu, S.C., Kim, N.G., Frauenheim, T. & Lee, Y.H. (2000). Hydrogen adsorption and storage in carbon nanotubes. *Synthetic Metals*, Vol. 113, No. 3, pp. 209-216.
- Li, J., Furuta, T., Goto, H., Ohashi, T., Fujiwara, Y. & Yip, S. (2003a). Theoretical evaluation of hydrogen storage capacity in pure carbon nanostructures. *Journal of Chemical Physics*, Vol. 119, No. 4, pp. 2376-2385.
- Li, R., Shang, Z., Wang, G., Pan, Y. & Zhao, X. (2003b). Theoretical investigation on the hydrogenation of armchair single-walled carbon nanotubes. *Journal of Molecular Structure: THEOCHEM*, Vol. 635, No. 1-3, pp. 203-210.
- Li, X.S., Zhu, H.W., Xu, C.L., Mao, Z.Q. & Wu, D.H. (2003c). Measuring hydrogen storage capacity of carbon nanotubes by tangent-mass method. *International Journal of Hydrogen Energy*, Vol. 28, No. 11, pp. 1251-1253.
- Lin, J. & Murad, S. (2001). The role of external electric fields in membrane-based separation processes: a molecular dynamics study. *Molecular Physics*, Vol. 99, No. 5, pp. 463-469.
- Liu, C., Fan, Y.Y., Liu, M., Cong, H.T., Cheng, H.M. & Dresselhaus, M.S. (1999). Hydrogen storage in single-walled carbon nanotubes at room temperature. *Science*, Vol. 286, No. 5442, pp. 1127-1129.

- Louchev, O.A., Laude, T., Sato, Y. & Kanda, H. (2003). Diffusion-controlled kinetics of carbon nanotube forest growth by chemical vapor deposition. *The Journal of Chemical Physics*, Vol. 118, No. 16, pp. 7622-7634.
- Lueking, A. & Yang, R.T. (2002). Hydrogen spillover from a metal oxide catalyst onto carbon nanotubes - Implications for hydrogen storage. *Journal of Catalysis*, Vol. 206, No. 1, pp. 165-168.
- Lummen, N. & Kraska, T. (2004). Investigation of the formation of iron nanoparticles from the gas phase by molecular dynamics simulation. *Nanotechnology*, Vol. 15, No. 5, pp. 525-533.
- Martin, F., Walczak, R., Boiarski, A., Cohen, M., West, T., Cosentino, C. & Ferrari, M. (2005). Tailoring width of microfabricated nanochannels to solute size can be used to control diffusion kinetics. *Journal of Controlled Release*, Vol. 102, No. 1, pp. 123-133.
- Maruyama, S., Kimura, T. (1999). A Study on Thermal Resistance over a Solid-Liquid Interface by the Molecular Dynamics Method. *Thermal Science and Engineering*, Vol. 7, No. 1, pp. 63-68.
- Mendelev, M.I., Han, S., Srolovitz, D.J., Ackland, G.J., Sun, D.Y. & Asta, M. (2003). Development of new interatomic potentials appropriate for crystalline and liquid iron. *Philosophical Magazine*, Vol. 83, No. 35, pp. 3977-3994.
- Meregalli, V. & Parrinello, M. (2001). Review of theoretical calculations of hydrogen storage in carbon-based materials. *Applied Physics a-Materials Science & Processing*, Vol. 72, No. 2, pp. 143-146.

- Mitchell, M.C., Gallo, M. & Nenoff, T.M. (2004). Computer simulations of adsorption and diffusion for binary mixtures of methane and hydrogen in titanosilicates. *Journal of Chemical Physics*, Vol. 121, No. 4, pp. 1910-1916.
- Murad, S., Jia, W. & Krishnamurthy, M. (2003). Molecular simulations of ion exchange in NaA zeolite membranes. *Chemical Physics Letters*, Vol. 369, No. 3-4, pp. 402-408.
- Murad, S. & Lin, J. (1999). Molecular modeling of fluid separations using membranes: effect of molecular forces on mass transfer rates. *Chemical Engineering Journal*, Vol. 74, No. 1-2, pp. 99-108.
- Murad, S. & Lin, J. (2002). Using thin zeolite membranes and external electric fields to separate supercritical aqueous electrolyte solutions. *Industrial & Engineering Chemistry Research*, Vol. 41, No. 5, pp. 1076-1083.
- Murad, S., Oder, K. & Lin, J. (1998). Molecular simulation of osmosis, reverse osmosis, and electro-osmosis in aqueous and methanolic electrolyte solutions. *Molecular Physics*, Vol. 95, No. 3, pp. 401-408.
- Murad, S. & Puri, I.K. (2007a). Dynamics of nanoscale jet formation and impingement on flat surfaces. *Physics of Fluids*, Vol. 19, pp. 128102.
- Murad, S. & Puri, I.K. (2007b). Nanoscale jet collision and mixing dynamics. *Nano Letters*, Vol. 7, No. 3, pp. 707-712.
- Murad, S. & Puri, I.K. (2008). Thermal transport across nanoscale solid-fluid interfaces. *Applied Physics Letters*, Vol. 92, pp. 133105.

- Murad, S., Ravi, P. & Powles, J.G. (1993). A Computer-Simulation Study Of Fluids In Model Slit, Tubular, And Cubic Micropores. *Journal of Chemical Physics*, Vol. 98, No. 12, pp. 9771-9781.
- Naab, F.U., Dhouhadel, M., Gilbert, J.R., Gilbert, M.C., Savage, L.K., Holland, O.W., Duggan, J.L. & McDaniel, F.D. (2006). Direct measurement of hydrogen adsorption in carbon nanotubes/nanofibers by elastic recoil detection. *Physics Letters A*, Vol. 356, No. 2, pp. 152-155.
- Nagayama, G. & Cheng, P. (2004). Effects of interface wettability on microscale flow by molecular dynamics simulation. *International Journal of Heat and Mass Transfer*, Vol. 47, No. 3, pp. 501-513.
- Nigra, P., Freeman, D.L., Sabo, D. & Doll, J.D. (2004). On the encapsulation of nickel clusters by molecular nitrogen. *The Journal of Chemical Physics*, Vol. 121, No. 1, pp. 475-482.
- Nishimiya, N., Ishigaki, K., Takikawa, H., Ikeda, M., Hibi, Y., Sakakibara, T., Matsumoto, A. & Tsutsumi, K. (2002). Hydrogen sorption by single-walled carbon nanotubes prepared by a torch arc method. *Journal of Alloys and Compounds*, Vol. 339, No. 1-2, pp. 275-282.
- Nutzenadel, C., Zuttel, A., Chartouni, D. & Schlapbach, L. (1999). Electrochemical storage of hydrogen in nanotube materials. *Electrochemical and Solid State Letters*, Vol. 2, No. 1, pp. 30-32.
- Ohara, T. (1999). Contribution of intermolecular energy transfer to heat conduction in a simple liquid. *Journal of Chemical Physics*, Vol. 111, No. 21, pp. 9667-9672.

- Ohara, T. & Suzuki, D. (2000). Intermolecular energy transfer at a solid-liquid interface. *Microscale Thermophysical Engineering*, Vol. 4, No. 3, pp. 189-196.
- Orimo, S., Majer, G., Fukunaga, T., Zuttel, A., Schlapbach, L. & Fujii, H. (1999). Hydrogen in the mechanically prepared nanostructured graphite. *Applied Physics Letters*, Vol. 75, No. 20, pp. 3093-3095.
- Pan, W.Y., Zhang, X.F., Li, S., Wu, D.H. & Mao, Z.Q. (2005). Measuring hydrogen storage capacity of carbon nanotubes by high-pressure microbalance. *International Journal of Hydrogen Energy*, Vol. 30, No. 7, pp. 719-722.
- Panella, B., Hirscher, M. & Roth, S. (2005). Hydrogen adsorption in different carbon nanostructures. *Carbon*, Vol. 43, No. 10, pp. 2209-2214.
- Park, J.H., Alegaonkar, P.S., Jeon, S.Y. & Yoo, J.B. (2008). Carbon nanotube composite: Dispersion routes and field emission parameters. *Composites Science and Technology*, Vol. 68, No. 3-4, pp. 753-759.
- Patel, H.A., Garde, S. & Keblinski, P. (2005). Thermal resistance of nanoscopic liquid-liquid interfaces: Dependence on chemistry and molecular architecture. *Nano Letters*, Vol. 5, No. 11, pp. 2225-2231.
- Pederson, M.R. & Broughton, J.Q. (1992). Nanocapillarity In Fullerene Tubules. *Physical Review Letters*, Vol. 69, No. 18, pp. 2689-2692.
- Petsev, D.N. & Lopez, G.P. (2006). Electrostatic potential and electroosmotic flow in a cylindrical capillary filled with symmetric electrolyte: Analytic solutions in thin double layer approximation. *Journal of Colloid and Interface Science*, Vol. 294, No. 2, pp. 492-498.

- Pinkerton, F.E., Wicke, B.G., Olk, C.H., Tibbetts, G.G., Meisner, G.P., Meyer, M.S. & Herbst, J.F. (2000). Thermogravimetric measurement of hydrogen absorption in alkali-modified carbon materials. *Journal of Physical Chemistry B*, Vol. 104, No. 40, pp. 9460-9467.
- Plimpton, S. (1993). Fast parallel algorithms for short-range molecular dynamics. p. Size: 40 p.
- Plimpton, S. (1995). Fast Parallel Algorithms For Short-Range Molecular-Dynamics. *Journal of Computational Physics*, Vol. 117, No. 1, pp. 1-19.
- Pollack, G.L. (1969). Kapitza Resistance. *Reviews of Modern Physics*, Vol. 41, No. 1, pp. 48.
- Poulikakos, D., Arcidiacono, S. & Maruyama, S. (2003). Molecular dynamics simulation in nanoscale heat transfer: A review. *Microscale Thermophysical Engineering*, Vol. 7, No. 3, pp. 181-206.
- Qiao, R. & Aluru, N.R. (2005). Atomistic simulation of KCl transport in charged silicon nanochannels: Interfacial effects. *Colloids and Surfaces a-Physicochemical and Engineering Aspects*, Vol. 267, No. 1-3, pp. 103-109.
- Rajalakshmi, N., Dhathathreyan, K.S., Govindaraj, A. & Satishkumar, B.C. (2000). Electrochemical investigation of single-walled carbon nanotubes for hydrogen storage. *Electrochimica Acta*, Vol. 45, No. 27, pp. 4511-4515.
- Ren, Y. & Price, D.L. (2001). Neutron scattering study of H-2 adsorption in single-walled carbon nanotubes. *Applied Physics Letters*, Vol. 79, No. 22, pp. 3684-3686.

- Rueckes, T., Kim, K., Joselevich, E., Tseng, G.Y., Cheung, C.L. & Lieber, C.M. (2000). Carbon nanotube-based nonvolatile random access memory for molecular computing. *Science*, Vol. 289, No. 5476, pp. 94-97.
- Rzepka, M., Lamp, P. & de la Casa-Lillo, M.A. (1998). Physisorption of hydrogen on microporous carbon and carbon nanotubes. *Journal of Physical Chemistry B*, Vol. 102, No. 52, pp. 10894-10898.
- Sacco, A., Thacker, P., Chang, T.N. & Chiang, A.T.S. (1984). The initiation and growth of filamentous carbon from [alpha]-iron in H₂, CH₄, H₂O, CO₂, and CO gas mixtures. *Journal of Catalysis*, Vol. 85, No. 1, pp. 224-236.
- Schelling, P.K., Phillpot, S.R. & Keblinski, P. (2004). Kapitza conductance and phonon scattering at grain boundaries by simulation. *Journal of Applied Physics*, Vol. 95, No. 11, pp. 6082-6091.
- Schimmel, H.G., Nijkamp, G., Kearley, G.J., Rivera, A., de Jong, K.P. & Mulder, F.M. (2004). Hydrogen adsorption in carbon nanostructures compared. *Materials Science and Engineering B-Solid State Materials for Advanced Technology*, Vol. 108, No. 1-2, pp. 124-129.
- Schmidt, K.F. (1993). Unusual Tubes Emerge from Boron Nitride. *Science News*, Vol. 143, No. 18, pp. 279.
- Sen, S. & Puri, I.K. (2004). Flame synthesis of carbon nanofibres and nanofibre composites containing encapsulated metal particles. *Nanotechnology*, Vol. 15, No. 3, pp. 264-268.

- Shaijumon, M.M., Bejoy, N. & Ramaprabhu, S. (2005). Catalytic growth of carbon nanotubes over Ni/Cr hydrotalcite-type anionic clay and their hydrogen storage properties. *Applied Surface Science*, Vol. 242, No. 1-2, pp. 192-198.
- Shen, K., Xu, H.F., Jiang, Y.B. & Pietrass, T. (2004). The role of carbon nanotube structure in purification and hydrogen adsorption. *Carbon*, Vol. 42, No. 11, pp. 2315-2322.
- Simonyan, V.V., Diep, P. & Johnson, J.K. (1999). Molecular simulation of hydrogen adsorption in charged single-walled carbon nanotubes. *Journal of Chemical Physics*, Vol. 111, No. 21, pp. 9778-9783.
- Sourirajan, S. & Matsuura, T. (1985). *Reverse osmosis and ultrafiltration*, Washington, D.C. :: American Chemical Society.
- Stan, G. & Cole, M.W. (1998a). Hydrogen adsorption in nanotubes. *Journal of Low Temperature Physics*, Vol. 110, No. 1-2, pp. 539-544.
- Stan, G. & Cole, M.W. (1998b). Low coverage adsorption in cylindrical pores. *Surface Science*, Vol. 395, No. 2-3, pp. 280-291.
- Stepanek, I., Maurin, G., Bernier, P., Gavillet, J., Loiseau, A., Edwards, R. & Jaschinski, O. (2000). Nano-mechanical cutting and opening of single wall carbon nanotubes. *Chemical Physics Letters*, Vol. 331, No. 2-4, pp. 125-131.
- Steve, P. (1995). Fast parallel algorithms for short-range molecular dynamics. *J. Comput. Phys.*, Vol. 117, No. 1, pp. 1-19.
- Stevens, R.J., Zhigilei, L.V. & Norris, P.M. (2007). Effects of temperature and disorder on thermal boundary conductance at solid-solid interfaces: Nonequilibrium

- molecular dynamics simulations. *International Journal of Heat and Mass Transfer*, Vol. 50, No. 19-20, pp. 3977-3989.
- Swartz, E.T. & Pohl, R.O. (1989). Thermal-Boundary Resistance. *Reviews of Modern Physics*, Vol. 61, No. 3, pp. 605-668.
- Tang, Q.H. & Yao, Y.G. (2006). The Kapitza resistance across grain boundary by molecular dynamics simulation. *Nanoscale and Microscale Thermophysical Engineering*, Vol. 10, No. 4, pp. 387-398.
- Tarasov, B.P., Maelen, J.P., Lototsky, M.V., Muradyan, V.E. & Yartys, V.A. (2003). Hydrogen sorption properties of arc generated single-wall carbon nanotubes. *Journal of Alloys and Compounds*, Vol. 356, pp. 510-514.
- Tessonnier, J.P., Wine, G., Estournes, C., Leuvrey, C., Ledoux, M.J. & Pham-Huu, C. (2005). Carbon nanotubes as a 1D template for the synthesis of air sensitive materials: About the confinement effect. *Catalysis Today*, Vol. 102, pp. 29-33.
- Thess, A., Lee, R., Nikolaev, P., Dai, H.J., Petit, P., Robert, J., Xu, C.H., Lee, Y.H., Kim, S.G., Rinzler, A.G., Colbert, D.T., Scuseria, G.E., Tomanek, D., Fischer, J.E. & Smalley, R.E. (1996). Crystalline ropes of metallic carbon nanotubes. *Science*, Vol. 273, No. 5274, pp. 483-487.
- Tibbetts, G.G., Meisner, G.P. & Olk, C.H. (2001). Hydrogen storage capacity of carbon nanotubes, filaments, and vapor-grown fibers. *Carbon*, Vol. 39, No. 15, pp. 2291-2301.
- Tironi, I.G., Sperb, R., Smith, P.E. & Vangunsteren, W.F. (1995). A Generalized Reaction Field Method For Molecular-Dynamics Simulations. *Journal of Chemical Physics*, Vol. 102, No. 13, pp. 5451-5459.

- Toffolo, F., Tommasini, M., Del Zoppo, M. & Zerbi, G. (2005). The hydrogen molecule in strong electrostatic fields: A theoretical vibrational spectroscopy study. *Chemical Physics Letters*, Vol. 405, No. 1-3, pp. 108-113.
- Tsang, S.C., Harris, P.J.F. & Green, M.L.H. (1993). Thinning And Opening Of Carbon Nanotubes By Oxidation Using Carbon-Dioxide. *Nature*, Vol. 362, No. 6420, pp. 520-522.
- Turner, C.H., Brennan, J.K., Pikunic, J. & Gubbins, K.E. (2002). Simulation of chemical reaction equilibria and kinetics in heterogeneous carbon micropores. *Applied Surface Science*, Vol. 196, No. 1-4, pp. 366-374.
- Twu, C.J. & Ho, J.R. (2003). Molecular-dynamics study of energy flow and the Kapitza conductance across an interface with imperfection formed by two dielectric thin films. *Physical Review B*, Vol. 67, No. 20, 205422.
- Valentini, L., Armentano, I. & Kenny, J.M. (2005). Electrically switchable carbon nanotubes hydrophobic surfaces. *Diamond and Related Materials*, Vol. 14, No. 1, pp. 121-124.
- Vitos, L., Ruban, A.V., Skriver, H.L. & Kollár, J. (1998). The surface energy of metals. *Surface Science*, Vol. 411, No. 1-2, pp. 186-202.
- Volpe, M. & Cleri, F. (2003). Role of surface chemistry in hydrogen adsorption in single-wall carbon nanotubes. *Chemical Physics Letters*, Vol. 371, No. 3-4, pp. 476-482.
- Wang, C.S., Chen, J.S., Shiomi, J. & Maruyama, S. (2007). A study on the thermal resistance over solid-liquid-vapor interfaces in a finite-space by a molecular dynamics method. *International Journal of Thermal Sciences*, Vol. 46, No. 12, pp. 1203-1210.

- Wang, Q.Y. & Johnson, J.K. (1999a). Computer simulations of hydrogen adsorption on graphite nanofibers. *Journal of Physical Chemistry B*, Vol. 103, No. 2, pp. 277-281.
- Wang, Q.Y. & Johnson, J.K. (1999b). Molecular simulation of hydrogen adsorption in single-walled carbon nanotubes and idealized carbon slit pores. *Journal of Chemical Physics*, Vol. 110, No. 1, pp. 577-586.
- Wang, Q.Y. & Johnson, J.K. (1999c). Optimization of carbon nanotube arrays for hydrogen adsorption. *Journal of Physical Chemistry B*, Vol. 103, No. 23, pp. 4809-4813.
- Watts, R.O. (1974). Monte Carlo studies of liquid water. *Molecular Physics*, Vol. 28, No. 4, pp. 1069 - 1083.
- Williams, K.A. & Eklund, P.C. (2000). Monte Carlo simulations of H₂ physisorption in finite-diameter carbon nanotube ropes. *Chemical Physics Letters*, Vol. 320, No. 3-4, pp. 352-358.
- Wu, J., Huang, Q.W., Ma, Y.F., Huang, Y., Liu, Z.F., Yang, X.Y., Chen, Y.S. & Chen, D.P. (2008). Distortion of carbon nanotube array and its influence on carbon nanotube growth and termination. *Colloids and Surfaces a-Physicochemical and Engineering Aspects*, Vol. 313, pp. 13-17.
- Xiao, S.P. & Belytschko, T. (2004). A bridging domain method for coupling continua with molecular dynamics. *Computer Methods in Applied Mechanics and Engineering*, Vol. 193, No. 17-20, pp. 1645-1669.

- Xu, J.L. & Li, Y.X. (2007). Boundary conditions at the solid-liquid surface over the multiscale channel size from nanometer to micron. *International Journal of Heat and Mass Transfer*, Vol. 50, No. 13-14, pp. 2571-2581.
- Xue, L., Keblinski, P., Phillpot, S.R., Choi, S.U.S. & Eastman, J.A. (2003). Two regimes of thermal resistance at a liquid-solid interface. *Journal of Chemical Physics*, Vol. 118, No. 1, pp. 337-339.
- Xue, L., Keblinski, P., Phillpot, S.R., Choi, S.U.S. & Eastman, J.A. (2004). Effect of liquid layering at the liquid-solid interface on thermal transport. *International Journal of Heat and Mass Transfer*, Vol. 47, No. 19-20, pp. 4277-4284.
- Yang, R.T. (2000). Hydrogen storage by alkali-doped carbon nanotubes-revisited. *Carbon*, Vol. 38, No. 4, pp. 623-626.
- Ye, Y., Ahn, C.C., Witham, C., Fultz, B., Liu, J., Rinzler, A.G., Colbert, D., Smith, K.A. & Smalley, R.E. (1999). Hydrogen adsorption and cohesive energy of single-walled carbon nanotubes. *Applied Physics Letters*, Vol. 74, No. 16, pp. 2307-2309.
- Yildirim, T. & Ciraci, S. (2005). Titanium-decorated carbon nanotubes as a potential high-capacity hydrogen storage medium. *Physical Review Letters*, Vol. 94, No. 17, 175501.
- Yin, Y.F., Mays, T. & McEnaney, B. (2000). Molecular simulations of hydrogen storage in carbon nanotube arrays. *Langmuir*, Vol. 16, No. 26, pp. 10521-10527.
- Yoo, E., Habe, T. & Nakamura, J. (2005). Possibilities of atomic hydrogen storage by carbon nanotubes or graphite materials. *Science and Technology of Advanced Materials*, Vol. 6, No. 6, pp. 615-619.

- Yu, M.F., Dyer, M.J., Skidmore, G.D., Rohrs, H.W., Lu, X.K., Ausman, K.D., Von Ehr, J.R. & Ruoff, R.S. (1999). Three-dimensional manipulation of carbon nanotubes under a scanning electron microscope. *Nanotechnology*, Vol. 10, No. 3, pp. 244-252.
- Yu, M.F., Lourie, O., Dyer, M.J., Moloni, K., Kelly, T.F. & Ruoff, R.S. (2000). Strength and breaking mechanism of multiwalled carbon nanotubes under tensile load. *Science*, Vol. 287, No. 5453, pp. 637-640.
- Yun, W. & Gyeong, S.H. (2005). Origin of nonlocal interactions in adsorption of polar molecules on Si(001)-2 x 1. *The Journal of Chemical Physics*, Vol. 122, No. 16, pp. 164706.
- Zacharia, R., Kim, K.Y., Kibria, A. & Nahm, K.S. (2005). Enhancement of hydrogen storage capacity of carbon nanotubes via spill-over from vanadium and palladium nanoparticles. *Chemical Physics Letters*, Vol. 412, No. 4-6, pp. 369-375.
- Zhang, Y. & Smith, K.J. (2005). A kinetic model of CH₄ decomposition and filamentous carbon formation on supported Co catalysts. *Journal of Catalysis*, Vol. 231, No. 2, pp. 354-364.
- Zhao, J., Gao, Q.Y., Gu, C. & Yang, Y. (2002). Preparation of multi-walled carbon nanotube array electrodes and its electrochemical intercalation behavior of Li ions. *Chemical Physics Letters*, Vol. 358, No. 1-2, pp. 77-82.
- Zheng, Q.R., Gu, A.Z., Lu, X.S. & Lin, W.S. (2005). Adsorption equilibrium of supercritical hydrogen on multi-walled carbon nanotubes. *Journal of Supercritical Fluids*, Vol. 34, No. 1, pp. 71-79.

- Zhou, L., Zhou, Y.P. & Sun, Y. (2004a). A comparative study of hydrogen adsorption on superactivated carbon versus carbon nanotubes. *International Journal of Hydrogen Energy*, Vol. 29, No. 5, pp. 475-479.
- Zhou, L., Zhou, Y.P. & Sun, Y. (2004b). Enhanced storage of hydrogen at the temperature of liquid nitrogen. *International Journal of Hydrogen Energy*, Vol. 29, No. 3, pp. 319-322.
- Zhou, L., Zhou, Y.P. & Sun, Y. (2006). Studies on the mechanism and capacity of hydrogen uptake by physisorption-based materials. *International Journal of Hydrogen Energy*, Vol. 31, No. 2, pp. 259-264.
- Zhu, H.W., Cao, A.Y., Li, X.S., Xu, C.L., Mao, Z.Q., Ruan, D.B., Liang, J. & Wu, D.H. (2001). Hydrogen adsorption in bundles of well-aligned carbon nano tubes at room temperature. *Applied Surface Science*, Vol. 178, No. 1-4, pp. 50-55.
- Zuttel, A., Sudan, P., Mauron, P., Kiyobayashi, T., Emmenegger, C. & Schlapbach, L. (2002). Hydrogen storage in carbon nanostructures. *International Journal of Hydrogen Energy*, Vol. 27, No. 2, pp. 203-212.

APPENDIX A

Typical LAMMPS input file to compute hydrogen storage:

```
# 3-d LJ hydrogen storage

dimension          3
boundary           p p p

atom_style         full
neighbor           0.5 bin
neigh_modify      delay 3

read_data          INPUT_LMP_570.dat

#kspace_style      ewald 1.0e-2
bond_style         harmonic
bond_coeff         1 1201.1 0.254

# LJ potentials

pair_style         lj/cut/coul/cut 3.0
pair_coeff         1 1 1.0 1.0
pair_coeff         2 2 0.737 1.166
pair_coeff         1 2 0.858 1.083
#pair_coeff        3 3 0.0 0.0
#pair_coeff        1 3 0.0 0.0
#pair_coeff        2 3 0.0 0.0
pair_coeff         3 3 0.0493 0.7787
pair_coeff         1 3 0.222 0.88935
pair_coeff         2 3 0.1906 0.97235

# Define groups

group              cnt type 2
group              hyd type 1
group              li type 3

# Initial velocities

temperature        mobile hyd full
velocity           hyd create 0.26316 482748 temp mobile
fix                1 all nve
fix                2 hyd temp/rescale 100 0.26316 0.26316 0.02 1.0
fix_modify         2 temp mobile
```

Static nanotube and metal

```
velocity      cnt set 0.0 0.0 0.0 units box
fix           3 cnt setforce 0.0 0.0 0.0
fix           4 cnt aveforce 0.0 0.0 0.0
velocity      li set 0.0 0.0 0.0 units box
fix           5 li setforce 0.0 0.0 0.0
fix           6 li aveforce 0.0 0.0 0.0
```

Run

```
timestep      0.0003
thermo        10000
thermo_style  custom step atoms temp pe ke eng evdwl
thermo_modify temp mobile
thermo_modify lost ignore

dump          1 all custom 100000 dump.position.* type mol x y z
dump          2 all xyz 100000 dump.xyz.*
run           1000000
```

Typical LAMMPS data file to specify initial configuration for the computation of hydrogen storage:

Lammps input file for carbon nanotube

2088 atoms
22 bonds
0 angles
0 dihedrals
0 impropers

3 atom types
1 bond types

0.0 89.083 xlo xhi
0.0 23.585 ylo yhi
0.0 23.585 zlo zhi

Masses

1 1.0
2 12.0
3 12.0

Atoms

1 1 1 1.0 9.969015121 9.969015121 9.969015121
2 1 1 -1.0 10.223014832 9.969015121 9.969015121

.....
43 22 1 1.0 79.752120972 19.938030243 19.938030243
44 22 1 -1.0 80.006118774 19.938030243 19.938030243
45 23 2 0.0 20.960548401 11.546074867 9.446883202
46 23 2 0.0 20.960548401 11.063755989 9.549403191

.....
2043 23 2 0.0 68.124099731 13.179007530 9.884426117
2044 23 2 0.0 68.124099731 12.283014297 9.485504150

.....
2087 66 3 0.0 42.500000000 12.500000000 20.000000000
2088 67 3 0.0 45.000000000 10.000000000 20.000000000

Bonds

1 1 1 2
2 1 3 4

.....

21 1 41 42
22 1 43 44

Typical LAMMPS input file to predict growth of carbon nanotubes:

```
# 3-d Carbon Nanotube Growth

dimension          3
boundary           p p p
units              metal

atom_style         atomic
newton             on

read_data          INPUT_LMP_13.5.dat

# Hybrid Potentials

pair_style          hybrid lj/cut 6.0 eam/fs airebo 3.0
pair_coeff          * * airebo CH.airebo NULL C C NULL
pair_coeff          * * eam/fs Fe_mm.eam.fs Fe NULL NULL NULL
#pair_coeff         3 3 lj/cut 0.0024 3.4
pair_coeff          1 2 lj/cut 0.02495 3.7
pair_coeff          1 3 lj/cut 0.02495 3.7
pair_coeff          4 4 lj/cut 0.0103 3.4
pair_coeff          1 4 lj/cut 0.0516 3.7
pair_coeff          2 4 lj/cut 0.00497 3.4
pair_coeff          3 4 lj/cut 0.00497 3.4

# define groups

group              fe type 1
group              cnt type 2
group              c type 3
group              ar type 4

# initial velocities

compute            mobile_ar ar temp
compute            mobile_fe fe temp
compute            mobile_c c temp
velocity           c create 950.0 483800 temp mobile_c
velocity           fe create 950.0 483800 temp mobile_fe
velocity           ar create 950.0 483800 temp mobile_ar
fix                1 all nve
fix                5 fe temp/rescale 100 950.0 950.0 1.0 1.0
fix                6 ar temp/rescale 100 950.0 950.0 1.0 1.0
fix                7 c temp/rescale 100 950.0 950.0 1.0 1.0
#fix_modify        2 temp mobile
```

```

# static nanotube and metal

fix                20 cnt recenter INIT INIT INIT units box

# Run

compute           en all pe/atom
timestep          0.000005

thermo            1000
thermo_style      custom step atoms temp pe ke etotal evdwl
#thermo_modify    temp mobile
thermo_modify     lost ignore

dump              1 all custom 1000 dump.position.* type tag x y z c_en
dump              2 all xyz 10000 dump.xyz.*
run               100000

unfix             20
fix               30 cnt recenter INIT INIT INIT units box

undump            1
undump            2
dump              3 all custom 10000 dump.position.* type tag x y z c_en
dump              4 all xyz 10000 dump.xyz.*
timestep          0.000002
run               200000

unfix             30
run               1700000

```

**Typical LAMMPS data file to specify initial configuration for prediction of growth
of carbon nanotubes:**

Lammps input file for carbon nanotube growth

9604 atoms
0 bonds
0 angles
0 dihedrals
0 impropers

4 atom types
0 bond types

0.0 137.5 xlo xhi
0.0 27.5 ylo yhi
0.0 548.0 zlo zhi

Masses

1 55.847
2 12.0
3 12.0
4 39.94

Atoms

1	1	5.415496826	1.805165529	246.599990845
2	1	3.610331059	1.805165529	248.405166626
.....				
9603	2	62.796142578	17.188240051	233.135681152
9604	2	62.211509705	15.875138283	233.135681152

Typical LAMMPS input file for nanoscale thermal transport:

2-d LJ flow simulation

dimension 3
boundary p p p
units metal

atom_style atomic

create geometry

lattice fcc 6.692
region box block 0 30 0 30 0 580 units box
create_box 2 box

mass 1 39.94
mass 2 55.85

potentials

pair_style hybrid eam/fs lj/cut 10.0
pair_coeff 1 1 lj/cut 0.0103 3.4
pair_coeff * * eam/fs Fe_mm.eam.fs NULL Fe
pair_coeff 1 2 lj/cut 0.0516 3.7

define groups

region 81 block INF INF INF INF 150 154 units box
create_atoms 1 region 81 units box
group liquid1 region 81

region 82 block INF INF INF INF 154 158 units box
create_atoms 1 region 82 units box
group liquid2 region 82

region 83 block INF INF INF INF 158 162 units box
create_atoms 1 region 83 units box
group liquid3 region 83

region 84 block INF INF INF INF 162 166 units box
create_atoms 1 region 84 units box
group liquid4 region 84

region 85 block INF INF INF INF 166 170 units box

create_atoms group	1 region 85 units box liquid5 region 85
region create_atoms group	86 block INF INF INF INF 170 210 units box 1 region 86 units box liquid6 region 86
region create_atoms group	87 block INF INF INF INF 210 250 units box 1 region 87 units box liquid7 region 87
region create_atoms group	88 block INF INF INF INF 250 290 units box 1 region 88 units box liquid8 region 88
region create_atoms group	89 block INF INF INF INF 290 330 units box 1 region 89 units box liquid9 region 89
region create_atoms group	90 block INF INF INF INF 330 370 units box 1 region 90 units box liquid10 region 90
region create_atoms group	91 block INF INF INF INF 370 410 units box 1 region 91 units box liquid11 region 91
region create_atoms group	92 block INF INF INF INF 410 414 units box 1 region 92 units box liquid12 region 92
region create_atoms group	93 block INF INF INF INF 414 418 units box 1 region 93 units box liquid13 region 93
region create_atoms group	94 block INF INF INF INF 418 422 units box 1 region 94 units box liquid14 region 94
region create_atoms group	95 block INF INF INF INF 422 426 units box 1 region 95 units box liquid15 region 95
region create_atoms group	96 block INF INF INF INF 426 430 units box 1 region 96 units box liquid16 region 96

```

region          97 block INF INF INF INF INF 140 units box
create_atoms   1 region 97 units box
group          liquid17 region 97

region          98 block INF INF INF INF 440 580 units box
create_atoms   1 region 98 units box
group          liquid18 region 98

lattice      bcc 2.87

region          1 block INF INF INF INF 140 150 units box
create_atoms   2 region 1 units box
group          lower region 1

region          2 block INF INF INF INF 430 440 units box
create_atoms   2 region 2 units box
group          upper region 2

group          boundary union lower upper
group          flowsides union liquid17 liquid18

group          flow subtract all boundary
group          flow2 subtract flow flowsides

### compute temperatures
compute        temp_1 flow temp/region 81
compute        temp_2 flow temp/region 82
compute        temp_3 flow temp/region 83
compute        temp_4 flow temp/region 84
compute        temp_5 flow temp/region 85
compute        temp_6 flow temp/region 86
compute        temp_7 flow temp/region 87
compute        temp_8 flow temp/region 88
compute        temp_9 flow temp/region 89
compute        temp_10 flow temp/region 90
compute        temp_11 flow temp/region 91
compute        temp_12 flow temp/region 92
compute        temp_13 flow temp/region 93
compute        temp_14 flow temp/region 94
compute        temp_15 flow temp/region 95
compute        temp_16 flow temp/region 96
compute        temp_lower lower temp
compute        temp_upper upper temp
compute        temp_flow flow temp

```

```

compute          energy1 lower group/group flow
compute          energy2 upper group/group flow
compute          energy1a lower group/group flow2
compute          energy2a upper group/group flow2

# initial velocities

velocity         flow create 100.0 581275 units box

fix             111 all nve

fix             1 liquid1 temp/rescale 10 100.0 100.0 0.001 1.0
fix             2 liquid2 temp/rescale 10 100.0 100.0 0.001 1.0
fix             3 liquid3 temp/rescale 10 100.0 100.0 0.001 1.0
fix             4 liquid4 temp/rescale 10 100.0 100.0 0.001 1.0
fix             5 liquid5 temp/rescale 10 100.0 100.0 0.001 1.0
fix             6 liquid6 temp/rescale 10 100.0 100.0 0.001 1.0
fix             7 liquid7 temp/rescale 10 100.0 100.0 0.001 1.0
fix             8 liquid8 temp/rescale 10 100.0 100.0 0.001 1.0
fix             9 liquid9 temp/rescale 10 100.0 100.0 0.001 1.0
fix            10 liquid10 temp/rescale 10 100.0 100.0 0.001 1.0
fix            11 liquid11 temp/rescale 10 100.0 100.0 0.001 1.0
fix            12 liquid12 temp/rescale 10 100.0 100.0 0.001 1.0
fix            13 liquid13 temp/rescale 10 100.0 100.0 0.001 1.0
fix            14 liquid14 temp/rescale 10 100.0 100.0 0.001 1.0
fix            15 liquid15 temp/rescale 10 100.0 100.0 0.001 1.0
fix            16 liquid16 temp/rescale 10 100.0 100.0 0.001 1.0
fix            17 liquid17 temp/rescale 10 100.0 100.0 0.001 1.0
fix            18 liquid18 temp/rescale 10 100.0 100.0 0.001 1.0

velocity         lower create 100.0 281375 units box
velocity         upper create 100.0 281375 units box
fix             221 lower temp/rescale 100 100.0 100.0 0.001 1.0
fix             222 upper temp/rescale 100 100.0 100.0 0.001 1.0

fix             20 lower momentum 10 linear 1 1 1
fix             21 upper momentum 10 linear 1 1 1
fix             22 flow momentum 10 linear 1 1 1

fix             91 flow ave/time 10 10000 100000 c_temp_1 c_temp_2
c_temp_3 c_temp_4 c_temp_5 c_temp_6 c_temp_7 c_temp_8 file heat_fluid1.out
fix             92 flow ave/time 10 10000 100000 c_temp_9 c_temp_10
c_temp_11 c_temp_12 c_temp_13 c_temp_14 c_temp_15 c_temp_16 file heat_fluid2.out
fix             94 upper ave/time 5 10000 100005 c_temp_upper file
heat_upper.out

```

```

fix          95 lower ave/time 5 10000 100005 c_temp_lower file
heat_lower.out
fix          96 all ave/time 100 1000 100000 c_energy1 c_energy1a
c_energy1[1] c_energy1[2] c_energy1[3] c_energy2a c_energy2 file force1.out

# Run

timestep          0.001
thermo            1000
thermo_style      custom step atoms temp pe ke etotal evdwl f_221
c_energy1 c_energy1[1] c_energy1[2] c_energy1[3] c_energy2
thermo_modify     lost ignore temp temp_flow

dump            1 all custom 100000 dump.kapitza.* type tag x y z vx vy vz
run            300000

unfix           1
unfix           2
unfix           3
unfix           4
unfix           5
unfix           6
unfix           7
unfix           8
unfix           9
unfix          10
unfix          11
unfix          12
unfix          13
unfix          14
unfix          15
unfix          16
unfix          17
unfix          18

restart         1000000 therm.restart
run            700000

unfix          221
unfix          222
fix            221 lower temp/rescale 100 125 125 0.001 1.0
fix            222 upper temp/rescale 100 125 125 0.001 1.0

run            7000000

```